

**MEASUREMENT OF THE $Z/\gamma^*(\rightarrow e^+e^-)+\geq n$ JET PRODUCTION CROSS
SECTIONS IN $p\bar{p}$ COLLISIONS AT $\sqrt{s} = 1.96$ TeV
DRAFT v1.3**

BY

MARC BUEHLER

B.S. (University of Basel, Switzerland) 1992
M.S. (University of Heidelberg, Germany) 1997

THESIS

Submitted as partial fulfillment of the requirements
for the degree of Doctor of Philosophy in Physics
in the Graduate College of the
University of Illinois at Chicago, 2005

Chicago, Illinois

Copyright by

Marc Buehler

2005

To Dasha

ACKNOWLEDGMENTS

I want to thank the DØ Collaboration (see Appendix A) ...

MB

TABLE OF CONTENTS

<u>CHAPTER</u>		<u>PAGE</u>
1	INTRODUCTION	1
2	THEORY	2
2.1	The Standard Model	2
2.1.1	Quarks and Leptons	2
2.1.2	Interactions	3
2.1.2.1	Electromagnetic Interaction	7
2.1.2.2	Weak Interaction	9
2.1.2.3	Strong Interaction	11
2.2	$Z/\gamma^* (\rightarrow e^+e^-) + \geq n$ Jets	14
3	EXPERIMENTAL APPARATUS	17
3.1	The Fermilab Accelerators	17
3.1.1	The Preaccelerator	19
3.1.2	The Linac	19
3.1.3	The Booster	20
3.1.4	The Main Injector	21
3.1.5	The Antiproton Source	22
3.1.6	The Tevatron	23
3.2	Luminosity and Cross Section	24
3.3	The DØ Detector	24
3.3.1	Coordinate Systems	26
3.3.2	Central Tracking System	28
3.3.2.1	Silicon Microstrip Tracker	29
3.3.2.2	Central Fiber Tracker	30
3.3.2.3	Solenoidal Magnet	33
3.3.3	Preshower Detectors	34
3.3.3.1	Central Preshower Detector	35
3.3.3.2	Forward Preshower Detector	36
3.3.4	Calorimeter	36
3.3.5	Muon System	38
3.4	The DØ Trigger and Data Acquisition Systems	40
3.4.1	The Level 1 Trigger	44
3.4.1.1	The Level 1 Calorimeter Trigger	44
3.4.1.2	The Level 1 Central Track Trigger	44
3.4.1.3	The Level 1 Muon Trigger	45
3.4.2	The Level 2 Trigger	46

TABLE OF CONTENTS (Continued)

<u>CHAPTER</u>		<u>PAGE</u>
3.4.2.1	The Level 2 Calorimeter Preprocessor	46
3.4.2.2	The Level 2 Muon Preprocessors	47
3.4.2.3	The Level 2 Preshower Preprocessor	48
3.4.2.4	The Level 2 Tracking Preprocessor	48
3.4.2.5	The Level 2 Global Processor	48
3.4.3	The Level 3 Trigger and Data Acquisition	49
4	OFFLINE EVENT RECONSTRUCTION	52
4.1	Track Reconstruction	52
4.2	Primary Vertex Reconstruction	53
4.3	Electromagnetic Object Reconstruction and Identification . .	55
4.3.1	Simple-Cone Clustering Algorithm	55
4.3.2	Electromagnetic Object Identification Parameters	57
4.4	Jet Reconstruction and Identification	60
4.4.1	Jet Cone Algorithm	60
4.4.2	Jet Identification Parameters	61
4.4.3	Jet Energy Scale	62
5	Monte Carlo Event Simulation	65
5.1	The PYTHIA Event Generator	65
5.2	Combining Matrix Elements with Showering	68
5.2.1	Combining ALPGEN with PYTHIA	70
5.2.2	Combining MADGRAPH with PYTHIA	70
5.3	The MCFM Monte Carlo Simulation	71
5.4	The DØ Detector Simulation	71
6	MEASUREMENT OF THE $Z/\gamma^*(\rightarrow e^+e^-)+\geq n$ JET PRODUCTION CROSS SECTIONS	72
6.1	Data and MC Samples	72
6.1.1	Data Sample	72
6.1.2	Monte Carlo Samples	76
6.1.2.1	PYTHIA and ALPGEN Samples	76
6.1.2.2	CKKW Samples	78
6.1.2.3	MCFM Cross Sections	78
6.2	Event Selection	79
6.2.1	Primary Vertex	79
6.2.2	Electron Selection	79
6.2.3	Z Selection	80
6.2.4	Jet Selection	80
6.2.5	Event Statistics	81
6.3	Data vs Monte Carlo	81
6.3.1	Primary Vertex Comparison	82

TABLE OF CONTENTS (Continued)

<u>CHAPTER</u>		<u>PAGE</u>
6.3.2	Z p_T Comparisons	82
6.3.3	$Z/\gamma^* (\rightarrow e^+e^-) + \geq n$ Jet Comparisons	87
6.3.3.1	$Z/\gamma^* (\rightarrow e^+e^-)$ Inclusive Sample	87
6.3.3.2	$Z/\gamma^* (\rightarrow e^+e^-) + \geq 1$ Jet Sample	87
6.3.3.3	$Z/\gamma^* (\rightarrow e^+e^-) + \geq 2$ Jet Sample	87
6.4	$Z/\gamma^* (\rightarrow e^+e^-)$ Inclusive Cross Section	99
6.4.1	Efficiencies	100
6.4.1.1	Trigger Efficiency	100
6.4.1.2	EM Reconstruction and Identification Efficiency	103
6.4.1.3	EM-Track Match Efficiency	106
6.4.1.4	Acceptance	111
6.4.2	Cross section calculation	111
6.4.3	Comparisons to other measurements	113
6.5	$Z/\gamma^* (\rightarrow e^+e^-) + \geq n$ Jets Cross Section	115
6.5.1	Efficiencies vs Jet Multiplicity	116
6.5.1.1	Trigger Efficiency	116
6.5.1.2	EM Reconstruction and Identification Efficiency	118
6.5.1.3	EM-Track Match Efficiency	118
6.5.1.4	Acceptance	122
6.5.1.5	Jet Reconstruction and Identification Efficiency	123
6.5.2	Cross section calculation	126
6.5.2.1	Unsmearing	126
6.5.2.2	Electron-Jet-Overlap Correction	138
6.5.2.3	Cross sections	144
6.6	Systematics	151
6.6.1	Jet Energy Scale Systematic Error	151
6.6.2	Systematic Error of Cross Section Unfolding	153
6.6.3	Electron-Jet-Overlap Systematic Error	161
6.6.4	Luminosity Systematic Error	161
6.6.5	Systematic Errors due to Efficiencies	162
6.6.5.1	Trigger Efficiency	162
6.6.5.2	EM Reconstruction and Identification Efficiency	163
6.6.5.3	EM-Track Match Efficiency	163
6.6.5.4	Overall Efficiency Systematic Error	164
6.6.6	Jet Promotion Systematic Error	164
6.6.7	Statistical Uncertainty	165
7	CONCLUSIONS	170
7.1	Final Results	170
7.2	Future Plans	171
	APPENDICES	176

TABLE OF CONTENTS (Continued)

<u>CHAPTER</u>	<u>PAGE</u>
Appendix A	177
Appendix B	191
CITED LITERATURE	200
VITA	206

LIST OF TABLES

<u>TABLE</u>		<u>PAGE</u>
I	SINGLE EM TRIGGERS USED IN THIS ANALYSIS	75
II	LIST OF MC SAMPLES	77
III	JET RESOLUTION PARAMETERS IN DATA AND MC.	78
IV	LIST OF CKKW SAMPLES	79
V	EVENT BREAKDOWN BY EXCLUSIVE JET MULTIPLICITIES ASSOCIATED WITH Z/γ^* PRODUCTION BEFORE ANY BACK- GROUND IS SUBTRACTED OR ANY CORRECTIONS ARE AP- PLIED.	82
VI	CROSS SECTION RESULTS FOR DIFFERENT DIEM INVARI- ANT MASS RANGES AND PROCESSES.	115
VII	OBJECT BASED TRIGGER EFFICIENCIES WITH STATISTI- CAL AND SYSTEMATIC ERRORS (RESPECTIVELY) FOR THE PRE-V12 AND V12 DATASETS FOR DIFFERENT INCLUSIVE JET MULTIPLICITIES.	116
VIII	OBJECT BASED EM RECO AND ID EFFICIENCIES WITH STA- TISTICAL AND SYSTEMATIC ERRORS (RESPECTIVELY) IN DATA AND MC FOR DIFFERENT INCLUSIVE JET MULTIPLI- CITIES. THERE WAS NOT ENOUGH STATISTICS AVAILABLE TO ESTIMATE THE EM EFFICIENCY IN DATA FOR ≥ 3 JETS.	120
IX	OBJECT BASED TRACKING EFFICIENCIES WITH STATISTI- CAL ERRORS IN DATA AND MC FOR DIFFERENT INCLUSIVE JET MULTIPLICITIES.	120
X	OBJECT BASED TRACKING EFFICIENCIES WITH SYSTEM- ATIC ERRORS.	122
XI	ACCEPTANCES WITH STATISTICAL ERRORS FOR DIFFER- ENT JET MULTIPLICITIES.	123

LIST OF TABLES (Continued)

<u>TABLE</u>		<u>PAGE</u>
XII	UNSMEARING AND JET RECO/ID COEFFICIENTS WITH SYSTEMATIC UNCERTAINTY DUE TO RESOLUTION AND JET RECO/ID EFFICIENCY.	127
XIII	ELECTRON-JET-OVERLAP COEFFICIENTS WITH SYSTEMATIC UNCERTAINTIES.	140
XIV	NUMBER OF SIGNAL EVENTS (DRELL-YAN IN PARENTHESES) AND NUMBER OF BACKGROUND EVENTS (QCD) FOR DIFFERENT JET MULTIPLICITIES. NUMBERS ARE CORRECTED FOR TRIGGER, EM AND TRACKING INEFFICIENCIES (AFTER APPLYING THE UNSMEARING, JET RECO/ID AND ELECTRON-JET-OVERLAP CORRECTIONS).	144
XV	FINAL CROSS SECTIONS WITH JES ERRORS.	151
XVI	FINAL CROSS SECTIONS WITH JET RECO/ID ERRORS. . . .	159
XVII	FINAL CROSS SECTIONS WITH JET RESOLUTION ERRORS.	159
XVIII	FINAL CROSS SECTIONS WITH ELECTRON-JET-OVERLAP CUT UNCERTAINTIES.	161
XIX	FINAL CROSS SECTIONS WITH LUMINOSITY ERRORS.	162
XX	RELATIVE ERRORS DUE TO UNCERTAINTY IN EM-TRACK MATCHING EFFICIENCIES.	164
XXI	OVERALL SYSTEMATIC UNCERTAINTIES DUE TO EFFICIENCIES (TRIGGER, EM, TRACKING).	165
XXII	NUMBER OF EVENTS FOR DIFFERENT INCLUSIVE JET MULTIPLICITIES WHEN REQUIRING EXACTLY ONE RECONSTRUCTED PRIMARY VERTEX AND AT LEAST TWO RECONSTRUCTED PRIMARY VERTICES. ENTRIES ARE NORMALIZED WITH RESPECT TO THE 2 VERTEX SAMPLE.	166
XXIII	AVERAGE NUMBER OF RECONSTRUCTED PRIMARY VERTICES FOR DIFFERENT JET MULTIPLICITIES.	166
XXIV	CROSS SECTIONS WITH STATISTICAL ERRORS.	169

LIST OF TABLES (Continued)

<u>TABLE</u>		<u>PAGE</u>
XXV	CROSS SECTIONS FOR DIFFERENT INCLUSIVE JET MULTIPLICITIES. NUMBER OF SIGNAL EVENT ENTRIES HAVE UNSMEARING, JET RECO/ID AND ELECTRON-JET-OVERLAP CORRECTIONS APPLIED.	171
XXVI	COMPARING MEASURED CROSS SECTIONS WITH RESULTS FROM MCFM AND CKKW.	172
XXVII	COMPARING MEASURED CROSS SECTION RATIOS WITH RESULTS FROM MCFM AND CKKW.	172

LIST OF FIGURES

<u>FIGURE</u>	<u>PAGE</u>
1 Quarks and leptons.	4
2 Interactions and their properties.	7
3 Feynman diagram for the process $e^+e^- \rightarrow \gamma^* \rightarrow \mu^+\mu^-$. (a) Tree level diagram. (b) One-loop diagram.	8
4 The Higgs potential.	12
5 Feynman diagram for one of the leading-order processes that produces a Z boson with an associated jet coming from a gluon.	15
6 SM Higgs boson production in association with a Z boson (<i>Higgsstrahlung</i>).	16
7 Z boson generation in association with two gluons.	16
8 Schematic view of the Fermilab accelerator chain.	18
9 Basic configuration of a magnetron.	20
10 Schematic of Linac RF cavity.	21
11 Simplified drawing of anti-proton production with nickel target and lithium lens.	23
12 Tevatron integrated luminosity delivered to DØ (April 2002 - March 2005).	25
13 Schematic view of the DØ detector.	27
14 The DØ central tracking system with with solenoid, preshower detectors, luminosity monitor, and calorimeter.	29
15 Double-sided ladder design, n-side.	31
16 SMT disk and barrel design.	31

LIST OF FIGURES (Continued)

<u>FIGURE</u>		<u>PAGE</u>
17	a) Location of the Central Fiber Tracker (CFT). b) Closeup view of axial and stereo layers.	32
18	$y - z$ view of the DØ magnetic field with both the toroid and solenoid magnets at full current. Numbers are in kG (10 kG = 1 T).	33
19	Perspective view of the solenoid inside the central calorimeter.	34
20	Cross section and layout geometry of the CPS and FPS scintillator strips.	35
21	Isometric view of the central and two end calorimeters.	39
22	Schematic view of two calorimeter cells.	40
23	Schematic view showing the calorimeter segmentation pattern. The shading pattern indicates cells for signal readout. The radial lines show the detector pseudo-rapidity intervals.	41
24	Schematic view of different calorimeter detection layers vs η	42
25	The DØ muon system with scintillators (SCINT) and drift tubes (PDT and MDT).	43
26	A hypothetical L1CTT track with hits in eight CFT axial doublet layers and the CPS axial layer.	45
27	The definition of roads based on L1 tracks and SMT hit selection in L2STT.	49
28	Main L3DAQ hardware components.	51
29	Axial view (looking down the beam-pipe) of a recorded event showing hits and reconstructed tracks. CFT hits are represented by squares, and SMT hits are represented by circles. Hits are colored solid if they are associated with a reconstructed track (solid lines). The curvature of the reconstructed tracks is due to the solenoidal magnetic field, which is pointing out of the page.	54
30	Illustration of the Isolation Parameter: E_{isoTot} is the total energy in a cone of radius 0.4, and $E_{isoCore}$ is the energy in the EM layers in a cone of radius 0.2.	56

LIST OF FIGURES (Continued)

<u>FIGURE</u>		<u>PAGE</u>
31	Illustration of the EM fraction parameter: EM fraction is the ratio between the energy in the CPS plus EM layers, and the energy in the CPS plus EM layers plus hadronic layers.	58
32	The jet energy scale correction factor measured for jets in data as a function of E (top) and η (bottom).	64
33	Schematic view of a parton shower.	68
34	Primary vertex distribution in data and MC (PYTHIA) for the inclusive sample.	83
35	Comparing Z p_T between data and PYTHIA MC (left), and ratio correction factor (right).	84
36	Comparing Z p_T between data and ALPGEN + PYTHIA $Z+1$ jet MC.	85
37	Comparing Z p_T between data and ALPGEN + PYTHIA $Z+2$ jets MC.	86
38	p_T of both Z electrons (top left), physics η of both Z electrons (bottom left), Z p_T (top right), Z rapidity (bottom right) for the $Z/\gamma^* \rightarrow e^+e^-$ inclusive sample in data and MC (PYTHIA).	88
39	Diem invariant mass comparison for the $Z/\gamma^* \rightarrow e^+e^-$ inclusive sample in data and MC (PYTHIA). Data is background subtracted.	89
40	p_T of both Z electrons (top left), physics η of both Z electrons (bottom left), Z p_T (top right), Z rapidity (bottom right) for the $Z/\gamma^* \rightarrow e^+e^- + \geq 1$ jet sample in data and MC (ALPGEN).	90
41	Diem invariant mass comparison for the $Z/\gamma^* \rightarrow e^+e^- + \geq 1$ jet sample in data and MC (ALPGEN). Data is background subtracted.	91
42	p_T (linear and logarithmic), physics η and physics Φ of all jets for the $Z/\gamma^* \rightarrow e^+e^- + \geq 1$ jet sample in data and MC (ALPGEN).	92
43	p_T (linear and logarithmic), physics η and physics Φ of the leading jets for the $Z/\gamma^* \rightarrow e^+e^- + \geq 1$ jet sample in data and MC (ALPGEN).	93
44	p_T of both Z electrons (top left), physics η of both Z electrons (bottom left), Z p_T (top right), Z rapidity (bottom right) for the $Z/\gamma^* \rightarrow e^+e^- + \geq 2$ jet sample in data and MC (ALPGEN).	94

LIST OF FIGURES (Continued)

<u>FIGURE</u>		<u>PAGE</u>
45	Diem invariant mass comparison for the $Z/\gamma^* \rightarrow e^+e^- + \geq 2$ jet sample in data and MC (ALPGEN). Data is background subtracted.	95
46	p_T (linear and logarithmic), physics η and physics Φ of all jets for the $Z/\gamma^* \rightarrow e^+e^- + \geq 2$ jet sample in data and MC (ALPGEN).	96
47	p_T (linear and logarithmic), physics η and physics Φ of the leading jets for the $Z/\gamma^* \rightarrow e^+e^- + \geq 2$ jet sample in data and MC (ALPGEN). . .	97
48	p_T (linear and logarithmic), physics η and physics Φ of the next to leading jets for the $Z/\gamma^* \rightarrow e^+e^- + \geq 2$ jet sample in data and MC (ALPGEN).	98
49	Trigger efficiencies for pre-v12 (top) and v12 (bottom) datasets vs EM object p_T	102
50	EM efficiencies versus probe track Φ and p_T in data. The Φ distribution shows the modulus($\Phi, \frac{2\pi}{32}$) distribution to illustrate the effect of the calorimeter Φ -module boundaries.	106
51	EM efficiencies versus probe track Φ and p_T in MC. The Φ distribution shows the modulus($\Phi, \frac{2\pi}{32}$) distribution to illustrate the effect of the calorimeter Φ -module boundaries.	107
52	Invariant mass in data when requiring at least one track-matched electron.	109
53	Invariant mass in data when requiring two track-matched electrons. . .	109
54	Invariant mass in MC when requiring at least one track-matched electron.	110
55	Invariant mass in MC when requiring two track-matched electrons. . . .	110
56	Diem invariant mass distribution for $Z/\gamma^* \rightarrow e^+e^- + X$ (Mean = 91.02 GeV \pm 0.04 GeV, Width 4.03 GeV \pm 0.04 GeV).	114
57	Average object based trigger efficiencies in data versus inclusive jet multiplicity.	117
58	Average object based EM reco and ID efficiencies in data and MC versus inclusive jet multiplicity.	119

LIST OF FIGURES (Continued)

<u>FIGURE</u>		<u>PAGE</u>
59	Average object based tracking efficiencies in data and MC versus inclusive jet multiplicity.	121
60	Jet reco/ID efficiencies in data. $CC = -0.7 < \eta_{det} < 0.7$, $ICR = 0.7 < \eta_{det} < 1.5$, $EC = 1.5 < \eta_{det} < 2.5$	125
61	Comparing inclusive jet multiplicities between data and particle level MC (applying data resolution smearing and data jet reco/ID efficiencies). The distributions are normalized with respect to the first bin.	128
62	Ratio of MC (with smearing and jet reco/ID efficiencies) inclusive jet multiplicities and data inclusive jet multiplicities.	128
63	Comparing inclusive jet multiplicities between data and particle level MC (after applying correction factors). The distributions are normalized with respect to the first bin.	129
64	Comparing jet p_T for all jets between data and particle level MC (with data resolution smearing and jet reco/ID efficiencies applied).	129
65	Comparing jet p_T for all jets between data and particle level MC (with data resolution smearing and jet reco/ID efficiencies applied).	130
66	Comparing jet p_T for leading jets between data and particle level MC (with data resolution smearing and jet reco/ID efficiencies applied). Kolmogorov-Smirnov Probability = 0.13. The gray band shows the uncertainty due to the jet energy scale.	130
67	Comparing jet p_T for leading jets between data and particle level MC (with data resolution smearing and jet reco/ID efficiencies applied). Kolmogorov-Smirnov Probability = 0.13. The gray band shows the uncertainty due to the jet energy scale.	131
68	Comparing jet p_T for second leading jets between data and particle level MC (with data resolution smearing and jet reco/ID efficiencies applied). Kolmogorov-Smirnov Probability = 0.56. The gray band shows the uncertainty due to the jet energy scale.	131
69	Comparing jet p_T for second leading jets between data and particle level MC (with data resolution smearing and jet reco/ID efficiencies applied). Kolmogorov-Smirnov Probability = 0.56. The gray band shows the uncertainty due to the jet energy scale.	132

LIST OF FIGURES (Continued)

<u>FIGURE</u>		<u>PAGE</u>
70	Comparing jet p_T for third leading jets between data and particle level MC (with data resolution smearing and jet reco/ID efficiencies applied). Kolmogorov-Smirnov Probability = 0.57.	132
71	Comparing jet p_T for third leading jets between data and particle level MC (with data resolution smearing and jet reco/ID efficiencies applied). Kolmogorov-Smirnov Probability = 0.57.	133
72	Comparing jet η for all jets between data and particle level MC (with data resolution smearing and jet reco/ID efficiencies applied).	133
73	Comparing jet η for leading jets between data and particle level MC (with data resolution smearing and jet reco/ID efficiencies applied). Kolmogorov-Smirnov Probability = 0.70.	134
74	Comparing jet η for second leading jets between data and particle level MC (with data resolution smearing and jet reco/ID efficiencies applied). Kolmogorov-Smirnov Probability = 0.30.	134
75	Comparing jet η for third leading jets between data and particle level MC (with data resolution smearing and jet reco/ID efficiencies applied). Kolmogorov-Smirnov Probability = 0.93.	135
76	Unsmearing and jet reco/ID particle jet multiplicities (left) and coefficients (right).	136
77	Unsmearing jet multiplicities (left) and coefficients (right) without applying jet reco/ID efficiencies.	137
78	ΔR between probe-tracks and good jets in data (without electron-jet-overlap cut).	139
79	ΔR between probe-tracks and good jets using PYTHIA MC (without electron-jet-overlap cut).	140
80	ΔR between probe-tracks and good jets in data (after the electron-jet-overlap cut was applied).	141
81	ΔR between generated electrons ($p_T > 25$ GeV, $ \eta < 1.1$) and partons ($p_T > 20$ GeV, $ \eta < 2.5$).	142
82	ΔR between partons and matched calorimeter jets ($p_T > 20$ GeV, $ \eta < 2.5$).	143

LIST OF FIGURES (Continued)

<u>FIGURE</u>		<u>PAGE</u>
83	Diem invariant mass distribution for the $Z/\gamma^* \rightarrow e^+e^- + \geq 1$ jet sample. The solid line shows a Gaussian plus Breit-Wigner fit to the Z peak. The dashed line shows an exponential fit to the QCD and Drell-Yan contribution.	145
84	Diem invariant mass distribution for the $Z/\gamma^* \rightarrow e^+e^- + \geq 2$ jet sample. The solid line shows a Gaussian plus Breit-Wigner fit to the Z peak. The dashed line shows an exponential fit to the QCD and Drell-Yan contribution.	146
85	Diem invariant mass distribution for the $Z/\gamma^* \rightarrow e^+e^- + \geq 3$ jet sample.	147
86	Diem invariant mass distribution for the $Z/\gamma^* \rightarrow e^+e^- + \geq 4$ jet sample.	148
87	Diem invariant mass distribution for the $Z/\gamma^* \rightarrow e^+e^- + \geq 5$ jet sample.	149
88	Cross sections for inclusive jet multiplicities with statistical errors. . . .	150
89	$\pm 1\sigma$ fluctuation of the jet energy scale (JES 5.3)	152
90	Jet reco/ID efficiencies with errors plotted versus particle jet p_T smeared with data energy resolution (central).	154
91	Jet reco/ID efficiencies with errors plotted versus particle jet p_T smeared with data energy resolution (ICR).	155
92	Jet reco/ID efficiencies with errors plotted versus particle jet p_T smeared with data energy resolution (forward).	156
93	Comparing scale factors between the Top group and this analysis. Equivalent techniques were used in both cases.	157
94	Comparing “efficiency” of finding a recoiling jet as a function of Z p_T in data and MC.	158
95	Comparing jet resolution for JES 5.1 (upper curve) and JES 5.3 (lower curve) in the central region of the Calorimeter. The difference is approximately 5% over the whole range.	160
96	Exponential fit to the number of QCD events for different inclusive jet multiplicities.	168

LIST OF FIGURES (Continued)

<u>FIGURE</u>		<u>PAGE</u>
97	Cross sections for inclusive jet multiplicities in data (with total errors) compared with MCFM and CKKW.	173
98	Ratios of the $Z/\gamma^*(\rightarrow e^+e^-)+\geq n$ jet cross sections to the total inclusive $Z/\gamma^*\rightarrow e^+e^-$ cross section versus n . The errors on the data include the combined statistical and systematic uncertainties. The line (CKKW) represents the predictions of LO Matrix Element calculations using 12 _{PYTHIA} for parton showering and hadronization, normalized to the measured $Z/\gamma^*+\geq 1$ jet cross section ratio. The open circles represent the 12 _{MCFM} predictions.	174
99	Data to theory (ALPGEN+PYTHIA) comparison for the highest p_T jet distribution in the $Z+\geq 1$ jet sample, for the second highest p_T jet distribution in the $Z+\geq 2$ jet sample and for the third highest p_T jet distribution in the $Z+\geq 3$ jet sample. The errors on the data are only statistical.	175
100	L1 and L2 trigger elements. Horizontal arrows are indicating the dataflow.	192
101	Layout of Level 2 calorimeter (L2CAL) crate with main components.	195
102	Level 2 Alpha Board with Ethernet card and hard disk drive.	196
103	Block diagram of Level 2 Alpha Board.	197
104	Block diagram of the 21172 Core Logic Chipset.	199

LIST OF ABBREVIATIONS

AA	Alternative Algorithm
BR	Branching Ratio
CC	Central Calorimeter
CellNN	Cell Nearest Neighbor
CDF	Collider Detector at Fermilab
CERN	European Organization for Nuclear Research
CFT	Central Fiber Tracker
CHF	Coarse Hadronic Fraction
CIA	Control, Input/Output, Address
CKKW	Catani, Krauss, Kuhn, Webber
COOR	Central Coordination Process
CPLD	Complex Programmable Logic Device
CPS	Central Preshower
CPU	Central Processing Unit
CTEQ	Coordinated Theoretical-Experimental Project on QCD

LIST OF ABBREVIATIONS (Continued)

D0GSTAR	D0 GEANT Simulation of the Total Apparatus Response
DAQ	Data Acquisition
DEC	Digital Equipment Corporation
DMA	Direct Memory Access
DRAM	Dynamic Random Access Memory
DSW	Data Switch
EC	End Calorimeter
EM	Electro Magnetic
EMF	Electro Magnetic Fraction
FAMUS	Forward Angle Muon System
FIC	Fiber Input Converter
FIFO	First in, First out
FNAL	Fermi National Accelerator Laboratory
FPGA	Field Programmable Gate Array
FPS	Forward Preshower
FSR	Final State Radiation
GEANT	GEometry ANd Tracking
GWS	Glashow, Weinberg, Salam

LIST OF ABBREVIATIONS (Continued)

HotF	Hot Fraction
HTF	Histogramming Track Finder
ICD	Inter Cryostat Detector
ICR	Inter Cryostat Region
ISR	Initial State Radiation
IDE	Integrated Drive Electronics
I/O	Input/Output
ISA	Industry Standard Architecture
JES	Jet Energy Scale
L1	Level 1
L1Cal	Level 1 Calorimeter
L1CTT	Level 1 Central Track Trigger
L1Muon	Level 1 Muon
L2	Level 2
L2Cal	Level 2 Calorimeter
L2CTT	Level 2 Central Track Trigger
L2GBL	Level 2 Global
L2MUC	Level 2 Muon Central

LIST OF ABBREVIATIONS (Continued)

L2MUF	Level 2 Muon Forward
L2Muon	Level 2 Muon
L2PS	Level 2 Preshower
L2STT	Level 2 Silicon Track Trigger
L3	Level 3
L3DAQ	Level 3 Data Acquisition
LBN	Luminosity Block Number
Linac	Linear Accelerator
LL	Leading Logarithmic
LLA	Leading Log Approximation
MB	Minimum Bias
MBT	Magic Bus Transceiver
MBus	Magic Bus
MC	Monte Carlo
MCFM	Monte Carlo for FeMtobarn processes
MDT	Mini Drift Tube
MG	Massless Gap
MPM	Multi Port Memory

LIST OF ABBREVIATIONS (Continued)

NLO	Next-To-Leading Order
PCI	Peripheral Component Interconnect
PDF	Parton Distribution Function
PDT	Proportional Drift Tube
PIO	Programmed Input Output
PLD	Programmable Logic Device
PV	Primary Vertex
RF	Radio Frequency
RISC	Reduced Instruction Set Computing
ROM	Read Only Memory
QCD	Quantum Chromo Dynamics
QED	Quantum Electro Dynamics
QFT	Quantum Field Theory
SBC	Single Board Computer
SCL(init)	Serial Command Link (Initialize)
Scone	Simple Cone
SIMM	Single In-line Memory Module
SM	Standard Model

LIST OF ABBREVIATIONS (Continued)

SMT	Silicon Microstrip Tracker
SROM	Serial Read Only Memory
TCC	Trigger Control Computer
TDR	Technical Design Report
TOT	Total Energy
UV	Ultra Violet
VBD	VME Buffer Driver
VITA	VMEbus International Trade Association
VLPC	Visible Light Photon Counter
VME	VERSA Module Eurocard
WAMUS	Wide Angle Muon System

SUMMARY

We present a study of events with Z bosons and hadronic jets produced at the Tevatron in $p\bar{p}$ collisions at a center of mass energy of 1.96 TeV. The data consist of approximately 14,000 $Z/\gamma^* \rightarrow e^+e^-$ decay candidates from 343 pb^{-1} of integrated luminosity collected using the DØ detector. Cross sections and jet production properties have been measured for $Z/\gamma^* + \geq 0$ to 5 jet events. We find our results to be in good agreement with QCD predictions.

CHAPTER 1

INTRODUCTION

Since the discovery of the Z boson at CERN in 1983 (1; 2), the production of electroweak gauge bosons in association with jets has been of increasing importance. A measurement of the $Z + \geq n$ jets cross sections provides a good test for our understanding of quantum chromodynamics (QCD). In addition, hadronic production of the Z boson is a major background to many interesting physics processes. In particular, Higgs searches in the channel where Higgs bosons are being produced in association with Z boson, rely on a detailed understanding of the $Z + \geq n$ jets background.

Chapter 2 of this dissertation provides a short overview of the theoretical framework within which this analysis was performed. A description of the experimental apparatus, including the Fermilab chain of accelerators, and the DØ detector is given in Chapter 3. Chapter 4 describes the methods that are used to reconstruct physical objects from raw detector data. The Monte Carlo (MC) event generators that are used are illustrated in Chapter 4. Chapter 5 outlines all steps that lead to the $Z + \geq n$ jets cross section measurement. A brief summary of the final result, together with a discussion of future plans, is given in Chapter 6.

Throughout this dissertation (unless stated otherwise) we follow the customary convention by which $\hbar = c = 1$.

CHAPTER 2

THEORY

2.1 The Standard Model

The *Standard Model of Particle Physics* is the name given to the current theory of elementary particles and the forces that act between them. It is a quantum theory of fields (QFT), which arises when combining quantum mechanics with special relativity. The SM includes most of our current understanding of the laws of physics (except gravity), and has been verified experimentally to an extremely high level of accuracy.

Nevertheless, the theory is incomplete. The SM contains many free parameters that cannot be derived from first principles. The Higgs boson, which is considered to be the last remaining piece to the SM, still has not been experimentally detected. Most importantly, gravity is not included in the SM. A framework that consistently combines quantum mechanics with general relativity into a theory of *quantum gravity* has not been discovered yet.

The following is a brief overview of the SM, together with the particles and interactions that it describes (3; 4; 5; 6; 7; 8; 9).

2.1.1 Quarks and Leptons

In the SM the most fundamental particles that make up ordinary matter are divided into two groups: *quarks* and *leptons* (Figure 1, Reference (10)). Both quarks and leptons are *fermions* since they are spin- $\frac{1}{2}$ particles, and therefore obey Fermi-Dirac statistics. As indicated in

Figure 1, quarks and leptons are each arranged in three families, each family being identical except for the masses of its members. For each particle there exists an anti-particle with opposite charge.

There are six different types of quarks, labeled (in order of increasing mass) *up*, *down*, *strange*, *charm*, *bottom*, and *top*. It is remarkable to note that quarks are never observed as single particles (see Chapter 2.1.2.3), and that they carry fractional electrical charges¹ of $+\frac{2}{3}$ or $-\frac{1}{3}$. Quarks form bound states called *hadrons* by either combining three quarks into *baryons*, or by pairing a quark with an antiquark into *mesons*. Protons (made up of two up-quarks and one down-quark) and neutrons (made up of two down-quarks and one up-quark) are the most common examples for baryons. Pions ($\pi^{0,\pm}$) and Kaons (K^\pm , K^0 , \bar{K}^0) are the most common examples for mesons.

There are three different types of charged leptons, carrying a charge of -1: *electrons* (e^-), *muons* (μ^-), and *tau leptons* (τ^-). While electrons exist in all atoms, muons and tau leptons can only be observed in energetic processes like cosmic ray showers, or high energy particle collisions. There are three neutral leptons, called *neutrinos* (ν), each corresponding to a charged lepton: ν_e , ν_μ , and ν_τ .

2.1.2 Interactions

One of the most fundamental insights in theoretical physics is that interactions are dictated by symmetry principles. In QFT interactions manifest themselves by imposing symmetry con-

¹All charges are given in units of the absolute value of the electron charge, 1.602×10^{-19} Coulombs.

Leptons spin = 1/2			Quarks spin = 1/2		
Flavor	Mass GeV/c ²	Electric charge	Flavor	Approx. Mass GeV/c ²	Electric charge
ν_e electron neutrino	$<1 \times 10^{-8}$	0	u up	0.003	2/3
e electron	0.000511	-1	d down	0.006	-1/3
ν_μ muon neutrino	<0.0002	0	c charm	1.3	2/3
μ muon	0.106	-1	s strange	0.1	-1/3
ν_τ tau neutrino	<0.02	0	t top	175	2/3
τ tau	1.7771	-1	b bottom	4.3	-1/3

Figure 1. Quarks and leptons.

ditions on the quantum fields representing the respective interactions. Using the framework of Lagrangian field theory, we impose that the Lagrangian of the theory be invariant under a group of local phase changes (*local gauge invariance*). A local phase change means that the phase change depends on space and time in a completely arbitrary way. The Lagrangian is no longer invariant under such local phase changes. In order to preserve gauge invariance of the Lagrangian (on purely aesthetic grounds) we introduce an additional gauge field. Excitations of these gauge fields lead to force-carrying spin-1 bosons that mediate the interactions of nature.

Four types of interactions are currently known (in order of decreasing strength): strong, electromagnetic, weak, and gravitational. Figure 2 summarizes basic properties of the four interactions (10). Note that gravity has not been incorporated into the SM, since no QFT for gravitational interactions has been discovered yet. Additionally, gravity is simply too weak to have any significant influence on particle interactions.

QFT uses the tools of *perturbation theory*. Physical quantities like cross sections cannot be computed exactly, but they can be approximated to any desired precision. In practice, calculations are performed by drawing *Feynman diagrams*, which are graphical representations of the processes under consideration. As an example, Figure 3(a) and Figure 3(b) show two Feynman diagrams describing electron-positron annihilation with subsequent muon-antimuon pair production, $e^+e^- \rightarrow \gamma^* \rightarrow \mu^+\mu^-$. Both diagrams have the same initial and final state configuration. While Figure 3(a) shows the lowest order (*tree level*) diagram, Figure 3(b) has an additional photon loop connecting the final state muon-antimuon lines (*one-loop correction*). An infinite amount of higher order diagrams with additional loop corrections exists, and a full

calculation would have to take into account all of these diagrams. Every additional loop introduces additional factors of the coupling constant of the interaction. The physical quantity that needs to be evaluated based on these diagrams therefore forms a power series with successive terms containing higher powers of the coupling constant. If the coupling constant is small, higher order contributions become negligible, and the power series converges.

An additional problem arises from the fact that all possible energy-momentum values of the virtual loop particles must be considered as well. This can lead to infinities in the calculations, i.e. the final result is non-physical. The concept of *renormalization* solves this problem at a practical level. As an example, consider the electrical charge of the electron. Taking higher order loop diagrams into account, the power series evaluating the charge diverges. The idea behind renormalization assumes that the electric charge that is actually observed is the sum of the *bare* charge (due to the tree level process) plus the contributions of all higher order diagrams. We then assume a value for the bare charge that is infinite as well, but opposite to that part of the higher order corrections. In other words, the two infinite contributions cancel each other to yield the finite, experimentally observed result for the electrical charge of the electron. If for a given theory all infinities can be absorbed into the available free parameters, the theory is considered *renormalizable*.

Technically, in order to express a physical parameter like the electron charge in terms of the bare parameter, the introduction of an arbitrary scale called the *renormalization scale* (μ_R), is required. It is customary to set μ_R equal to the typical energy scale associated with the process of interest. Different choices for μ_R represent different *renormalization schemes*. The

Property \ Interaction	Gravitational	Weak (Electroweak)	Electromagnetic	Strong	
				Fundamental	Residual
Acts on:	Mass – Energy	Flavor	Electric Charge	Color Charge	See Residual Strong Interaction Note
Particles experiencing:	All	Quarks, Leptons	Electrically charged	Quarks, Gluons	Hadrons
Particles mediating:	Graviton (not yet observed)	$W^+ W^- Z^0$	γ	Gluons	Mesons
Strength relative to electromag for two u quarks at: for two protons in nucleus	10^{-41}	0.8	1	25	Not applicable to quarks
	10^{-41}	10^{-4}	1	60	
	10^{-36}	10^{-7}	1	Not applicable to hadrons	20

Figure 2. Interactions and their properties.

renormalization scale essentially removes physics beyond $\frac{1}{\mu_R}$ from perturbative calculations, including diverging loop corrections (*UV divergences*) and interesting short distance physics (quantum gravity). The coupling constant of the interaction and the coefficients of the perturbative expansions become a function of μ_R , although ultimately (calculating them to infinite orders) they are independent of μ_R . One can exploit this fact to calculate the effective variation of physical constants with changes in scale, also known as the *renormalization group*.

The following is a brief summary of the interactions that have been incorporated into the SM.

2.1.2.1 Electromagnetic Interaction

Historically, the electromagnetic interaction was the first to be formulated in the framework of a renormalizable QFT by Tomonaga, Feynman, and Schwinger in the 1940s (Nobel Prize in 1965). All subsequent efforts to create theories for other interactions are modeled on it. *Quantum Electrodynamics* (QED) describes the electromagnetic interaction by requiring gauge

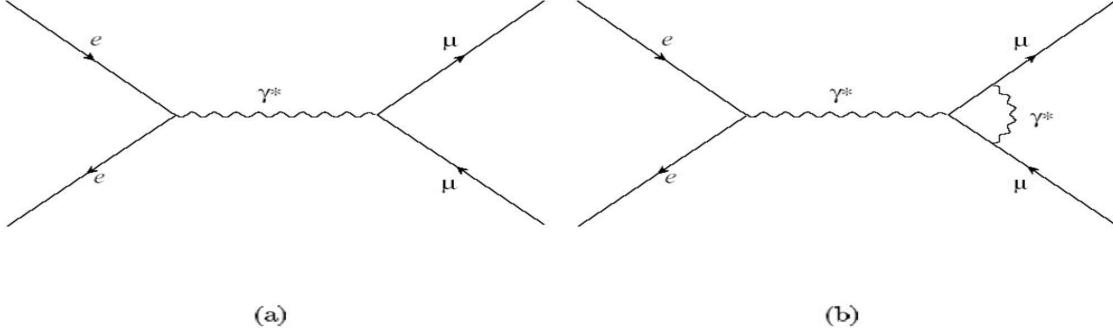


Figure 3. Feynman diagram for the process $e^+e^- \rightarrow \gamma^* \rightarrow \mu^+\mu^-$. (a) Tree level diagram. (b) One-loop diagram.

invariance under $U(1)$ group transformations. $U(1)$ denotes a group of unitary one-dimensional matrices, describing space-time dependent rotations in a complex plane. The requirement of gauge invariance gives rise to the photon field and the *photons* as the corresponding mediator of the electromagnetic interaction. Because the photon is massless the interaction is long range. The photon couples to all particles that carry electrical charge, like quarks and charged leptons. The strength of the coupling is proportional to the magnitude of the dimensionless *finestructure coupling constant*:

$$\alpha_{EM} = \frac{e^2}{4\pi} \approx \frac{1}{137} \quad (2.1)$$

2.1.2.2 Weak Interaction

The weak interaction is most prominent in *beta decays* (Equation 2.2 and Equation 2.3) and associated radioactivity.

$$n \rightarrow p + e^- + \bar{\nu}_e \quad (2.2)$$

$$p \rightarrow n + e^+ + \nu_e \quad (2.3)$$

The range of the interaction is short due to the high mass of the mediating gauge bosons (W^\pm , Z^0):

$$m_{W^\pm} \approx 80 \text{ GeV} \quad (2.4)$$

$$m_{Z^0} \approx 91 \text{ GeV} \quad (2.5)$$

A QFT combining the electromagnetic with the weak interaction was first developed by Glashow, Weinberg, and Salam (*GWS theory*, Noble Prize in 1979). Later 't Hooft and Veltman were able to prove that the theory is renormalizable (Nobel Prize in 1999). Electroweak theory combines a new U(1) group with an SU(2) group, and requires invariance under $SU(2) \otimes U(1)$ transformations. SU(n) describes groups of special¹ and unitary $n \times n$ matrices. Local gauge invariance under SU(2) group transformations introduces three massless spin-1 gauge bosons W^+ , W^- , and W^0 . Adding the U(1) group introduces another gauge boson called B^0 . The

¹The determinant of the matrices must be 1.

W^0 and B^0 mix quantum mechanically to give rise to the experimentally observed photon (γ) and Z^0 :

$$\gamma = W^0 \sin \theta_W + B^0 \cos \theta_W \quad (2.6)$$

$$Z^0 = W^0 \cos \theta_W - B^0 \sin \theta_W \quad (2.7)$$

where θ_W is called the *weak mixing angle* or *Weinberg angle*. As opposed to QED, the underlying group of the electroweak theory is *non-Abelian* since not all the generators of the group commute with each other, which allows for self interaction between the gauge bosons.

Up to this point the electroweak theory is very simple and elegant. Yet it is incomplete, since all gauge bosons of the theory are massless. However, we know from experiment that the W and Z bosons are heavy (Equation 2.4 and Equation 2.5). Additionally, mass terms cannot be introduced into the Lagrangian describing the system, since this generates unrenormalizable divergences which make the theory unphysical. This problem is resolved by a process known as *electroweak symmetry breaking*.

Electroweak symmetry breaking is achieved by introducing a new field, the Higgs field Φ , where Φ is an $SU(2)$ doublet of complex scalar fields:

$$\Phi = \begin{pmatrix} \Phi^+ \\ \Phi^0 \end{pmatrix} \quad (2.8)$$

The simplest and most general Lagrangian for the Higgs field, consistent with SU(2) gauge symmetry, is:

$$\mathcal{L}_{Higgs} = (\partial_\mu \Phi)^\dagger (\partial^\mu \Phi) - \mu^2 \Phi^\dagger \Phi - \lambda (\Phi^\dagger \Phi)^2 \quad (2.9)$$

where the first term contains the Higgs field kinetic energy and gauge interactions, and the remaining terms describe the Higgs potential (Figure 4). SU(2) symmetry is spontaneously broken by requiring that the minimum of the Higgs potential lies not at zero, but on a circle of minima:

$$\langle \Phi^0 \rangle = \frac{\mu}{\sqrt{2\lambda}} = \frac{v}{\sqrt{2}} \quad (2.10)$$

where v is the Higgs field vacuum expectation value, $v \approx 246$ GeV. Replacing Φ in Equation 2.9 with $\Phi = (0, v/\sqrt{2})$, results in the W and Z bosons acquiring mass through interaction with the Higgs field.

Excitations of the Higgs field give rise to a particle known as the *Higgs boson*. The mass of the Higgs boson is not known, and the particle has not been observed in experiments yet.

2.1.2.3 Strong Interaction

Quantum Chromo Dynamics (QCD) is the QFT describing the strong interaction. It is based on an SU(3) gauge field, which leads to 8 mediating massless gauge bosons called *gluons*. Strongly interacting particles like quarks and gluons carry a new type of charge called *color*. Each (anti)quark can carry a (anti)red, (anti)green, or (anti)blue color charge. Gluons carry a combination of a color and anticolor charge. The fact that gluons are themselves carriers of the color charge allows them to couple to each other. This essentially derives from the non-Abelian

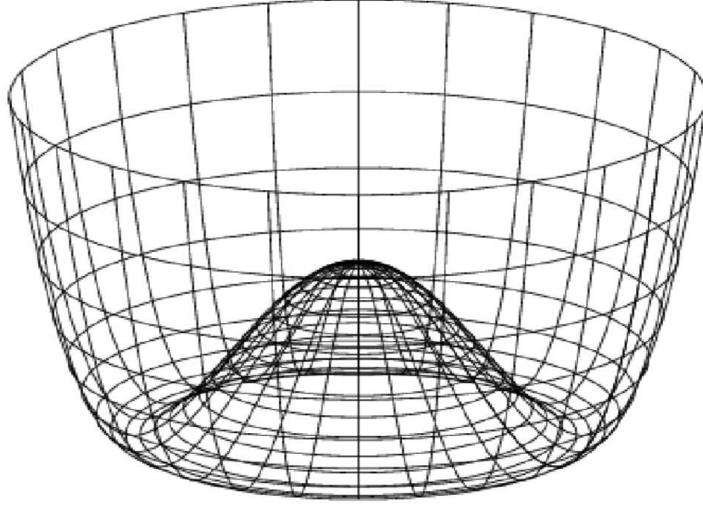


Figure 4. The Higgs potential.

character of the gauge theory. Quarks and gluons are collectively referred to as *partons*.

One interesting feature of QCD is the fact that the strength of the strong coupling increases with decreasing energy scale, i.e. at low energies and long distances the interaction becomes too strong to be treated within the framework of perturbation theory. This leads to the idea of *confinement*, which assumes that all objects carrying color can never be found as free particles in nature and that they are confined into color-neutral composite hadrons. Colors can be combined into color-neutral objects in two ways: a colored quark combined with an antiquark of the corresponding anticolor (meson), or a combination of three (anti)quarks each carrying

a different (anti)color (baryon)¹. This essentially confines quarks to a small region near one another. The quarks that combine into baryons or mesons are referred to as *valence quarks*. They constantly interact with each other by exchanging gluons. Since gluons can couple to each other, they can emit more gluons that can further split into virtual quark-antiquark pairs called *sea quarks*.

Another important consequence of confinement is the fact that quarks and gluons are observed experimentally as *jets* of color-neutral hadrons. This means that if a single parton emerges from a particle collision, gluons will be radiated which subsequently produce quark-antiquark pairs, which ultimately combine into a jet of hadrons moving in the direction close to that of the original parton. This process is called *hadronization*.

As the energy scale increases, the strength of the strong coupling decreases. This has the consequence that partons behave like free particles at energies that are typical of modern high-energy experiments. This is called *asymptotic freedom*. Theoretical work on asymptotic freedom by Gross, Politzer, and Wilczek was rewarded with the 2004 Nobel Prize.

In practice, when calculating partonic cross sections, perturbative (high energy, small distance) and non-perturbative (low energy, large distance) regions of parameter space are separated in energy by the *factorization scale*, μ_F . The non-perturbative regime is described by *Parton Distribution Functions* (PDF). PDFs parameterize the momentum distributions of partons within the proton and are determined experimentally from deep inelastic scattering

¹Several experiments since 2003 claim to have seen a *pentaquark* which would combine four quarks and one antiquark.

experiments. When calculating cross sections beyond leading orders in perturbation theory, additional loops (*virtual corrections*) and external lines (*real corrections*) need to be included. Higher order corrections will lead to divergences in the soft and collinear limits of parton emission. When calculating fully inclusive quantities, finite results can be obtained since divergences due to the virtual and real corrections cancel. These divergences do not cancel exactly when more exclusive quantities are calculated. Logarithmic terms that become large in the soft and collinear limit need to be treated using a technique known as *resummation*. Leading Logarithmic (LL) terms of the form $(\alpha_s \ln)^n$, where α_s is the strong coupling constant, can be summed to all orders in perturbation theory to yield finite results. This is known as the Leading Log Approximation (LLA).

2.2 $Z/\gamma^* (\rightarrow e^+e^-) + \geq n$ Jets

The production of Z/γ^* gauge bosons in association with jets of hadronic particles provides a good opportunity to test perturbative QCD predictions at large momentum transfers. Physical quantities in QCD are generally expressed as perturbative expansions in the strong coupling constant, by separating processes at different orders of α_s . Figure 5 shows one of the leading-order (LO) processes that produces a Z boson with an associated jet. The decay of the Z/γ^* gauge bosons into pairs of electrons (e^-) and positrons (e^+) provides an efficient way to identify candidate events with low background contamination.

In this analysis we study Z/γ^* gauge boson production and test the reliability of perturbative QCD predictions over a range of jet energies and jet multiplicities. The results are compared to state-of-the-art MC event simulations, representing LO and next-to-leading order

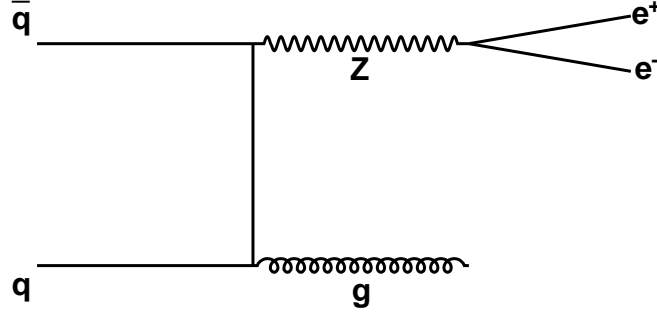


Figure 5. Feynman diagram for one of the leading-order processes that produces a Z boson with an associated jet coming from a gluon.

(NLO) QCD calculations. A description of the MC event generators that were used is given in Chapter 5.

The production of Z/γ^* gauge bosons in association with jets is also an important background process relevant for Higgs boson searches. One of the dominating Higgs production modes at the Tevatron involves the generation of a Higgs boson in association with a Z boson (Figure 6). The study of jet properties and cross sections for processes that generate similar final state particles (Figure 7), allows a more precise distinction between a possible Higgs signal and QCD background.

The analysis presented in this dissertation was performed with the $D\bar{O}$ detector at the Fermilab proton-antiproton Tevatron collider. The following chapter gives an overview of the experimental apparatus that was used for this analysis.

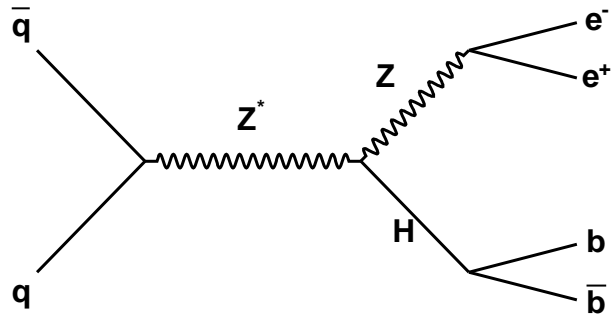


Figure 6. SM Higgs boson production in association with a Z boson (*Higgsstrahlung*).

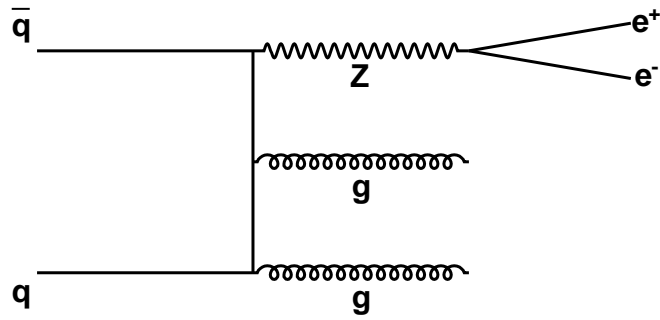


Figure 7. Z boson generation in association with two gluons.

CHAPTER 3

EXPERIMENTAL APPARATUS

The Fermi National Accelerator Laboratory (FNAL, or Fermilab) currently operates the world's highest energy proton-antiproton collider, the *Tevatron*. In this chapter we describe the chain of accelerators that is necessary to achieve a center-of-mass collision energy of 1.96 TeV. We also give an overview of the DØ detector which is built around one of the collision regions where protons and antiprotons collide.

The data used in this analysis was recorded with the DØ detector during the data taking period known as Run II, which officially began in March 2001.

3.1 The Fermilab Accelerators

The Tevatron is the final stage in a sequence of seven accelerators (11; 12; 13). A Cockcroft-Walton *preaccelerator*, a linear accelerator (*Linac*) and a synchrotron (*Booster*) provide a source of 8 GeV protons. The antiproton *Debuncher* and *Accumulator* are two components of the *Antiproton Source*. The *Main Injector* serves as the final boosting stage before injecting protons and antiprotons into the Tevatron. It also provides the necessary source of energetic protons which are needed in the Antiproton Source.

Figure 8 gives an overview of the Fermilab accelerator complex (14).

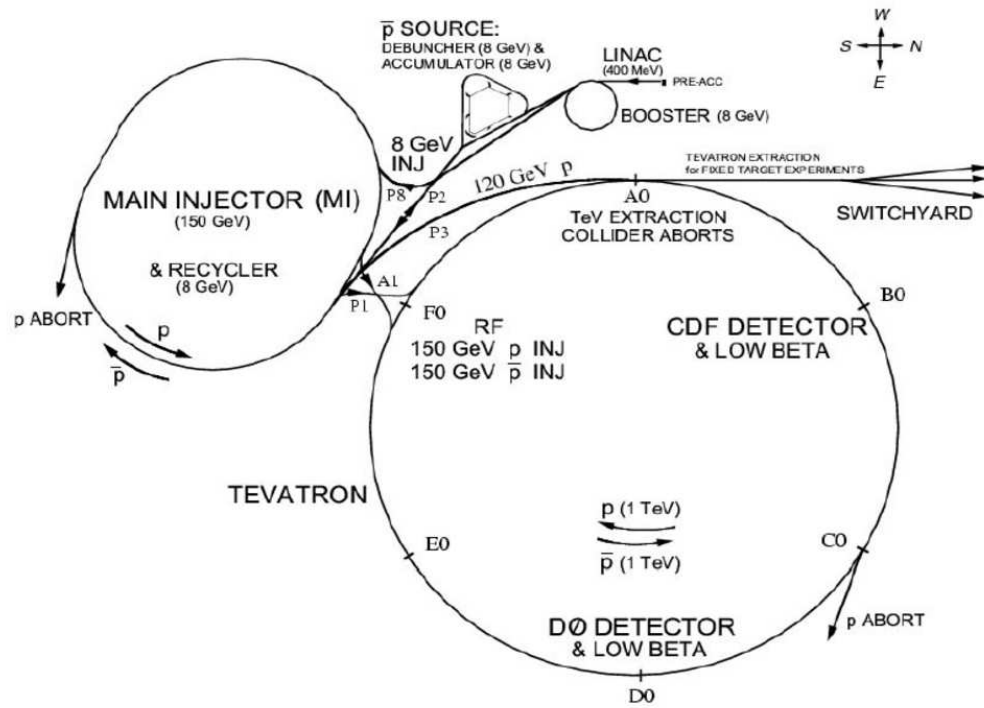


Figure 8. Schematic view of the Fermilab accelerator chain.

3.1.1 The Preaccelerator

The purpose of the preaccelerator is to produce negatively charged hydrogen ions (H^-) with an energy of 750 keV, which are then transferred into the Linac.

Hydrogen gas (H_2) enters a magnetron surface-plasma source (Figure 9). Due to the electric field between the anode (negatively charged) and cathode (positively charged) the electrons are stripped away from the hydrogen atoms to create a plasma. The positively charged hydrogen ions then strike the surface of the cathode to collect extra electrons and thereby form negatively charged hydrogen ions. The H^- ions are extracted through the anode aperture with an electric field of 18 kV applied by the extractor plate (see Figure 9).

A commercial Cockcroft-Walton Generator produces a 750 kV potential differential by charging capacitors in parallel from an AC voltage source and discharging them in series, via diodes ¹. The Cockcroft-Walton Generator is used to further accelerate the H^- ions to an energy of 750 keV.

After exiting the Cockcroft-Walton device the H^- ions travel through a transfer line. Before entering into the Linac the continuous stream of H^- ions passes through a single gap radio frequency (RF) cavity which bunches the beam at the RF frequency of the Linac.

3.1.2 The Linac

The Linac receives bunches of 750 keV H^- ions from the preaccelerator and accelerates them further to an energy of 400 MeV using RF cavities (Figure 10). The RF cavities are contained

¹The maximum voltage is limited by how much the air can “stand off” before sparking.

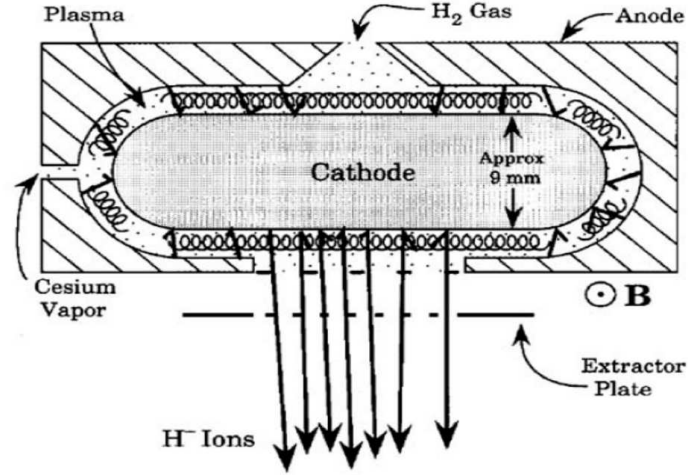


Figure 9. Basic configuration of a magnetron.

within a collection of steel tanks which are holding a sequence of drift tubes separated from each other by gaps. In order to accelerate H^- ions the cavities are designed in such a way that particles traveling in the gaps experience an acceleration, while particles traveling in the drift tubes are shielded from the RF.

After passing through the Linac, bunches of 400 MeV H^- ions are transferred into the Booster.

3.1.3 The Booster

The Booster is the first synchrotron in the chain of acceleration. It consists of a sequence of dipole and quadrupole magnets and 17 RF cavities arranged in a circle with a diameter of 151 m. The Booster accelerates protons to an energy of 8 GeV.

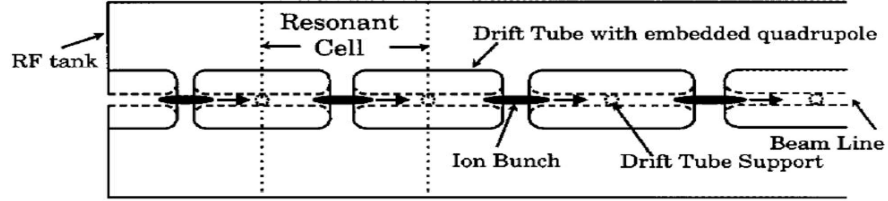


Figure 10. Schematic of Linac RF cavity.

It is easier to merge negatively charged H^- ions coming from the Linac with protons (H^+ ions) circulating in the Booster due to their opposite charge. Therefore the two beams are merged with the help of dipole magnets and the electrons are stripped from the H^- ions by letting the combined beam pass through a carbon foil.

Once the Booster is filled with proton bunches the RF cavities provide an acceleration up to 8 GeV. At the same time the field strength in the dipole magnets is adjusted accordingly in order to maintain a constant radius for the circulating particles. Once the protons have reached an energy of 8 GeV they are transferred into the Main Injector.

3.1.4 The Main Injector

The Main Injector is a circular synchrotron with a diameter of 1 km. It can accelerate both protons (coming from the Booster) and antiprotons (coming from the Antiproton Source) from 8 GeV to 150 GeV, before injecting them into the Tevatron. It also delivers 120 GeV protons to the Antiproton Source.

Historically the Main Injector was built for Run II in order to replace the Main Ring.

The fact that both the Main Ring and the Tevatron occupied the same tunnel led to several problems. First, overpasses for the DØ and CDF detectors had to be built for the Main Ring. Second, due to their close proximity the Tevatron beam was influencing the Main Ring beam. Consequently the Main Injector was built next to the Tevatron using a separate tunnel.

3.1.5 The Antiproton Source

The Antiproton Source consists of three major components: the *Target Station*, the *Debuncher*, and the *Accumulator*. In the first step the Target Station receives 120 GeV protons from the Main Injector and diverts them onto a Nickel Target. This produces a shower of secondary particles (including antiprotons) at many different angles and large spread in particle momentum. A Lithium lens and bending magnets are used to focus the beam and remove positively charged particles (Figure 11, and Reference (15)). A process called *stochastic cooling* is used in both the Debuncher and Accumulator in order to reduce the spread in momentum and position of the antiprotons and thereby “cooling” them.

Both the Debuncher and Accumulator are located in a rounded-triangle shaped tunnel with a circumference of about 51 m. Antiprotons coming from the Target Station are transferred into the Debuncher where the momentum spread of the particles is reduced. It is technically very challenging to accumulate a large quantity of antiprotons. On average for every 1 million protons that hit the Nickel target, only about 20 antiprotons can be gathered. Therefore the Accumulator stores antiprotons till a sufficient amount has been generated that can be transferred into the Main Injector. The Accumulator must be capable of storing antiprotons over many hours.

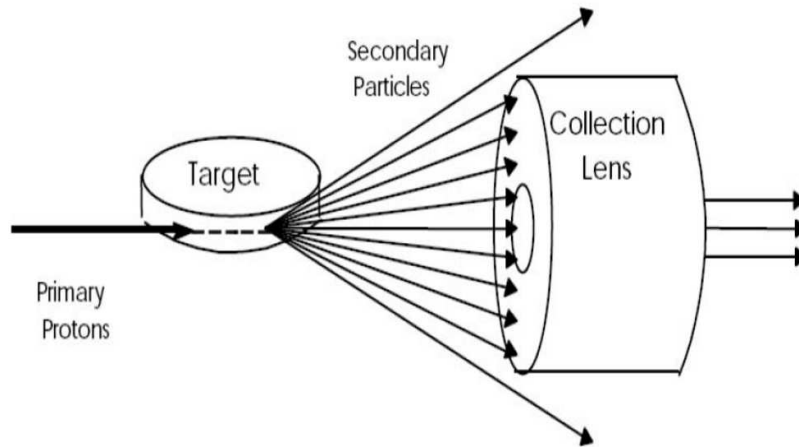


Figure 11. Simplified drawing of anti-proton production with nickel target and lithium lens.

3.1.6 The Tevatron

The Tevatron is the final stage in the sequence of proton and antiproton acceleration. It has a diameter of 2 km and uses superconducting magnets which operate at liquid helium temperature providing magnetic fields of up to 4 T. Protons and antiprotons are accelerated to 980 GeV, leading to a center-of-mass collision energy of 1.96 TeV.

36 bunches of protons and antiprotons travel in opposite directions and share the same beam pipe. Collisions occur every 396 ns at the DØ interaction point.

3.2 Luminosity and Cross Section

Luminosity \mathcal{L} is a measure of particle flux per unit area and per unit time ($\text{cm}^{-2}\text{s}^{-1}$). In a collider experiment such as DØ it gives an indication of how many proton-antiproton collisions (events) occur in a given time and area. The luminosity is determined by measuring the rate of inelastic proton-antiproton scatterings, which have a known cross section (16).

The cross section σ is a measure of the interaction probability per unit flux. Cross sections are usually expressed in *barns*, where $1 \text{ barn} = 10^{-24} \text{ cm}^2$.

The number of times a given process occurs, N , is proportional to \mathcal{L} and σ :

$$N = \sigma \cdot \int \mathcal{L} dt \quad (3.1)$$

$\int \mathcal{L} dt$ is called *integrated luminosity*. Figure 12 shows the integrated luminosity profile of the Tevatron, covering the data-taking period from April 2002 till March 2005. A total integrated luminosity of 343 pb^{-1} was used for the result presented in this analysis.

3.3 The DØ Detector

The DØ detector (Figure 13, and References (17; 18)) has a magnetic central-tracking system, consisting of a silicon microstrip tracker (SMT) and a central fiber tracker (CFT), both located within a 2 T superconducting solenoidal magnet. Central and forward preshower detectors are located just outside of the superconducting coil. A liquid-argon/uranium calorimeter has a central section (CC) covering pseudorapidities $|\eta|$ up to ≈ 1 , and two end calorimeters (EC) extending coverage to $|\eta| \approx 4$, all three housed in separate cryostats. A muon system

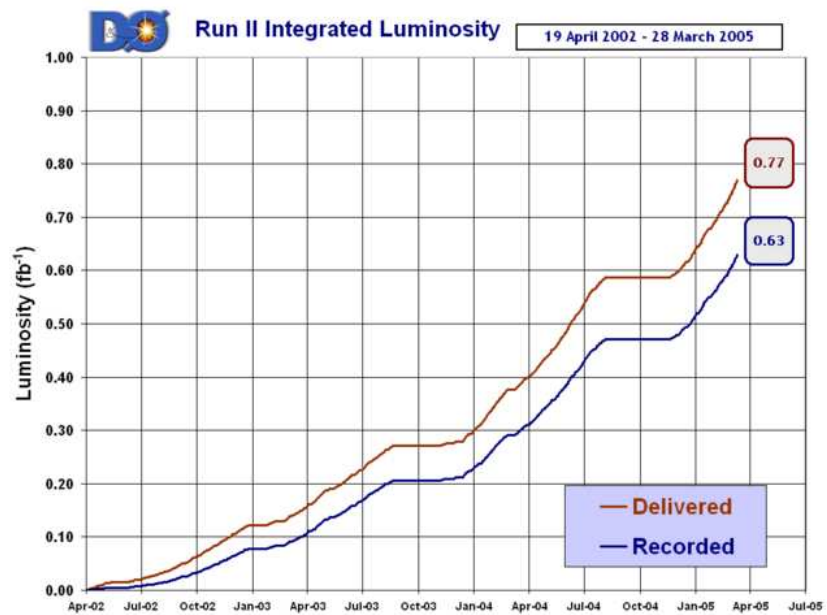


Figure 12. Tevatron integrated luminosity delivered to DØ (April 2002 - March 2005).

resides beyond the calorimetry, and consists of a layer of tracking detectors and scintillation trigger counters before 1.8 T toroids, followed by two more similar layers after the toroids. Luminosity is measured using plastic scintillator arrays located in front of the EC cryostats. The trigger and data acquisition systems are designed to accommodate the high luminosities of Run II.

3.3.1 Coordinate Systems

The coordinate system used for the DØ detector is right-handed. It has the positive z -axis aligned with the direction in which the protons travel and the positive y -axis pointing upwards.

In most cases cylindrical coordinates are used (z, Φ, θ) . Φ is the azimuthal angle in the plane perpendicular to the beam (z -axis), where $\Phi=0$ coincides with the positive x -axis. θ is the polar angle relative to the positive z -axis.

Since the colliding protons and antiprotons can exhibit a significant net boost along the z -axis it is suitable to choose a polar angle quantity that is invariant under relativistic transformations. Therefore it is often more convenient to use pseudorapidity η instead of the polar angle θ :

$$\eta = -\ln \cdot \left[\tan \frac{\theta}{2} \right] \quad (3.2)$$

The pseudorapidity approximates the true rapidity,

$$y = \frac{1}{2} \cdot \ln \left[\frac{E + p_z}{E - p_z} \right] \quad (3.3)$$

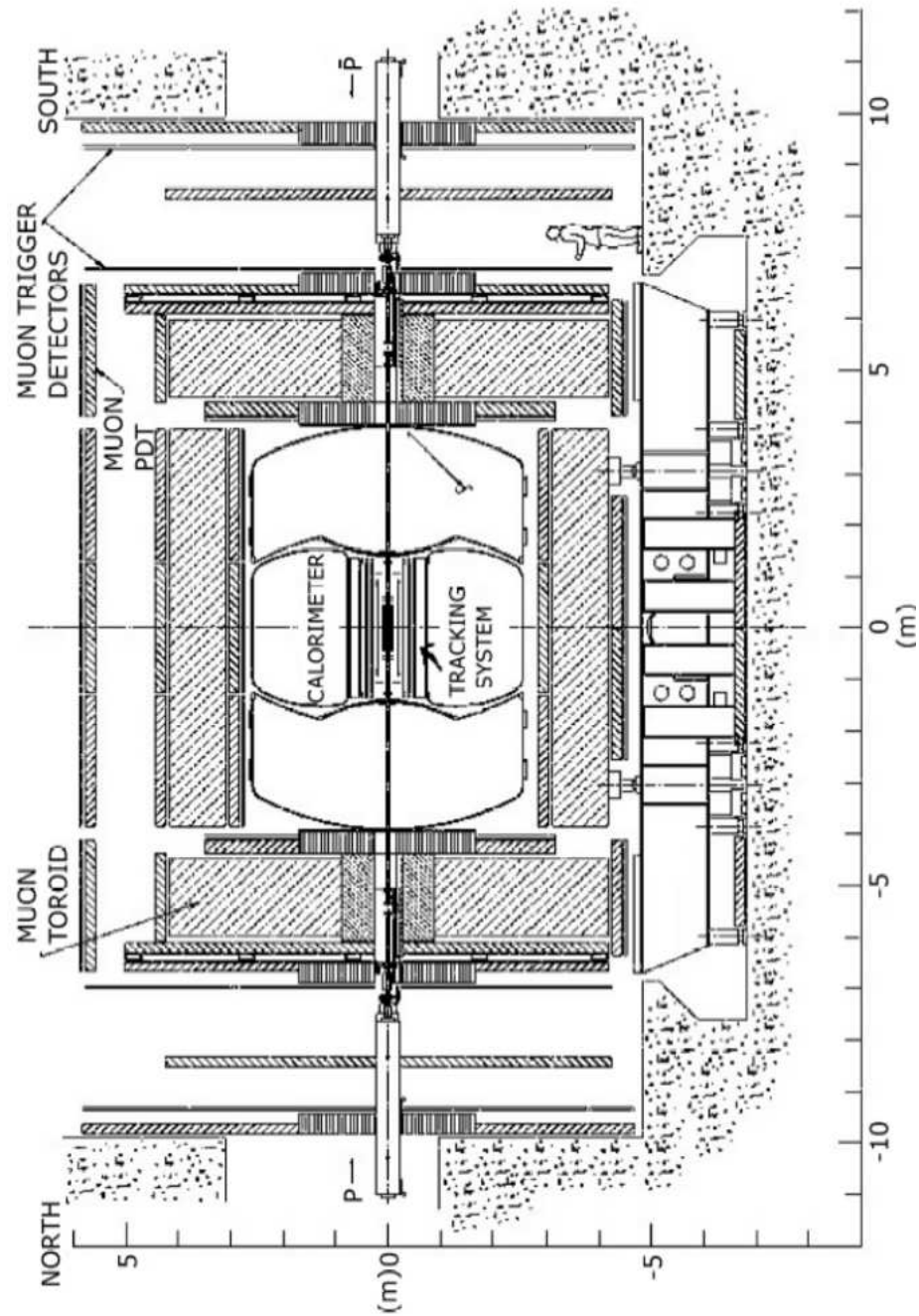


Figure 13. Schematic view of the DØ detector.

in the limit of $m \ll E$ (where m is the invariant mass $m^2 = E^2 - p^2$). We use the term “forward” to describe regions at large $|\eta|$.

In many cases some of the products of a proton-antiproton collision escape along the beam pipe, which makes it difficult to measure momentum components along the z -axis accurately. Therefore it is more convenient to use the momentum vector projected onto a plane perpendicular to the beam axis (*transverse momentum*):

$$p_T = p \cdot \sin\theta. \quad (3.4)$$

In a similar fashion we define *transverse energy* as

$$E_T = E \cdot \sin\theta. \quad (3.5)$$

3.3.2 Central Tracking System

The central tracking system is essential in measuring the position of the primary interaction vertex with high accuracy, which subsequently allows good measurement of lepton p_T , jet E_T and missing transverse energy (\cancel{E}_T). It also allows to detect the presence of b -quarks through the measurement of displaced vertices.

The Central Tracking System consists of the silicon microstrip tracker (SMT), the central fiber tracker (CFT) and the superconducting solenoid (Figure 14). Combining information from both SMT and CFT the primary vertex resolution is approximately $35 \mu\text{m}$ along the beam-

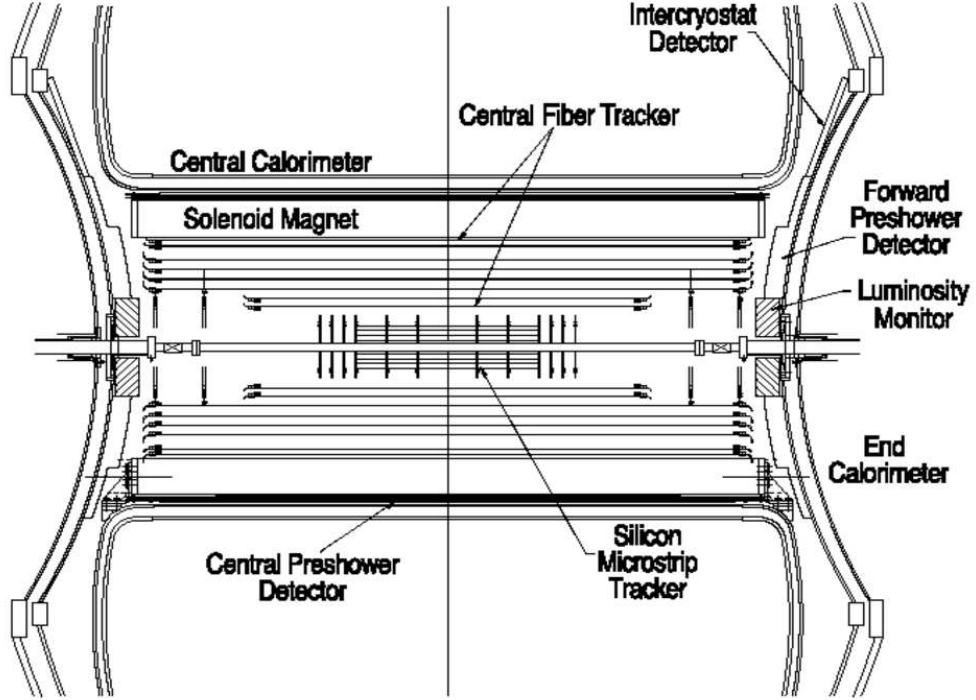


Figure 14. The DØ central tracking system with with solenoid, preshower detectors, luminosity monitor, and calorimeter.

line. Jets originating from the decay of b -quarks can be measured with an impact parameter resolution of less than $15 \mu\text{m}$ in $r - \Phi$.

3.3.2.1 Silicon Microstrip Tracker

In order to be able to detect the paths of charged particles emerging from a proton-antiproton collision, the SMT (19) uses wafers of silicon with a thickness of $300 \mu\text{m}$. When a charged particle passes through a $p - n$ junction in silicon it produces electron-hole pairs that

can be separated by an applied voltage. The charge which is collected can then be stored in capacitors and later read-out and digitized. The SMT contains a total of approximately 800,000 individual silicon detectors. Figure 15 shows the design of a basic silicon detector unit (*ladder*).

The SMT is designed in such a way that tracks of charged particles are perpendicular to detector material over a large range of η values. The structure of the device is mostly dictated by the fact that the interaction region is spread out with respect to the center of the detector ($\sigma \approx 25$ cm). This leads to a design of barrel modules combined with disks in the center and larger disks in the forward region (Figure 16). The SMT has six barrels along the z -axis, each containing four detector layers with a maximal outer radius of 10.5 cm. There are twelve small diameter double-sided “F” disks and four large diameter single-sided “H” disks to cover the far forward region ($|\eta| < 3$). The F-disks are at $|z| = 12.5, 38.2, 43.1$ and 53.1 cm. The centers of the H-disks are located at $|z| = 100.4, 121.0$ cm.

3.3.2.2 Central Fiber Tracker

The Central Fiber Tracker (CFT) (20) is located in between the SMT and the solenoid magnet. The purpose of the CFT is to improve the detection of charged particle tracks within $|\eta| < 2$. It consists of approximately 70,000 scintillating fibers mounted on eight concentric support cylinders with inner and outer radii of 20 and 52 cm, respectively. Each cylinder carries two layers of fibers running parallel to the beampipe (*axial layers*), and two layers of fibers oriented at small angles of $\pm 3^\circ$ (*stereo layers*) (Figure 17). The scintillating fibers have a diameter of $835 \mu\text{m}$ and are composed of a scintillating core surrounded by a layer with a high index of refraction, which leads to total internal refraction.

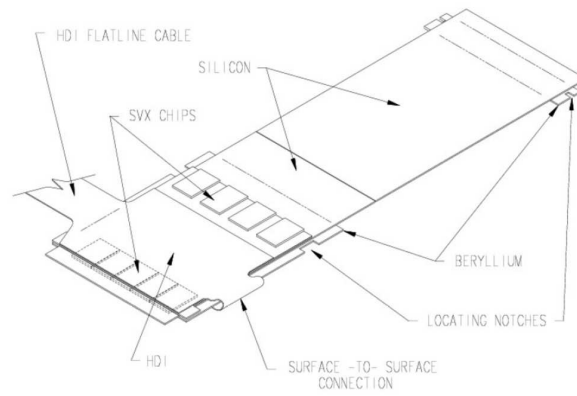


Figure 15. Double-sided ladder design, n-side.

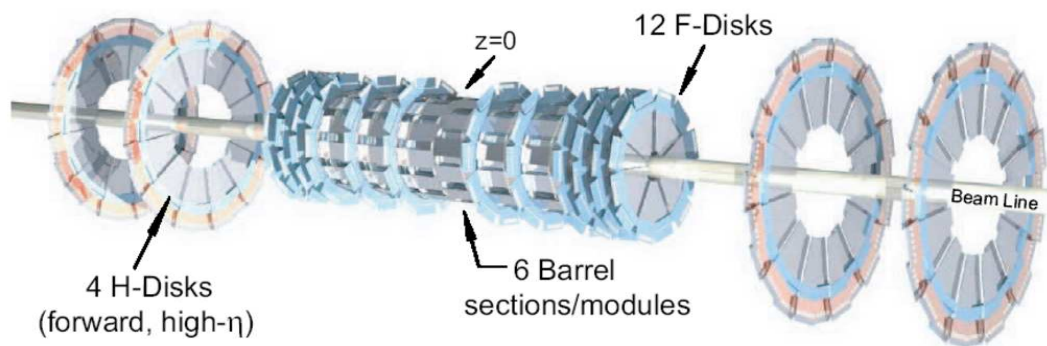


Figure 16. SMT disk and barrel design.

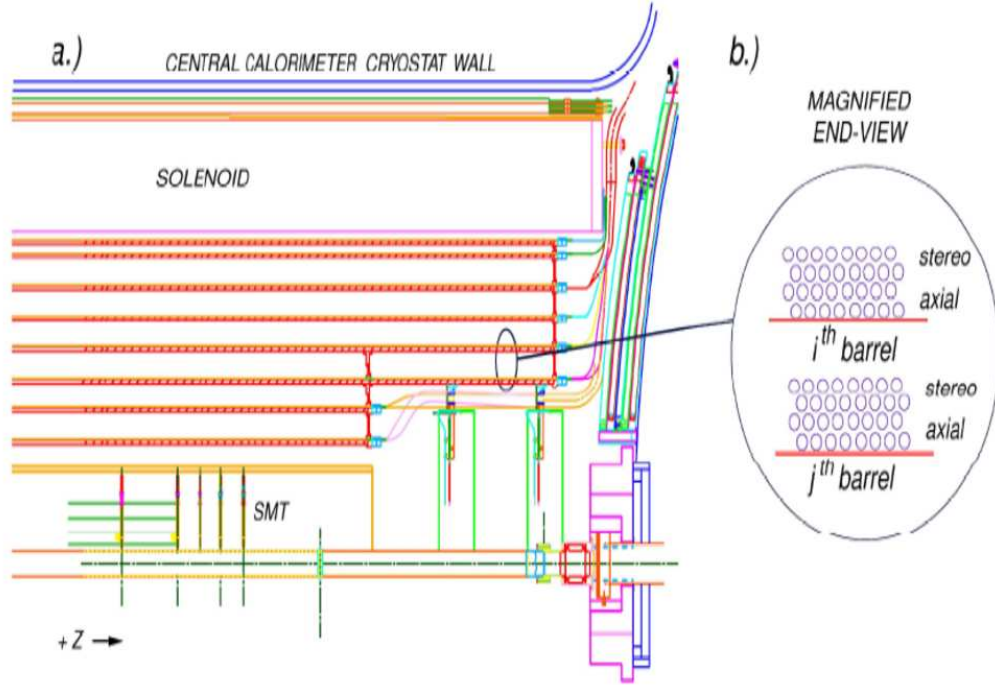


Figure 17. a) Location of the Central Fiber Tracker (CFT). b) Closeup view of axial and stereo layers.

Charged particles passing through a scintillating fiber excite the molecules in the fiber which subsequently release photons in the yellow-green part of the visible light spectrum as they relax to their ground states. Clear fiber waveguides carry the scintillation light to visible light photon counters (VLPCs) that convert the light into electrical signals. The VLPCs are silicon avalanche photodetectors that operate at liquid helium temperature in order to reduce the background due to electronic noise.

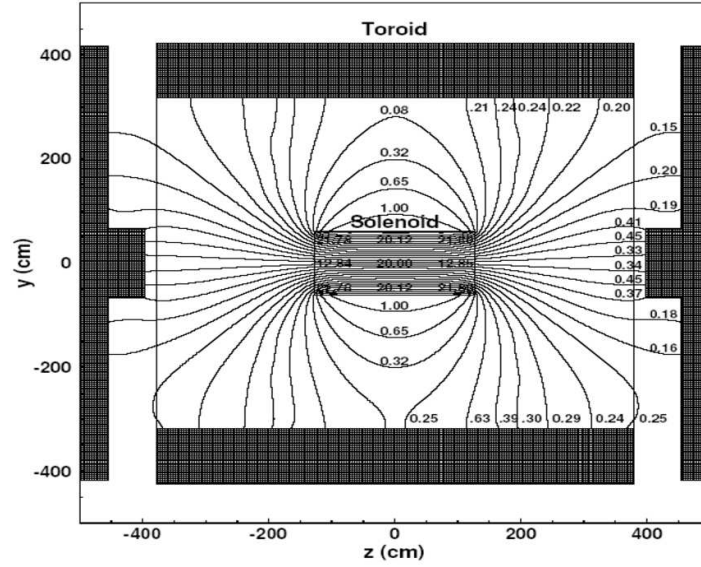


Figure 18. $y - z$ view of the DØ magnetic field with both the toroid and solenoid magnets at full current. Numbers are in kG (10 kG = 1 T).

3.3.2.3 Solenoidal Magnet

The superconducting solenoidal magnet significantly improves the capabilities of the DØ detector with regard to the detection of charged particle tracks and momentum resolution. The location and physical size of the magnet are constrained by the available space between the inner tracking system and the vacuum vessel of the central calorimeter. The magnet has a length of 2.73 m and a diameter of 1.42 m and provides uniform field of 2 T (20 kG) over most of the region covered by the inner tracking system (Figure 18). Figure 19 shows a perspective view of the solenoid inside the central calorimeter with its chimney and control dewar.

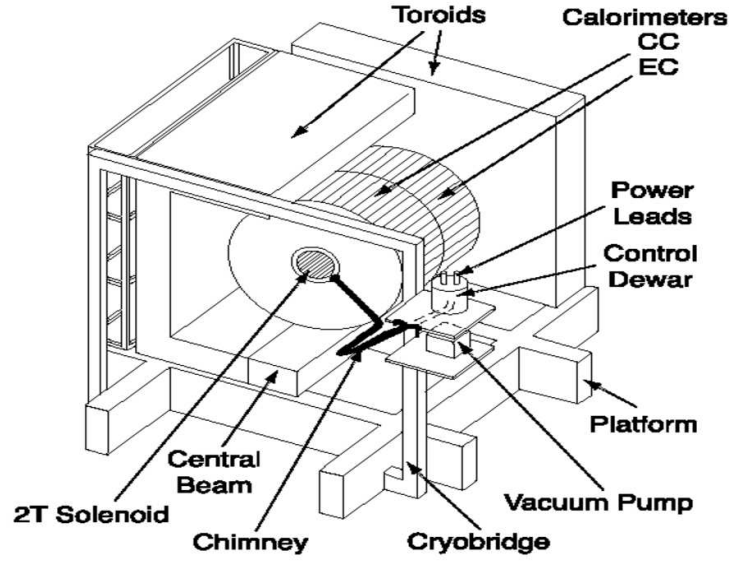


Figure 19. Perspective view of the solenoid inside the central calorimeter.

3.3.3 Preshower Detectors

The preshower detectors (21; 22) are designed to improve the identification of electrons and background rejection. By the time a charged particle has reached the preshower detectors it has already passed through several detectors as well as other upstream material like cables and support structures. The preshower detectors allow to correct for upstream energy losses in the offline event reconstruction. Due to their fast response time the preshower detectors can also be used for Level 1 triggering (see Chapter 3.4.1).

Scintillators are used to detect both position and energy of charged particles. In contrast to the scintillators used in the CFT, preshower scintillators are triangular shaped (Figure 20).

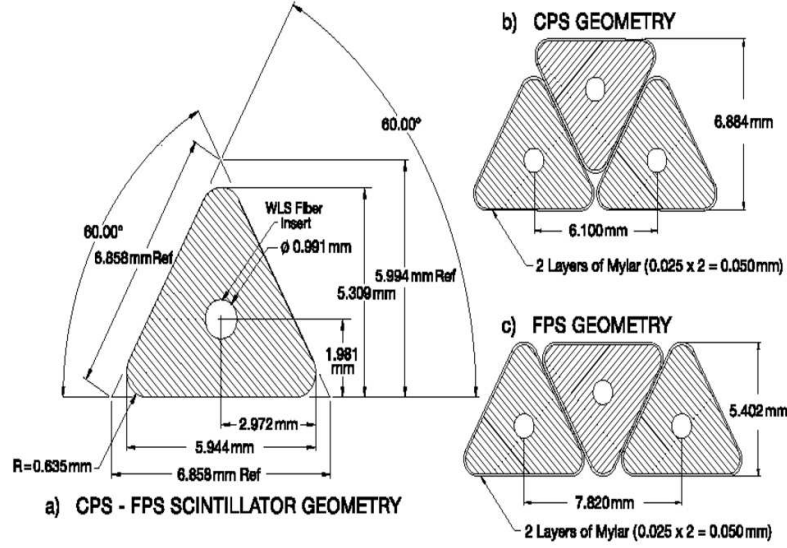


Figure 20. Cross section and layout geometry of the CPS and FPS scintillator strips.

This allows to arrange layers of scintillators without creating any dead space and thereby improving the accuracy of position measurements. The center of each scintillator carries a wavelength-shifting fiber which collects the light created by passing charged particles. The light is transmitted via clear fibers to VLPCs for readout.

3.3.3.1 Central Preshower Detector

The Central Preshower Detector (CPS) is located in the 5 cm gap between the solenoid and the central calorimeter, covering the region $|\eta| < 1.3$ (Figure 14). It consists of a layer of lead radiator which has a thickness corresponding to approximately one radiation-length (X_0), followed by three layers of triangular scintillator strips. The purpose of the lead radiator is to

ensure that the total amount of material encountered by a passing particle is constant at all pseudorapidities. The scintillating layers are arranged in an axial- u - v geometry, with a u stereo angle of 23.8° and a v stereo angle of 24.0° . Each layer has a total number of 2,560 readout channels.

3.3.3.2 Forward Preshower Detector

The two Forward Preshower Detectors (FPS) are attached to the faces of the end calorimeters and cover a region of $1.5 < |\eta| < 2.5$ (Figure 14). Each detector consists of an upstream double layer of scintillator strips (minimum ionizing particle layers, or MIP layers), followed by a lead-stainless-steel absorber layer, and another double layer of scintillator strips behind it (shower layers). This configuration allows for the distinction between electron-like and photon-like objects. While an electron-like object will create a minimum ionizing energy deposit in the MIP layers, a photon-like object will not. Therefore electrons can be identified by requiring spatially matched energy deposits in both the MIP layers and the shower layers, whereas photons will only have energy deposits in the shower layers.

3.3.4 Calorimeter

The main purpose of the calorimeter system (23) is to measure the energy deposits from electrons, photons, and jets. It also allows direct identification of electrons, photons, jets, and muons. In addition, measurements of the transverse energy balance in an event, allow to detect the presence of neutrinos.

The calorimeter system consists of a central calorimeter (CC) covering $|\eta| < 1.2$ and two end calorimeters (EC), covering $1.3 < |\eta| < 4.0$ (Figure 21). Each of the calorimeters has an

electromagnetic section, followed by fine and coarse hadronic sections. Since liquid argon is used as the active medium, all calorimeters are contained within cryostats. Different types of materials are used for absorber plates:

- 3 mm (4 mm) plates of depleted uranium for the CC (EC) electromagnetic sections.
- 6 mm plates of uranium-nobium (2%) for the fine hadronic sections.
- 46.5 mm plates of copper (stainless steel) for the CC (EC) coarse hadronic sections.

A typical calorimeter cell is shown in (Figure 22). Each cell consists of a grounded absorber plate and a signal board maintained at a positive high voltage of typically 2 kV. The 2.3 mm gap between the absorber plate and signal board is filled with liquid argon. The calorimeter cells are arranged to form pseudo-projective towers (Figure 23).

In order to measure the energy of electromagnetically interacting objects, the calorimeter takes advantage of the electromagnetic shower process. For example, an incoming electron will emit Bremsstrahlung photons when passing through the dense absorber material and interacting with the nuclei in the absorber via Coulomb interaction. The emitted photons will subsequently decay into electron-positron pairs. This chain of processes continues till the energies of the secondary particles fall below the threshold for pair production. After that the particles mainly interact via ionization. At each stage of the electromagnetic shower, charged particles are ionizing the liquid argon. The high voltage between the absorber plates and signal boards is then used to collect the ionization charges, which allows a measurement of the energy in the shower. Typical transverse sizes of electromagnetic showers are in the range of 1-2 cm.

Hadronic showers are induced by the interaction between hadronic particles and the nuclei

of the absorber material via the strong nuclear force. Secondary hadronic particles then further interact via inelastic nucleus collisions till their energy falls below a threshold. Typical transverse sizes of hadronic showers are of the order of 10 cm.

The space in between the central and end calorimeters ($1.1 < |\eta| < 1.4$) is referred to as the intercryostat region (ICR). In order to be able to measure the energies of particles that pass through this gap in the calorimeter coverage, additional detectors are used. Calorimeter cells called massless gaps (MG) are installed before the first layer of uranium inside of the central and end cryostats. Additionally, a ring of scintillator tiles mounted to the exterior surface of the end cryostats comprises the intercryostat detector (ICD).

Figure 24 shows the different calorimeter detection layers for a given η value (24).

3.3.5 Muon System

Due to their large mass and long lifetime, muons pass through the calorimeter by depositing only a small amount of energy (≈ 2.5 GeV) via ionization. Therefore, the outermost subdetector is dedicated to the detection of muons (Figure 25). The muon system is separated into central and forward detectors. A 1.9 T iron toroid magnet is used for muon momentum measurements.

Proportional Drift Tubes (PDT), Mini Drift Tubes (MDT), and scintillators are the main detection elements used in the muon system. Drift tubes collect the ionization charges created by muons passing through a gas mixture onto high voltage wires. Correlating the arrival times of ionization charges from different drift tubes with the beam crossing time, allows to extrapolate the path of muons as they pass through the detector. Scintillators are mainly used for their

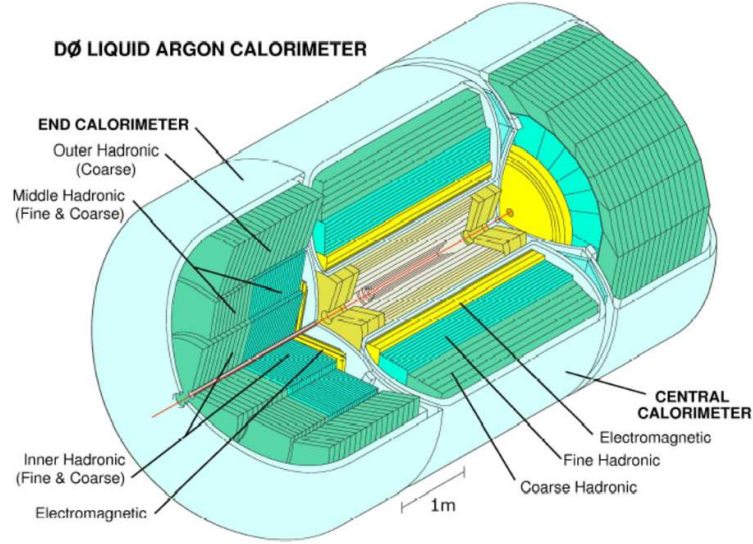


Figure 21. Isometric view of the central and two end calorimeters.

good timing resolution (≈ 4 ns) which allows a way to trigger on muons.

The central muon system (25) covers the region of $|\eta| < 1.0$ and is referred to as the Wide Angle Muon System (WAMUS). It consists of three PDT layers, with the first layer (A layer) in between the toroid magnet and the calorimeter, and two more layers (B and C layers) after the toroid magnet. Additional layers of scintillators before the A layer and covering the outside of the muon system allow for spatial and precise timing measurements to reject cosmic rays.

The forward muon system (26) covers the region of $1.0 < |\eta| < 2.0$ and is referred to as the Forward Angle Muon System (FAMUS). It consists of three MDT layers and scintillators, with

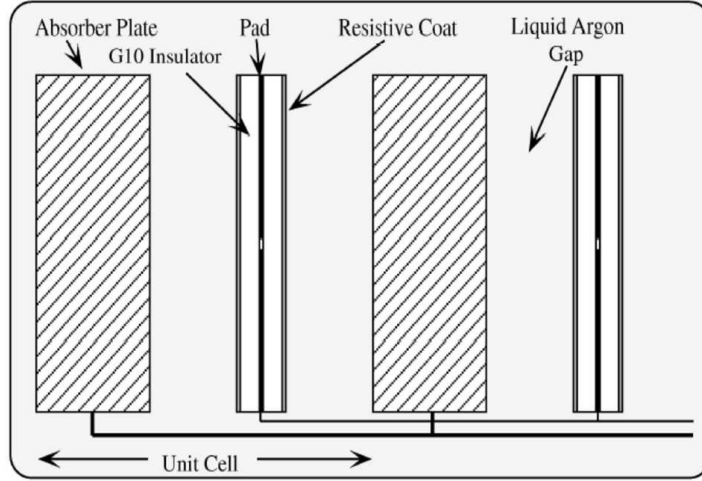


Figure 22. Schematic view of two calorimeter cells.

the first layer (A layer) before the toroid magnet, and two more layers (B and C layers) after the toroid magnet.

3.4 The DØ Trigger and Data Acquisition Systems

DØ deploys a three level trigger system (27; 28) to handle the high proton-antiproton collision rate of 2.5 MHz. Each succeeding level of triggering examines fewer events, with more sophisticated trigger algorithms. At the first stage the Level 1 (L1) system uses a hardware trigger to reduce the event rate to ≈ 5 kHz. At the next stage the Level 2 (L2) system further reduces the event rate to ≈ 1 kHz. L2 uses hardware engines associated with specific detector subsystems and a single global processor for the final L2 trigger decision. In the last step the Level 3 (L3) system which consists of a farm of microprocessors, reduces the event rate

Figure 23. Schematic view showing the calorimeter segmentation pattern. The shading pattern indicates cells for signal readout. The radial lines show the detector pseudo-rapidity intervals.

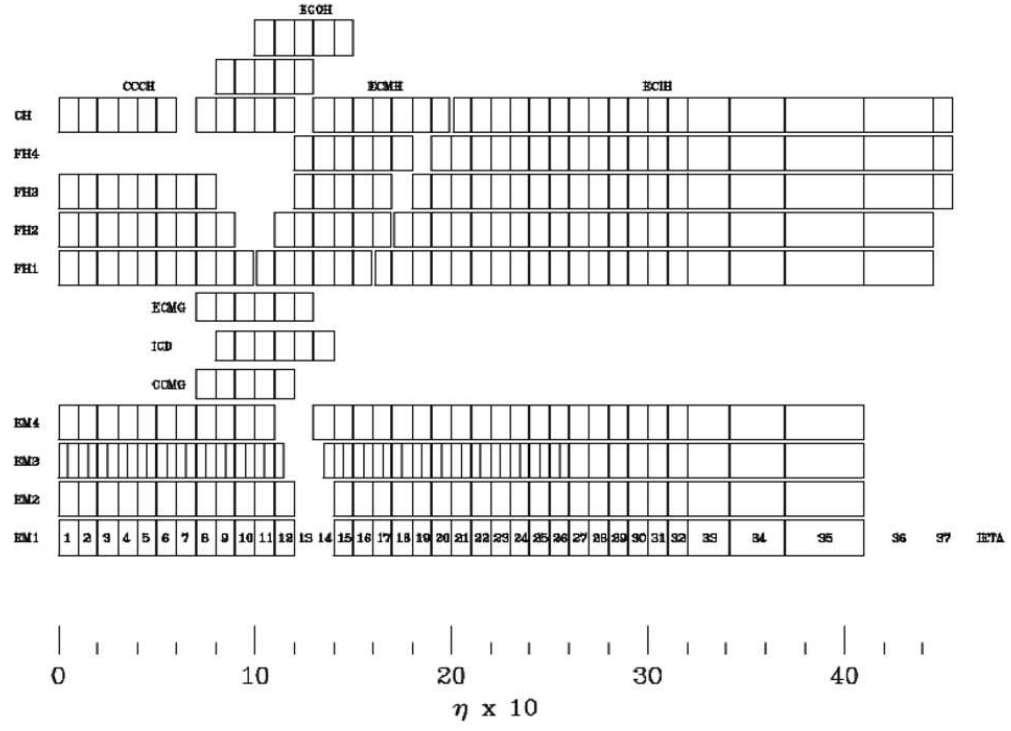


Figure 24. Schematic view of different calorimeter detection layers vs η .

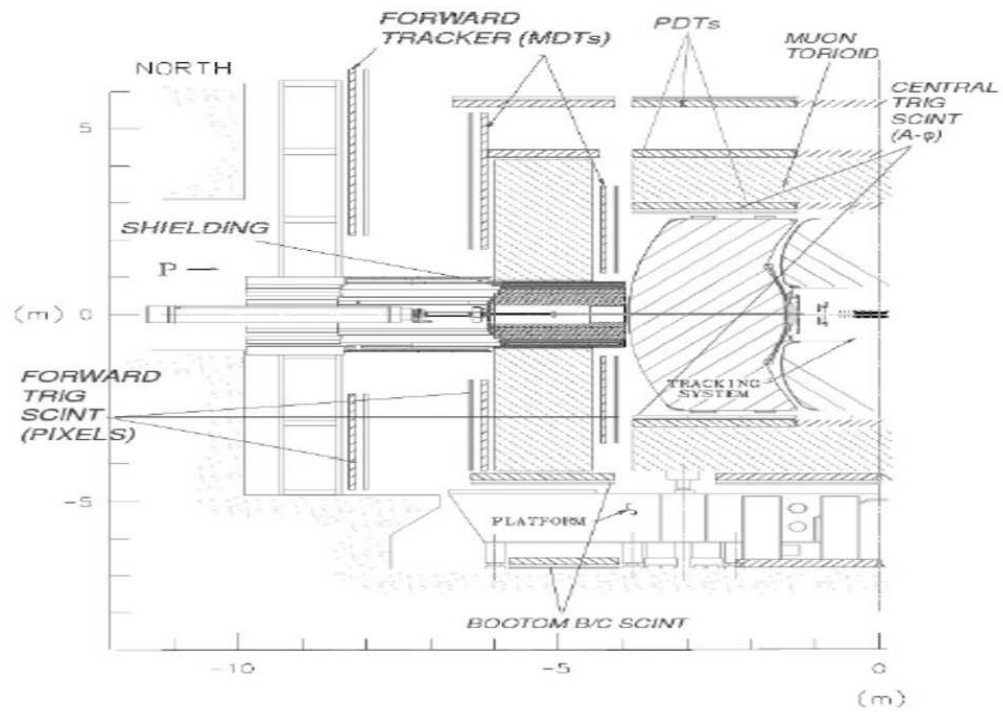


Figure 25. The DØ muon system with scintillators (SCINT) and drift tubes (PDT and MDT).

to ≈ 50 Hz. Only those events that pass all three trigger levels are stored for further offline reconstruction and analysis.

3.4.1 The Level 1 Trigger

The L1 trigger system uses information from the CFT, CPS, FPS, calorimeter and muon subdetectors to provide an event rate reduction by a factor of ≈ 500 . Field programmable gate arrays (FPGAs) check whether a given event satisfies one of up to 128 L1 trigger conditions. If at least one trigger condition is satisfied the event information is digitized and buffered to await a L2 decision. L1 trigger decisions are made within a $4.2 \mu\text{s}$ time window.

3.4.1.1 The Level 1 Calorimeter Trigger

For trigger purposes the calorimeter is segmented into 1280 trigger towers of $\Delta\eta \times \Delta\Phi = 0.2 \times 0.2$. Level 1 calorimeter (L1CAL) trigger decisions are based on the amount of transverse energy deposited in the electromagnetic layers (EM) and electromagnetic plus fine hadronic layers (TOT) of the trigger towers. L1CAL trigger conditions require that a specific number of EM or TOT trigger towers be above a certain transverse energy threshold. In addition L1CAL can also impose thresholds on the total sum of transverse energy and the missing transverse energy in a given event.

3.4.1.2 The Level 1 Central Track Trigger

The Level 1 Central Track Trigger (L1CTT) uses information from the CFT and CPS subdetectors in the central region ($|\eta| < 1.7$), and information from the CFT and FPS subdetectors in the forward region ($1.4 < |\eta| < 2.5$). Possible track candidates are identified by FPGAs using hit patterns in the axial layers of the CFT and matching energy deposits in the preshower

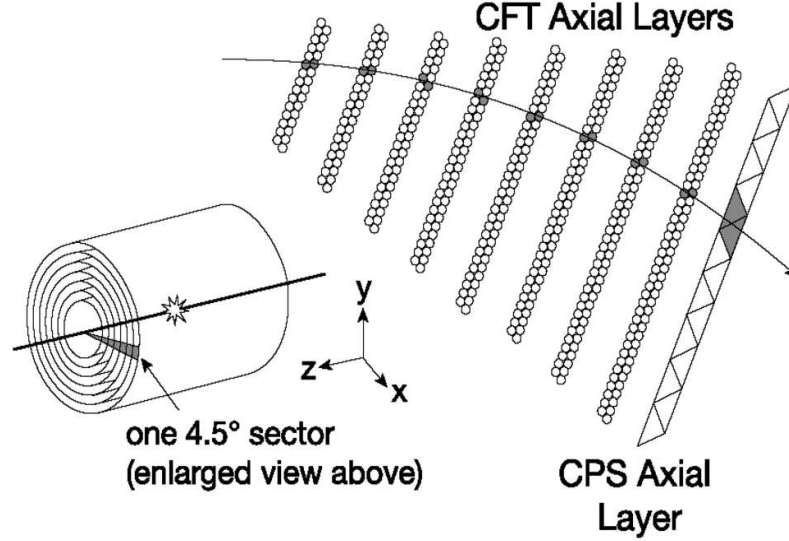


Figure 26. A hypothetical L1CTT track with hits in eight CFT axial doublet layers and the CPS axial layer.

detectors (Figure 26). The p_T of a track candidate can be estimated by the azimuthal bend of the CFT hits. L1CTT trigger conditions require that a track candidate be above a certain p_T threshold with the possibility of a matching hit in the corresponding preshower subdetector.

3.4.1.3 The Level 1 Muon Trigger

The Level 1 Muon Trigger (L1Muon) uses information from the muon wire chambers, muon scintillators, and L1CTT tracks. L1Muon trigger logic is implemented in FPGAs and trigger

conditions require a combination of criteria based on p_T thresholds, geographical region, track quality and multiplicity.

3.4.2 The Level 2 Trigger

The L2 trigger system was designed to reduce the event rate by a factor of 10. It receives inputs from both the L1 system and the detector subsystems. L2 operates in two stages. In the first stage, subdetector-specific preprocessors form physics objects such as EM energy clusters or tracks. Individual preprocessors for the tracking, preshower, calorimeter and muon subdetectors run in parallel and are located in separate crates. L2 preprocessor physics objects are then used at the second stage by a global processor. The L2 global processor makes the final L2 trigger decision by imposing selection criteria on the preprocessor physics object, including correlations between multiple detector subsystems.

The two-stage L2 architecture (*stochastic pipeline*) allows to make trigger decisions within a 100 μs time window (see Appendix B for a detailed description of the L2 trigger system). Events passing L2 trigger requirements are flagged for full detector readout and further refined analysis at the L3 triggering stage.

3.4.2.1 The Level 2 Calorimeter Preprocessor

The Level 2 calorimeter preprocessor (L2Cal) receives the full list of 2560 EM and TOT trigger towers from L1CAL.

The L2 jet algorithm forms jet objects by clustering 5×5 groups of TOT trigger towers centered around seed towers. A jet seed tower is any TOT trigger tower with $E_T \geq 2 \text{ GeV}$. The list of seed towers for the L2 jet algorithm is E_T -ordered. Depending on the configuration,

overlapping L2 jet candidates can be reported as separate jets or simply the highest- E_T jet. An E_T -ordered list of all L2 jets is sent to the L2 global processor.

The L2 Electron/photon algorithm forms EM objects by adding the transverse energies of EM seed towers with their largest E_T neighbors. An EM seed tower is any EM trigger tower with $E_T \geq 1$ GeV. The list of seed towers for the L2 EM algorithm is E_T -ordered. The L2 EM algorithm can be configured in such a way that only the seeds (without considering the neighboring towers) are used to form EM objects. To reduce background the EM energy fractions for both the leading and next-to-leading EM cluster that form the EM object are calculated. Additionally, the isolation of the EM cluster from other energy deposits in the calorimeter is evaluated. An E_T -ordered list of all L2 EM objects and parameters is sent to the L2 global processor.

3.4.2.2 The Level 2 Muon Preprocessors

The Level 2 Muon system (L2Muon) consists of two components: a preprocessor for the central muon region (L2 Muon Central, or L2MUC) and a preprocessor for the forward muon region (L2 Muon Forward, or L2MUF). L2Muon receives inputs from Level 1 (L1Muon), and the muon subdetector drift chambers and scintillators. This allows to improve muon triggering capabilities by incorporating better calibration and timing information from the muon scintillators. Muon tracks at L2 contain η and ϕ information, as well as p_T , sign, and timing information.

3.4.2.3 The Level 2 Preshower Preprocessor

The Level 2 preshower preprocessor (L2PS) receives inputs from the L1 trigger system. Based on preshower detector information it forms clusters with η and ϕ coordinates that can then be matched with calorimeter trigger towers or CFT trigger tracks at the L2 global processing stage.

3.4.2.4 The Level 2 Tracking Preprocessor

The Level 2 tracking preprocessor uses information from L1CTT and the SMT to form lists of L2 track candidates that can be used by the L2 global processor for triggering. This part of the L2 trigger system is still under development. It would allow to trigger on vertices that are displaced from the primary interaction vertex. Displaced vertices are characteristic of long-lived particles such as B -Mesons, and can therefore be used to identify heavy-flavored quarks.

The L2 tracking preprocessor can be operated in two different modes. In the first mode of operation (L2 Central Track Trigger, or L2CTT) it further refines tracking information coming from L1CTT. In the second mode of operation (L2 Silicon Track Trigger, or L2STT) it combines L1CTT and SMT information. Figure 27 shows the conceptual design of L2STT. It uses hit information from the first and last layer of the CFT to define a *road*, and then extrapolates that road into the SMT to find additional hits in the axial strips of the SMT silicon ladders.

3.4.2.5 The Level 2 Global Processor

The Level 2 global processor (L2GBL) receives lists of trigger objects that are generated by the L2 preprocessors (L2Cal, L2MUC, L2MUF, L2PS, L2CTT, L2STT). It creates global trigger

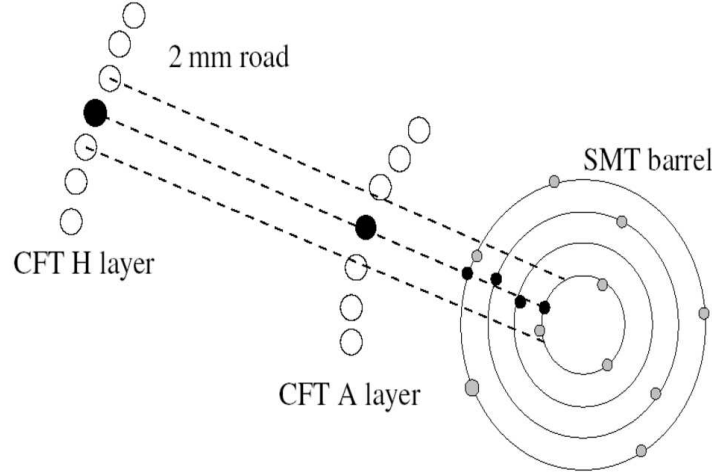


Figure 27. The definition of roads based on L1 tracks and SMT hit selection in L2STT.

objects by either using the trigger objects generated by the preprocessors or by combining trigger object information from different preprocessors. For example, spacial correlations between track candidates and EM energy deposits in the calorimeter can be used to select electron candidates. L2GBL makes the final L2 trigger decision by imposing cuts on global trigger objects that are defined by trigger list information which is parsed from the trigger control computer.

3.4.3 The Level 3 Trigger and Data Acquisition

Both the L1 and L2 trigger systems do not use the full detector readout for their trigger decisions. The event rate needs to be reduced to 1 kHz or below, so that the Level 3 (L3) trigger system can take advantage of the full detector readout. L3 then further reduces the event rate to 50 Hz. The average event size is ≈ 300 kByte.

The L3 trigger system is based on software algorithms that resemble the algorithms for offline event reconstruction (see Chapter 4) as closely as possible, given restrictions due to available processing power.

The data acquisition system (L3DAQ) is based on a single Cisco 6509 Ethernet switch that allows data transfer rates of 250 Mbyte/s. Figure 28 illustrates the main hardware components of the data acquisition system. Detector data is transferred from commodity VME single-board computers (SBCs), via the Ethernet switch to the individual L3 farm nodes. A supervisor process running on a separate CPU provides the interface between the main DØ run control system (COOR) and L3DAQ.

After passing L3 trigger requirements the data are transferred to a permanent storage facility.

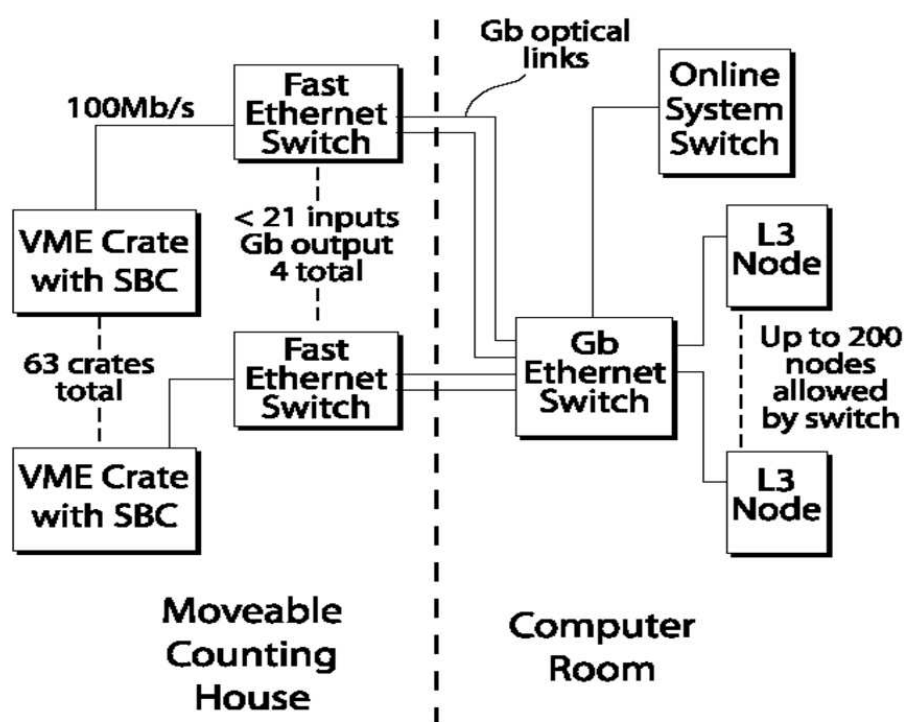


Figure 28. Main L3DAQ hardware components.

CHAPTER 4

OFFLINE EVENT RECONSTRUCTION

This chapter describes how physical objects like electrons or jets, are formed or *reconstructed* from the raw detector data. A collection of complex software algorithms written in C++ called *d0reco* (29) is used for this reconstruction process. As described in the previous chapter a stream of digital readout signals from the subdetectors is being recorded for each event that passes all three levels of triggering. Powerful PC computing farms are deployed to analyze the data and reconstruct candidates of physical objects (electrons, jets, tracks, etc) that can then be used in the final analysis.

4.1 Track Reconstruction

In order to reconstruct track candidates, two different types of algorithms are used. The *Alternative Algorithm* (AA) (30) uses a road-following method, while the *Histogramming Track Finder* (HTF) (31) relies on a histogramming method.

The AA method starts from any combination of three hits in SMT barrels or disks. Moving outwards, towards the CFT, it then extrapolates the sequence of hits to the next SMT or CFT layer. If a hit is found within a configurable expectation window a χ^2 test is performed. If the χ^2 value is below a configurable threshold, the newly found hit is associated with the track candidate. If no hit is found, it is recorded as a *miss*. Construction of track candidates ends until the last layer of the CFT is reached, or until three misses are recorded.

The HTF method takes advantage of the fact that the trajectory of a charged particle moving perpendicular to a homogeneous magnetic field can be characterized by the three parameters ρ , d_0 , Φ ; where $\rho = qB/p_T$ is the radius of curvature, d_0 is the distance of closest approach with respect to (0,0) (*impact parameter*), and Φ is the direction of the track at the point of closest approach to (0,0). Examining only track candidates with small impact parameters, every pair of hits in (x,y) coordinate space belonging to the same track, corresponds to a single point in parameter space (ρ, Φ) . Therefore, after examining every pair of hits and filling a 2-D (ρ, Φ) histogram, a peak in the histogram corresponds to a track candidate.

Both algorithms generate lists of track candidates that are combined after removing duplicates, and applying additional selection criteria based on number of hits, number of misses, and χ^2 value. Figure 29 shows an example of hits and reconstructed tracks (32).

4.2 Primary Vertex Reconstruction

The primary vertex (PV) is the location of the proton-antiproton hard scatter collision. It is important to identify the position of the PV with high accuracy, since it is an essential ingredient to reconstruct jets, electrons and missing transverse energy. It is also important to select an algorithm (33) that allows to distinguish between the hard scatter vertex and vertices from additional *minimum bias* (MB) interactions.

Based on the list of reconstructed tracks (see Chapter 4.1) a list of vertices is generated by extrapolating the tracks back to the z -axis. Clusters of vertices are then formed by selecting vertices within 2 cm of each other along the z -axis. In each vertex cluster, the vertex with the highest number of tracks pointing at it, is stored in a list of “selected” vertices. For every se-

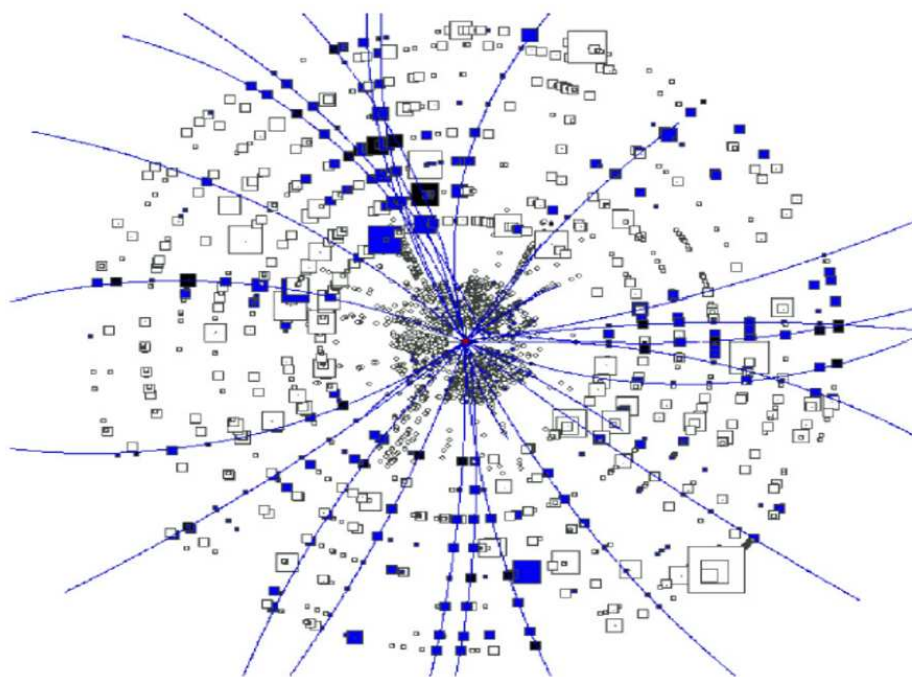


Figure 29. Axial view (looking down the beam-pipe) of a recorded event showing hits and reconstructed tracks. CFT hits are represented by squares, and SMT hits are represented by circles. Hits are colored solid if they are associated with a reconstructed track (solid lines). The curvature of the reconstructed tracks is due to the solenoidal magnetic field, which is pointing out of the page.

lected vertex, tracks nearby are used to compute the probability that the vertex does not come from a MB interaction. The computation of this probability is based on the assumption that tracks coming from MB interactions will have a smaller transverse momentum, as tracks coming from the hard scatter. Finally, the vertex with the smallest MB probability is chosen as the PV.

4.3 Electromagnetic Object Reconstruction and Identification

Electromagnetic objects (EM objects), such as electrons and photons, are initially identified based on calorimeter information. Since photons are not generating any signals in the tracking system, requiring a track that matches the energy deposit in the calorimeter allows to distinguish electrons from photons.

EM object reconstruction starts by forming initial calorimeter clusters. Different algorithms can be used to find those initial clusters:

- Simple-Cone tower clustering algorithm (“Scone Method”)
- Cell Nearest Neighbor clustering algorithm (“CellNN Method”)
- Track extrapolation clustering algorithm (“Road Method”)

In this analysis, objects reconstructed with the simple cone algorithm are used.

4.3.1 Simple-Cone Clustering Algorithm

The simple-cone algorithm (34) clusters calorimeter cells of size $\Delta\eta \times \Delta\Phi = 0.1 \times 0.1$. Each cell is required to have at least 1.5 GeV of transverse energy. Additionally, for each cell the

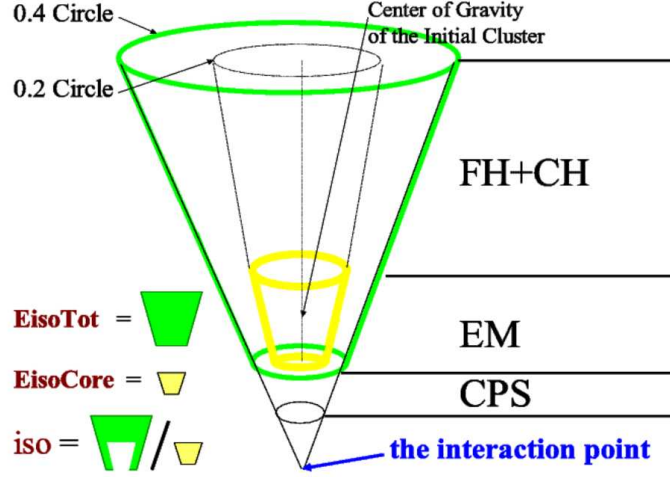


Figure 30. Illustration of the Isolation Parameter: $EisoTot$ is the total energy in a cone of radius 0.4, and $EisoCore$ is the energy in the EM layers in a cone of radius 0.2.

ratio of the energy in the EM layers to the total energy (EM fraction) is required to be above 0.9. Next, all clusters satisfying the above criteria are tested for *isolation*:

$$isolation = \frac{EisoTot - EisoCore}{EisoCore} \quad (4.1)$$

Figure 30 illustrates the definition of the isolation parameter (34). All initial EM clusters are required to have an isolation of less than 0.2. The isolation parameter gives a measure of how deep and narrow a given cluster is. EM objects tend to deposit most of their energy in a narrow region of the EM layers, while hadrons deposit their energies in the hadronic layers in a much wider radius.

4.3.2 Electromagnetic Object Identification Parameters

A set of various parameters is calculated for every EM cluster that passes the initial quality criteria. This allows flexibility when defining EM objects at the analysis stage.

ID: All EM clusters that pass the initial quality criteria are assigned an ID of 10. If in addition a cluster has a track loosely matched to it, it is assigned an ID of ± 11 (“+” for electrons, “−” for positrons).

Isolation: See Chapter 4.3.1.

Electromagnetic Fraction: The electromagnetic fraction (EM fraction) is another discriminant between EM and hadronic calorimeter energy deposits. It takes advantage of the fact that EM showers are almost entirely contained within the EM layers of the calorimeters. Figure 31 illustrates the definition of the EM fraction parameter (34).

H-Matrix: The H-Matrix technique allows a distinction between EM and hadronic energy deposits, by analyzing the longitudinal and transverse shape of the showers. Based on MC generated electrons a covariance matrix (M) is defined using a set of seven discriminant variables :

$$M_{ij} = \frac{1}{N} \sum_{n=1}^N (x_i^n - \langle x_i \rangle) (x_j^n - \langle x_j \rangle) \quad (4.2)$$

where x_i^n is the value of variable i for electron n , and $\langle x_i \rangle$ is the mean value of variable i . The seven variables that are used are listed below:

- Shower energy fraction in 1st, 2nd, 3rd, and 4th EM layer of the calorimeter.
- Cluster size in $r - \Phi$ based on the 3rd EM layer of the calorimeter.

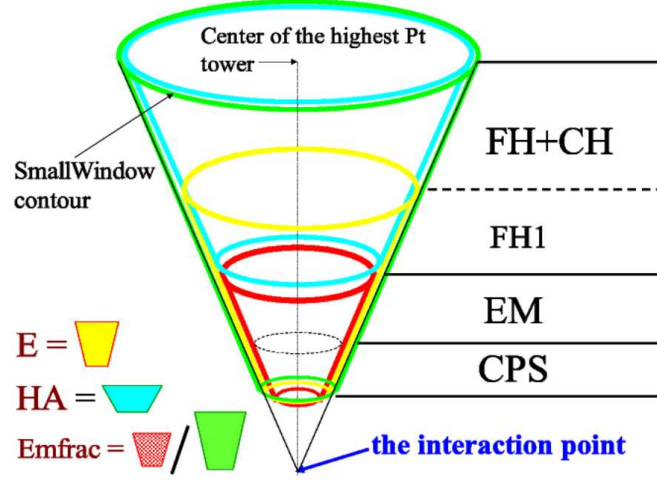


Figure 31. Illustration of the EM fraction parameter: EM fraction is the ratio between the energy in the CPS plus EM layers, and the energy in the CPS plus EM layers plus hadronic layers.

- Total shower energy.
- Primary vertex position.

The H matrix is defined as the inverse of the covariance matrix (Equation 4.2):

$$H \equiv M^{-1} \quad (4.3)$$

Using the H matrix one can calculate a χ^2 -like variable that gives a measure of the likelihood that a given shower k is consistent with an EM object shower:

$$\chi^2 = \sum_{ij} (x_i^k - \langle x_i \rangle) H_{ij} (x_j^k - \langle x_j \rangle) \quad (4.4)$$

Track Matching: Requiring that a track is associated with a calorimeter EM cluster allows to distinguish electrons from photons. In this analysis *global tracks* are used for tracking confirmation, i.e. tracks based on information from both the CFT and SMT subdetectors. Using calorimeter and tracking information the following χ^2 variable is calculated:

$$\chi^2 = \left(\frac{\Delta\Phi}{\sigma_\Phi} \right)^2 + \left(\frac{\Delta z}{\sigma_z} \right)^2 + \left(\frac{E_T/p_T - 1}{\sigma_{E/p}} \right)^2 \quad (4.5)$$

where in Equation 4.5:

- $\Delta\Phi$ (Δz) is the difference in Φ (z) between the EM cluster position in the 3rd EM calorimeter layer and the extrapolation of the track to the same layer.
- σ_Φ , σ_z , and $\sigma_{E/p}$ are the root-mean-squares of the experimental measurements of each quantity.
- E_T/p_T is the ratio of the transverse energy of the EM calorimeter cluster and the transverse momentum of the track.

A track is matched to an EM cluster by requiring that the track matching χ^2 probability is $P(\chi^2) > 10^{-2}$.

4.4 Jet Reconstruction and Identification

Individual quarks and gluons cannot be detected directly due to color confinement. Instead, collimated streams of hadrons (*jets*) are observed in the detector. In this chapter we discuss the techniques that are used to reconstruct and identify jets.

4.4.1 Jet Cone Algorithm

The general idea behind a jet cone algorithm is to define cones in $\eta \times \Phi$ space that contain the energy of a jet that is associated with a certain parton which emerged from the interaction region. The following describes the jet cone algorithm that was used to reconstruct the jets that were used in this analysis (35):

1. Jet reconstruction is based on the total transverse energy (E_T) of calorimeter towers ($\Delta\eta \times \Delta\Phi = 0.1 \times 0.1$). Only towers with $E_T > 0.5$ GeV are considered.
2. Starting with the highest E_T tower as a seed, *preclusters* are formed by adding the transverse energies of all towers within a radius of $\Delta R = \sqrt{(\Delta\eta)^2 + (\Delta\Phi)^2} = 0.3$ around the seed towers. Only preclusters with $E_T > 1.0$ GeV are considered. Towers cannot be shared amongst different preclusters.
3. For every precluster the E_T (Equation 4.6) and E_T weighted cone centroid (Equation 4.7, Equation 4.8) are calculated:

$$E_T \equiv \sum_i E_T^i = \sum_i E_i \times \sin \theta_i \quad (4.6)$$

$$\eta = \frac{\sum_i E_T^i \eta_i}{\sum_i E_T^i} \quad (4.7)$$

$$\Phi = \frac{\sum_i E_T^i \Phi_i}{\sum_i E_T^i} \quad (4.8)$$

4. The E_T in a cone of radius $\Delta R = 0.5$ around each precluster is calculated, as well as the cone axis. This step is repeated until the cone axis becomes stable. Each stable cone is added to a list of *proto-jets*. Only proto-jets with $E_T > 8.0$ GeV are considered.
5. Using a similar clustering procedure as before, midpoints between any combination of two proto-jets are also used as seeds and iterated until stable cones are found. This step is done to remove sensitivity to soft radiation.
6. After receiving a list of proto-jets coming from preclusters and midpoints, the proto-jets are checked for overlapping regions. In order to avoid double counting of energy a merging/splitting algorithm is applied. Two proto-jets are *merged* if the shared energy between them is greater than half of the lower E_T proto-jet. Otherwise, the two proto-jets are *split* and the tower energies are assigned to the closest proto-jet.

4.4.2 Jet Identification Parameters

A set of quality cuts is applied to every reconstructed jet, in order to reduce fake jets from calorimeter noise.

EM Fraction (EMF): Hadronic shower formation tends to distribute energy evenly in the EM and hadronic layers of the calorimeter, whereas EM objects mostly shower in the EM layers. Therefore, a cut on the fraction of transverse energy in the EM layers allows to distinguish jets from EM objects.

Coarse Hadronic Fraction (CHF): Coarse hadronic fraction is the fraction of transverse energy of a jet that is deposited in the coarse hadronic layers of the calorimeter.

Hot Fraction (HotF): Hot Fraction is the ratio of transverse energy in the most energetic tower to that of the next most energetic tower in the jet. If a significant amount of the total jet energy is originating from a single calorimeter tower, it is likely that the tower is generating artificially high read-out signals due to detector problems (*hot tower*). A cut on the Hot Fraction parameter allows to eliminate jets originating from hot towers.

N90: N90 is the number of towers making up 90% of the jet energy. A cut on the N90 parameter allows to eliminate jets originating from hot towers as well.

L1 Confirmation: L1 confirmation was introduced in order to deal with calorimeter cell precision readout noise. The parameter compares the jet energy at the L1 trigger tower level with the jet energy derived from the jet cone algorithm, which is based on calorimeter cell precision readout:

$$L1conf = \frac{\sum_{trigger} E_T^i}{E_T^{jet} \cdot (1 - CHF)} \quad (4.9)$$

where $\sum_{trigger} E_T^i$ is the sum of transverse TOT trigger tower energies within $\Delta R < 0.5$ of the reconstructed jet; E_T^{jet} is the transverse energy of the reconstructed jet; and CHF is the Coarse Hadronic Fraction of the reconstructed jet.

4.4.3 Jet Energy Scale

The jet energy scale (JES) is a calibration that adjusts the measured jet energy for various effects (36). Depending on the jet E_T and jet η it applies a calibration factor that allows to

obtain the particle level jet E_T ($E_{jet}^{particle}$) from the measured jet E_T ($E_{jet}^{calorimeter}$) according to the following relation:

$$E_{jet}^{particle} = \frac{E_{jet}^{calorimeter} - E_{offset}}{R_{jet} \cdot R_{cone}} \quad (4.10)$$

where E_{offset} is the *offset energy*, R_{jet} is the *jet response* correction, and R_{cone} is the *out of cone showering* correction.

Offset Energy: Any energy contributions to the jet reconstruction that are not related to the physics processes that are responsible for creating a jet need to be subtracted from the measured jet energy. The offset energy term contain contributions from multiple interactions, underlying event energy, electronic noise, uranium noise, and pile-up from previous bunch crossings.

Jet Response: The jet response correction takes into account the calorimeter response to the hadronic jets, i.e. the amount of energy that is lost due to uninstrumented regions and dead material in the calorimeter. The correction is estimated from the p_T imbalance in back-to-back photon+jet events. Since photon E_T can be measured to a high level of accuracy, this allows a good estimation of the jet response.

Out of Cone Showering: Due to interactions between the particles that comprise a jet and detector material, it is possible that some particles produced inside (outside) the jet algorithm cone deposit a fraction of their energy outside (inside) of the cone. Additionally, particle trajectories can get bent in the magnetic field, which again can lead to energy being deposited inside or outside of the jet cone.

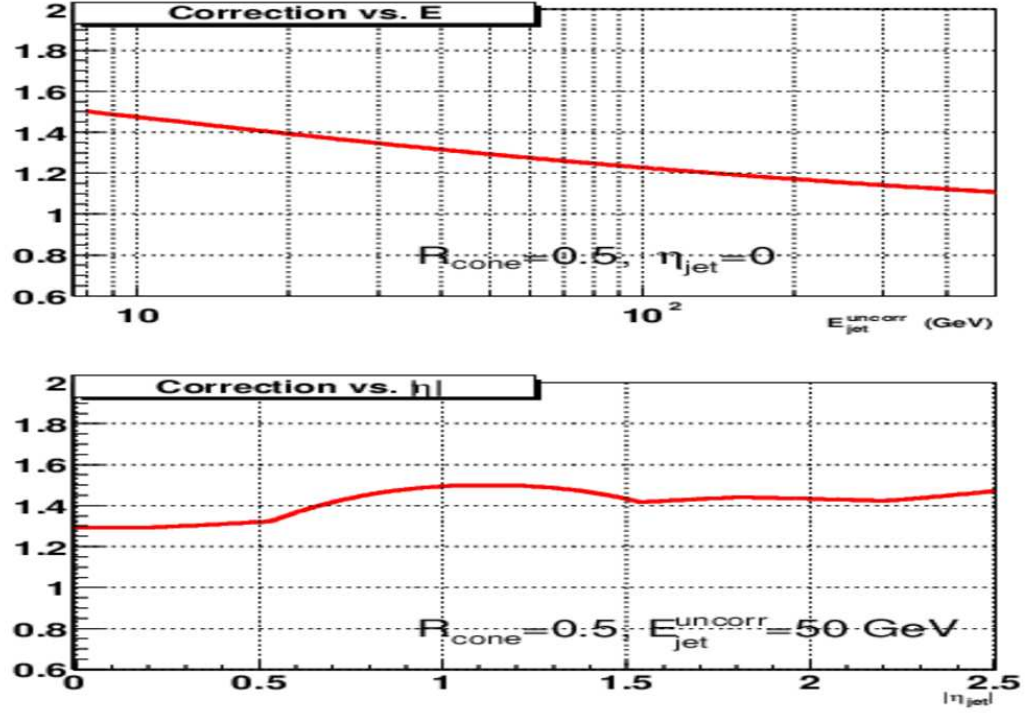


Figure 32. The jet energy scale correction factor measured for jets in data as a function of E (top) and η (bottom).

Figure 32 shows the overall jet energy scale corrections as a function of E and η (37).

CHAPTER 5

MONTE CARLO EVENT SIMULATION

Monte Carlo event simulations are an essential tool in particle physics (38; 39). The simulations represent our theoretical understanding of nature and the ultimate goal is to simulate nature as accurately as possible. In particle physics MC simulations include all stages of interactions that occur at particle accelerators, including initial creation of partons in hadronic collisions (*parton level*), subsequent hadronization (*particle level*), and simulations of detector responses (*detector level*). Therefore, MC event simulations allow to compare MC output with data, in order to test theoretical predictions. The simulations can also be used to estimate detector acceptances, and for the study of background processes. Alternatively, the simulations allow to correct data for detector effects so that direct comparisons to generator level MC simulations can be made.

This chapter gives a brief description of the MC simulation tools and techniques, that were used in this analysis.

5.1 The PYTHIA Event Generator

PYTHIA is a general purpose MC event generator (40). It is able to describe most physical aspects of a typical high-energy event:

1. The initial beam particles, such as protons and antiprotons, are characterized by PDFs.

2. One parton from each initial particle starts to radiate in a *Bremsstrahlung*-like process, such as $q \rightarrow qg$, to initiate a sequence of branchings, which builds up an initial-state shower (*Initial State Radiation*, or ISR).
3. Two partons participate in the *hard process*, which produces a number of outgoing particles. PYTHIA is optimized for hard processes that have two particles in the initial and final states, such as $q\bar{q} \rightarrow Z/\gamma^* \rightarrow e^+e^-$ ($2 \rightarrow 2$ process). Intermediate resonances, like Z/γ^* , need to be included in the description of the hard process.
4. Final state particles can also radiate to initiate a final-state shower (*Final State Radiation*, or FSR).
5. The remaining partons (*spectators*) in the two incoming hadrons may interact.
6. Beam remnant interactions need to be taken into account.
7. Outgoing quarks and gluons are forming color neutral hadrons, due to QCD confinement.
8. Many of the produced hadrons are unstable and decay further.

In order to describe inclusive $Z/\gamma^* \rightarrow e^+e^-$ events, we use a PYTHIA sample based on the $q\bar{q} \rightarrow Z/\gamma^* \rightarrow e^+e^-$ hard process. For this process the LO cross section is purely an electroweak process. ISR parton showers provide QCD corrections to the LO calculation. Figure 33 shows a schematic view of a parton shower (9). The probability for a parton to radiate, or branch, is given by the *DGLAP* or *Altarelli-Parisi* equation. First, we introduce

$$t = \ln(Q^2/\Lambda^2) \quad \Rightarrow \quad dt = d \ln(Q^2) = \frac{dQ^2}{Q^2} \quad (5.1)$$

where Q is the scale of the hard process, and Λ is the scale at which α_s becomes large and non-perturbative QCD becomes important. The differential probability for parton a to branch is now

$$d\mathcal{P}_a = \sum_{b,c} \frac{\alpha_s}{2\pi} P_{a \rightarrow bc}(z) dt dz. \quad (5.2)$$

where a branches according to $a \rightarrow bc$, with parton b taking a fraction z of the energy and momentum of a . The splitting kernels $P_{a \rightarrow bc}(z)$ express the branching probabilities for different branchings, and the sum runs over all allowed branchings ($q \rightarrow qg$, $g \rightarrow q\bar{q}$, etc.). The parameter t can be regarded as describing the time for the shower evolution. In this picture, the actual probability that a branching of a occurs at t can be expressed as the naive answer modified by an exponential suppression: if a parton has already branched at a ‘time’ $t' < t$, it can no longer branch at t . This description is analogous to the radioactive decay problem. In the parton-shower language, the exponential factor is known as the *Sudakov form factor*. PYTHIA uses this ‘radioactive decay’ type description and applies it to the parton-shower evolution.

The parton shower is evolved from the scale Q down to a cut-off scale Q_0 , where it terminates. At this scale QCD becomes strongly interacting and perturbation theory breaks down. Due to confinement, the colored partons are converted into colorless hadrons by the hadronization process. PYTHIA uses a phenomenological model known as the *String Model* to describe this process. As a color-confined quark-antiquark pair moves out in opposite directions, the color field between them collapses into a string-like configuration. Since the string has a uniform energy per unit length, the potential energy in the string increases as the quarks move apart. Once it becomes energetically favorable another $q\bar{q}$ pair is pulled from the vacuum, splitting

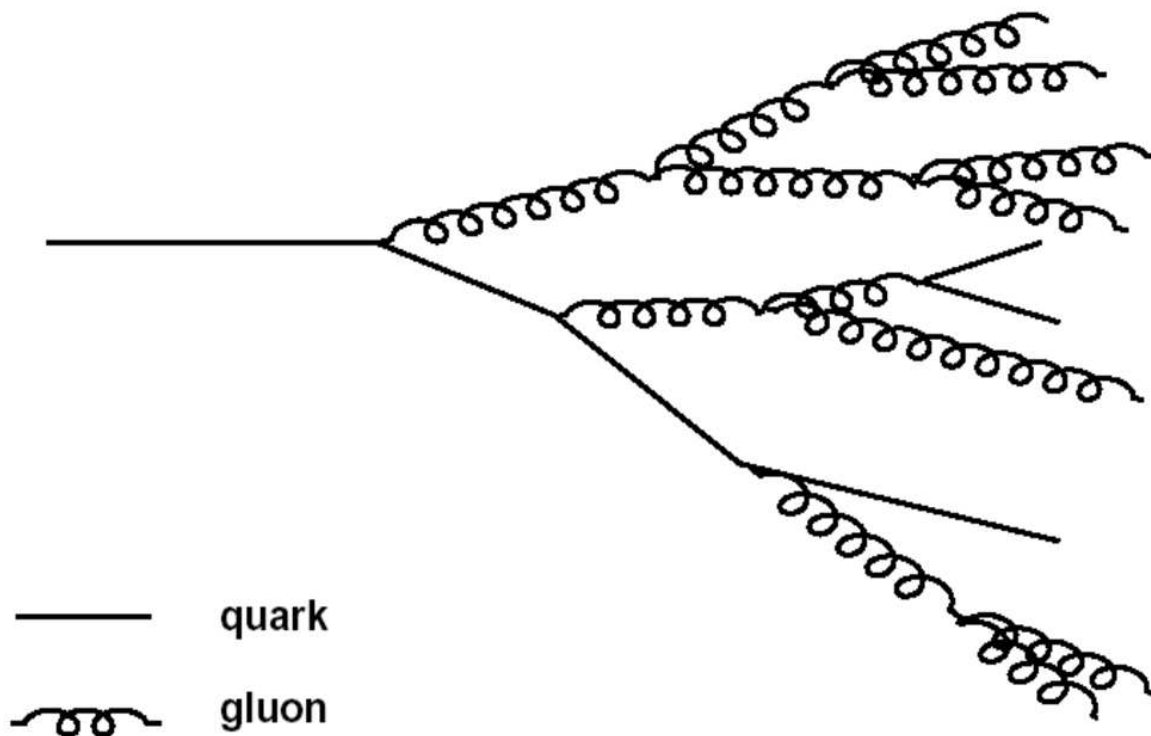


Figure 33. Schematic view of a parton shower.

the string in two. This process continues until only on mass-shell hadrons remain.

5.2 Combining Matrix Elements with Showering

PYTHIA is essentially based on the differential cross section for a simple $2 \rightarrow 2$ process, combined with a parton-shower simulation of additional QCD radiation that connects to a model

of hadronization in order to account for multijet events. Since parton showers are only reliable approximations in the soft and collinear limits, they do not properly describe final states with several hard and well separated jets. Such final states occur frequently at the Tevatron due to the large energies that are available. Therefore, different MC generators are needed that allow to estimate multijet cross sections by calculating the corresponding partonic matrix elements. In order to obtain results that can be compared to experimental data, these calculations need to be completed by taking into account higher-order corrections leading to the development of partonic cascades, and with the subsequent transformation of the partons into observable hadrons. The consistent combination of the parton level calculations with the partonic evolution due to the MC shower simulation, as implemented in PYTHIA, is the subject of extensive work (41; 42).

One of the biggest problems when combining matrix element and parton shower event generators is due to the potential *double counting* of jet configurations. Consider a process like $q\bar{q} \rightarrow Z$ together with its higher order companion process $q\bar{q} \rightarrow Zg$. Only a fraction of the higher order process is described by the lower order process through gluon ISR. Therefore, the two processes should not be blindly combined, in order to avoid double counting of some portion of phase space. In addition, simply ignoring the higher order process would lead to a poor description of high p_T Z bosons.

A solution to this problem has been proposed by Catani, Krauss, Kuhn, and Webber (*CKKW*) (43). In this approach the phase space for a n parton process is divided into a matrix element regime and a parton shower regime, by using the parameter y_{cut} . Kinematics in

the parton shower regime are based on $n - 1$ partons. While the parton shower develops, possible branchings can be *vetoed* by re-weighting the matrix elements with Sudakov form factors. This essentially prevents the shower regime from populating the matrix element regime. Since y_{cut} introduces an arbitrary scale, physical observables will be dependent on y_{cut} . Following the CKKW prescription this dependence is small.

5.2.1 Combining ALPGEN with PYTHIA

In order to describe inclusive $Z/\gamma^* \rightarrow e^+e^- + \geq n$ jet events ($n \geq 1$) we use the tree-level matrix element generator ALPGEN (44; 45). ALPGEN was designed to simulate specific SM processes in hadronic collisions, emphasizing large jet multiplicities in the final state. It calculates parton level final states to lowest order in perturbation theory. The ALPGEN output is interfaced with PYTHIA for showering and hadronization.

No procedure to avoid double counting of jet configurations is implemented in the ALPGEN + PYTHIA samples used for this analysis. While it is still possible to use these samples to compare the shape of basic kinematic variables, they can not be used to estimate cross sections.

5.2.2 Combining MADGRAPH with PYTHIA

MADGRAPH (46) is a tree-level matrix element generator that allows to specify initial and final state particles for arbitrary processes. It then creates a list of all relevant Feynman diagrams and calculates the corresponding matrix elements. The program is able to calculate matrix elements for any SM process. The only limitation is processing power¹. The MAD-

¹At present MADGRAPH is limited to 10,000 diagrams per subprocess, corresponding to $W + 5$ jets.

GRAPH output is interfaced with PYTHIA for showering and hadronization.

The matching between MADGRAPH and PYTHIA in order to avoid double counting is done following a modified CKKW prescription (see (47; 48) for details). We refer to these samples as *CKKW samples* and use them for the final cross section comparison.

5.3 The MCFM Monte Carlo Simulation

MCFM (*Monte Carlo for FeMtobarn processes*) (49; 50; 51) is a parton-level event generator with at most three partons in the final state. It allows to calculate partonic cross sections to NLO in α_s . No parton showering or hadronization is available for MCFM at the moment. As an advantage, the dependence of the cross sections on the renormalization and factorization scales is much reduced at NLO.

We compare our final results to MCFM cross sections.

5.4 The DØ Detector Simulation

After all final state particles are generated, detector effects can be simulated with a simulation package called D0GSTAR (*D0 GEANT Simulation of the Total Apparatus Response*) (52). D0GSTAR is based on the CERN package GEANT (*GEometry ANd Tracking*) (53) which simulates the passage of particles through matter. Effects such as ionization, showering, and magnetic field interaction in the DØ detector are modeled. The output of this simulation has the same format as the real data recorded by the detector. The full event reconstruction applied to real data can also be applied to the simulation output for direct comparisons.

CHAPTER 6

MEASUREMENT OF THE $Z/\gamma^*(\rightarrow e^+e^-)+\geq n$ JET PRODUCTION CROSS SECTIONS

This chapter outlines the measurement of the $Z/\gamma^* \rightarrow e^+e^- + \geq n$ jets production cross sections. A description of the data and MC samples is given in Section 6.1. Event selection criteria are discussed in Section 6.2. Section 6.3 compares basic properties of electrons and jets between data and MC. In Sections 6.4 and 6.5 we describe the measurements of the inclusive $Z/\gamma^* \rightarrow e^+e^-$ cross section, and the $Z/\gamma^* \rightarrow e^+e^- + \geq n$ jets cross sections ($n \geq 1$). Sources for systematic errors are evaluated in Section 6.6.

6.1 Data and MC Samples

6.1.1 Data Sample

The dataset used for this analysis was collected between April 2002 and June 2004 and contains approximately 1 billion events. We analyse the raw data with the p14 version of the DØ reconstruction software. In order to reduce the size of the data sample, we apply additional pre-selection or *skimming* criteria:

EM1TRK skimming Requiring that each event in the data set has at least one EM object with $ID = 10$ or ± 11 and $p_T > 8$ GeV, and a track with $p_T > 5$ GeV within $\Delta\phi = 0.1$ of the EM object, reduces the size of the data sample to approximately 57 million events.

Root tuple skimming The reconstructed data are reformatted into an object oriented ntuple format (*root tuple*) using the ATHENA (54) software package (version p16-br-03). At this stage JES corrections (version 5.3) and a calorimeter noise suppression algorithm (T42 (55)) are applied. The root tuple data are then further skimmed by requiring at least one EM object with EM fraction > 0.9 , Isolation < 0.15 , H-Matrix(7) < 12.0 , $|\eta_{det}| < 1.1$ and a track match¹ in each event. The final analysis root tuple contains 2.4 million events.

Data declared as unusable by data-quality experts is excluded from the analysis. We require that the SMT, CFT, calorimeter, and luminosity subsystems of the detector are fully operational. Additionally all data taking periods with limited L1CAL trigger coverage ($|\eta| < 0.8$) are excluded (56).

Events for the analysis are selected based on the requirement that the trigger system identifies at least one EM object (*single electron triggers*). Additionally, the single electron triggers need to be *unprescaled*. In case that the trigger conditions implemented in the trigger system during data taking are not providing the required reduction in event rate, *prescaling factors* are applied. If a prescaling factor of n is applied to a certain trigger, it will only accept every n -th event satisfying the trigger conditions. All single electron triggers used in this analysis have their prescaling factors set to 1.

The data taking period for this analysis can be divided into two periods, during which

¹ χ^2 probability for best track using the distance in η/Φ and E/p

different lists of triggers were implemented. The following is the prioritized order of trigger combinations for trigger lists before *global_CMT-12* (runs ≤ 178732 , “pre-v12 dataset”)¹ (57):

- EM_HI_SH or EM_HI.2EM5_SH
- EM_HI_SH
- EM_HI
- EM_MX_SH
- EM_MX

The Level 2 trigger subsystem was not available for the entire pre-v12 dataset (all runs with run numbers ≤ 169523) in which case we do not require the Level 2 trigger condition to be satisfied.

The trigger combinations for trigger list *global_CMT-12* (runs ≥ 178722 , “v12 dataset”) are:

- E1_SHT20 or E2_SHT20 or E3_SHT20 or E1_SH30
- E1_SHT20 or E2_SHT20 or E1_SH30
- E1_SHT20 or E1_SH30
- E1_SHT20

Table I contains details of the individual triggers.

A total integrated luminosity of 343 pb^{-1} was available for this analysis after trigger selection and exclusion of unusable data due to bad quality.

¹“Trigger A or Trigger B” = if Trigger A and Trigger B are unscaled, accept the event if Trigger A or Trigger B fired

TABLE I

SINGLE EM TRIGGERS USED IN THIS ANALYSIS			
Trigger	L1	L2	L3
EM_HI_SH	CEM(1,10)	EM(1,12)	ELE_LOOSE_SH_T(1,20)
EM_HI_2EM5_SH	CEM(2,5)	EM(1,12)	ELE_LOOSE_SH_T(1,20)
EM_HI	CEM(1,10)	EM(1,12)	ELE_LOOSE(1,30)
EM_MX_SH	CEM(1,15)	none	ELE_LOOSE_SH_T(1,20)
EM_MX	CEM(1,15)	none	ELE_LOOSE(1,30)
E1_SHT20	CEM(1,11)	none	ELE_NLV_SHT(1,20)
E2_SHT20	CEM(2,6)	none	ELE_NLV_SHT(1,20)
E3_SHT20	CEM(1,9)CEM(2,3)	none	ELE_NLV_SHT(1,20)
E1_SH30	CEM(1,11)	none	ELE_NLV_SH(1,30)

L1 Triggers	
CEM(1,10)	one EM trigger tower with $E_T > 10$ GeV
CEM(2,5)	two EM trigger towers with $E_T > 5$ GeV
CEM(1,15)	one EM trigger tower with $E_T > 15$ GeV
CEM(1,11)	one EM trigger tower with $E_T > 11$ GeV
CEM(2,6)	two EM trigger towers with $E_T > 6$ GeV
CEM(1,9)CEM(2,3)	one EM trigger tower with $E_T > 9$ GeV, another EM trigger tower with $E_T > 3$ GeV

L2 Triggers	
EM(1,12)	one EM candidate with $E_T > 12$ GeV (not present for runs below 169524)

L3 Triggers	
ELE_LOOSE_SH_T(1,20)	one electron with $ \eta < 3.0$ and $E_T > 20$ GeV passing loose requirements including shower shape cuts
ELE_LOOSE(1,30)	one electron with $ \eta < 3.0$ and $E_T > 30$ GeV passing loose requirements
ELE_NLV_SHT(1,20)	one electron with $ \eta < 3.6$ and $E_T > 20$ GeV passing tight shower shape cuts
ELE_NLV_SH(1,30)	one electron with $ \eta < 3.6$ and $E_T > 30$ GeV passing loose shower shape cuts

6.1.2 Monte Carlo Samples

6.1.2.1 PYTHIA and ALPGEN Samples

The MC samples used for data to MC comparisons and acceptance estimations are summarized in Table II. For studies regarding the inclusive $Z/\gamma^* \rightarrow e^+e^-$ cross section a PYTHIA $Z/\gamma^* \rightarrow e^+e^-$ inclusive sample is used (CTEQ5 PDF). For higher jet multiplicities, events are generated with ALPGEN and then passed through PYTHIA for parton showering and hadronization ($\mu_{F/R}^2 = M_Z^2 + \sum p_{T,jet}^2$). Since the electron energy resolution in data is not correctly described by the MC simulation, additional energy smearing is applied to the MC electrons. The p_T (as well as p_x , p_y , p_z and Energy) of the electrons is replaced by $p_T \rightarrow p_T \cdot c \cdot \text{Gauss}(1, f)$ where Gauss(1,f) is the smearing parameter which is randomly chosen from a Gaussian distribution with mean 1 and width f . c is an overall calibration factor. We use the following values for the smearing parameters (58):

- $f = 0.045$
- $c = 1.003$

We also apply jet resolution smearing to the MC jets based on the jet resolution in data and MC derived with JES version 5.0 (applying T42)(59). Equation 6.1 shows the resolution

parameterization where the constants C , S , and N represent the calibration errors, sampling fluctuations, and noise contributions respectively.

$$\frac{\sigma(p_T)}{p_T} = \sqrt{\frac{N^2}{p_T^2} + \frac{S^2}{p_T} + C^2} \quad (6.1)$$

Table III summarizes all coefficients for different detector regions.

Using the p_T and η_{det} of the MC jets, we calculate the data and MC resolutions. If for a given jet the data resolution is better than the MC resolution, we do not apply any additional smearing. If the resolution is worse in data than in MC, we calculate a multiplicative smearing factor (Equation 6.2) and apply it to the p_T of the jet.

$$\text{Smearing Factor} = \text{Gauss} \left(1, \sqrt{\left(\frac{\sigma(p_T)}{p_T} \right)_{data}^2 - \left(\frac{\sigma(p_T)}{p_T} \right)_{MC}^2} \right) \quad (6.2)$$

Process	Generators	SAM Dataset definition	Size
$Z(\gamma^*) \rightarrow e^+e^-$	PYTHIA	p14.05.01_pythia_zee_m60-130	400k
$Zj \rightarrow e^+e^-j$	ALPGEN + PYTHIA	p14.05.01_alpgen_pythia_zj_eej	150k
$Zjj \rightarrow e^+e^-jj$	ALPGEN + PYTHIA	pdt-zjj-eejj-p14tmb	180k
$Zjjj \rightarrow e^+e^-jjj$	ALPGEN + PYTHIA	p14.07.00_alpgen_pythia_zjjj_eejjj	15k

TABLE II

LIST OF MC SAMPLES

Coefficient	$ \eta_{det} < 0.5$	$0.5 < \eta_{det} < 1.0$	$1.0 < \eta_{det} < 1.5$	$ \eta_{det} > 1.5$
N_{data}	5.05	$9.06 \cdot 10^{-9}$	2.24	6.42
S_{data}	0.753	1.2	0.924	$4.5 \cdot 10^{-10}$
C_{data}	0.0893	0.087	0.135	0.0974
N_{MC}	4.26	4.61	3.08	4.83
S_{MC}	0.658	0.621	0.816	$5.13 \cdot 10^{-7}$
C_{MC}	0.0436	0.0578	0.0729	0.0735

TABLE III

JET RESOLUTION PARAMETERS IN DATA AND MC.

6.1.2.2 CKKW Samples

Table IV summarizes the CKKW samples that are used. The samples use a matching threshold of $p_T > 15$ GeV. Jets are restricted to $|\eta| < 2.5$. The Z boson has a generated mass between 75 GeV and 105 GeV. The matrix element generation with MADGRAPH was done up to jet multiplicities of 3. Higher jet multiplicities are due to parton showering and hadronization simulated with PYTHIA. The factorization scale is set to $\mu_F^2 = M_Z^2$. The renormalization scale is set to $\mu_R^2 = p_{Tjet}^2$ for jets from initial state radiation and $\mu_R^2 = k_{Tjet}^2$ for jets from final state radiation.

6.1.2.3 MCFM Cross Sections

MCFM inclusive cross sections are calculated for up to 3 jets. The kinematic and geometric jet cuts are the same as used in the analysis: jet $p_T > 20$ GeV, $|\eta| < 2.5$. The Z boson has a mass between 80 GeV and 100 GeV and CTEQ6M is used for the PDF. The renormalization and factorization scales are set to $\mu_{F/R}^2 = M_Z^2 + p_{TZ}^2$.

Process	Generators	SAM Dataset definition	Size
$Zj \rightarrow e^+e^-j$	MADGRAPH + PYTHIA	p14tmbfix_ckkw_batch2_z1jets	234k
$Zjj \rightarrow e^+e^-jj$	MADGRAPH + PYTHIA	p14tmbfix_ckkw_batch2_z2jets	20k
$Zjjj \rightarrow e^+e^-jjj$	MADGRAPH + PYTHIA	p14tmbfix_ckkw_batch2_z3jets	3k

TABLE IV

LIST OF CKKW SAMPLES

6.2 Event Selection

The following selection criteria are applied in order to assure that we select events with two high p_T electrons contained within the central calorimeter and originating from the decay of a Z/γ^* gauge boson. After identifying these Z *candidate* events, we require the presence of n high p_T jets.

6.2.1 Primary Vertex

The primary vertex is required to be within 60 cm of the detector center along the beam pipe (z-axis).

6.2.2 Electron Selection

EM objects have to satisfy the following requirements:

- Loose electrons:
 - ID = 10 or ± 11
 - EM Fraction > 0.9
 - Isolation < 0.15

- H-Matrix(7) < 12
- $p_T > 25$ GeV
- $|\eta_{det}| < 1.1$
- Tight electrons:
 - Requirements of loose electron.
 - Track match¹ with $P(\chi^2) > 0.01$

6.2.3 Z Selection

Z candidates are selected based on the following criteria:

- Two loose electrons.
- At least one of the two electrons needs to be tight.
- At least one of the two electrons needs to have matching trigger objects at L1, L2 and L3 for one of the unscaled single electron triggers that fired in a given event. The trigger objects also need to satisfy the trigger requirements for those triggers.
- Diem invariant mass window cut: $75 \text{ GeV} < M_{ee} < 105 \text{ GeV}$

6.2.4 Jet Selection

Jets are formed using a simple cone jet algorithm with a cone size of 0.5 and are selected based on the following criteria:

¹ χ^2 probability for best track using the distance in η/Φ and E/p

- $0.05 < \text{EMF} < 0.95$
- $\text{HotF} < 10$.
- $\text{N90} > 1$.
- $\text{CHF} < 0.4$
- L1 confirmation
- JES corrected $p_T > 20 \text{ GeV}$
- $|\eta_{\text{physics}}| < 2.5$
- Since the jet algorithm identifies *fake* jets originating from electron energy deposits, we remove all jets overlapping with electrons coming from the Z/γ^* boson within $\Delta R = \sqrt{\Delta\eta^2 + \Delta\phi^2}$ of 0.4

6.2.5 Event Statistics

Table V gives an overview of the event statistics with regard to exclusive jet multiplicities.

6.3 Data vs Monte Carlo

This section presents a comparison of basic kinematic distributions for electrons, Z candidates, and jets between data and MC simulations. It is important that the MC distributions describe the data distributions as accurately as possible. The MC simulations are used to account for the fraction of events that are lost due to kinematic and geometric electron cuts, the diem invariant mass cut, and the primary vertex cut (*acceptance*).

Sample	N	Fraction
$Z/\gamma^* + 0$ jets	12,247	0.8815
$Z/\gamma^* + 1$ jets	1,427	0.1027
$Z/\gamma^* + 2$ jets	189	0.0136
$Z/\gamma^* + 3$ jets	25	0.0018
$Z/\gamma^* + 4$ jets	3	0.0002
$Z/\gamma^* + 5$ jets	2	0.0001
Total	13,893	1.0000

TABLE V

EVENT BREAKDOWN BY EXCLUSIVE JET MULTIPLICITIES ASSOCIATED WITH Z/γ^* PRODUCTION BEFORE ANY BACKGROUND IS SUBTRACTED OR ANY CORRECTIONS ARE APPLIED.

6.3.1 Primary Vertex Comparison

Figure 34 compares the primary vertex distribution between data and inclusive $Z/\gamma^* \rightarrow e^+e^-$ PYTHIA MC.

6.3.2 Z p_T Comparisons

Figure 35 shows the Z p_T comparison between data and PYTHIA MC. Since PYTHIA does not fully incorporate higher-order contributions of hard radiation to the Drell-Yan (γ^*) process, there is a disagreement on the Z p_T distribution (especially at high p_T) with the data. To account for this discrepancy, an additional correction based on the Z p_T comparison between data and MC is applied. The Z p_T correction is also shown in Figure 35.

Figure 36 and Figure 37 show Z p_T comparisons when using ALPGEN + PYTHIA for

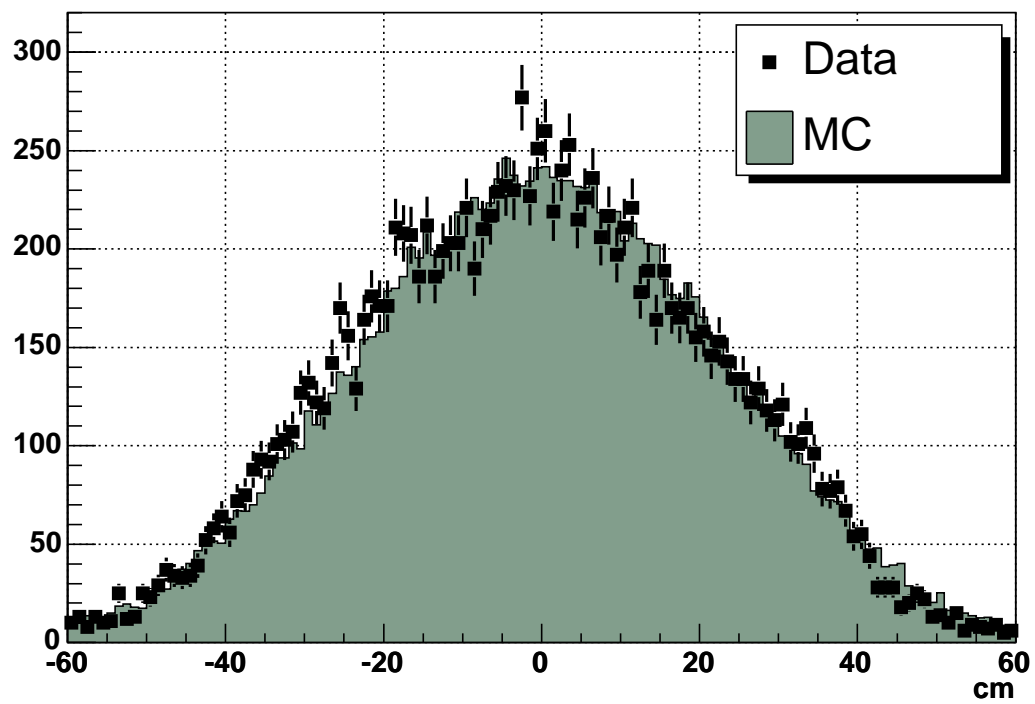


Figure 34. Primary vertex distribution in data and MC (PYTHIA) for the inclusive sample.

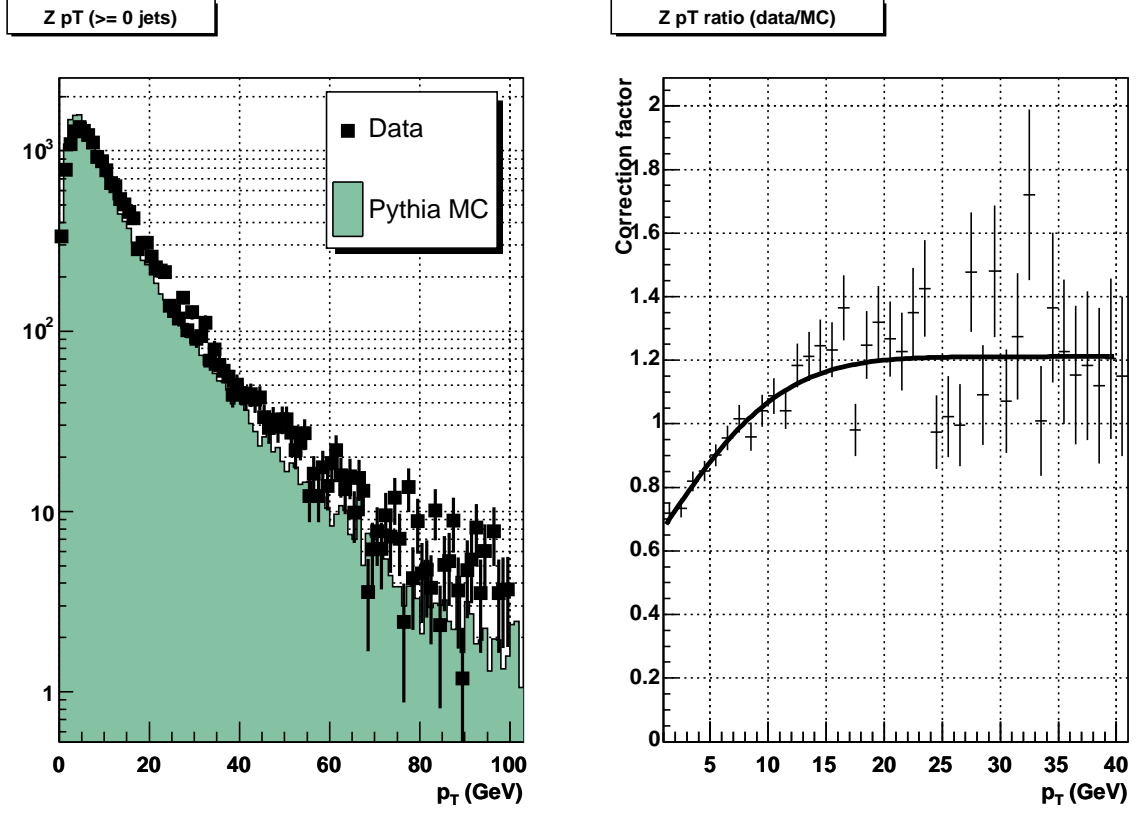


Figure 35. Comparing $Z p_T$ between data and PYTHIA MC (left), and ratio correction factor (right).

$Z+1$ jet and $Z+2$ jet samples. We do not apply an additional $Z p_T$ correction when using the ALPGEN MC samples.

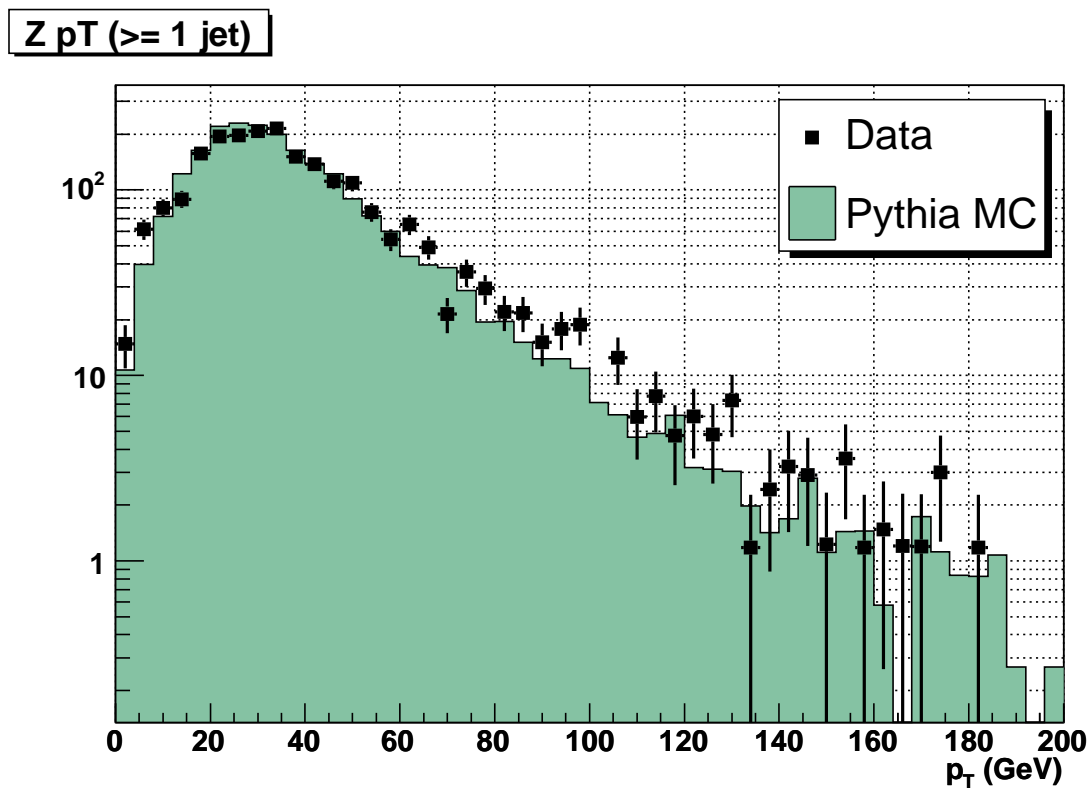


Figure 36. Comparing Z p_T between data and ALPGEN + PYTHIA $Z+1$ jet MC.

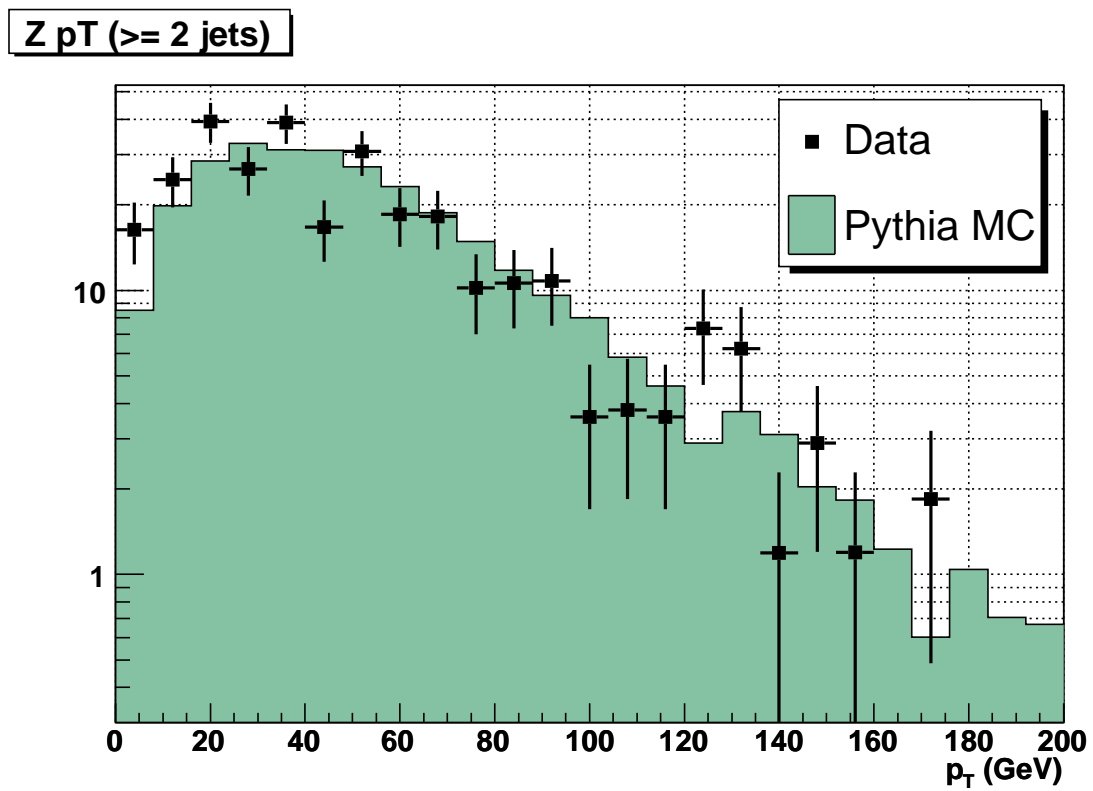


Figure 37. Comparing Z p_T between data and ALPGEN + PYTHIA $Z+2$ jets MC.

6.3.3 $Z/\gamma^* (\rightarrow e^+e^-) + \geq n$ Jet Comparisons

6.3.3.1 $Z/\gamma^* (\rightarrow e^+e^-)$ Inclusive Sample

We compare basic kinematic distributions for electrons and Z candidates after applying all corrections (Trigger, EM, Tracking, Z p_T - see Chapters 6.4.1 and 6.5.1 for a description of the corrections). All distributions are normalized by area. Figure 38 compares basic electron and Z kinematic properties ¹. Figure 39 compares the diem invariant mass distribution. The average Z mass is 91.02 GeV with a width of 4.03 GeV.

6.3.3.2 $Z/\gamma^* (\rightarrow e^+e^-) + \geq 1$ Jet Sample

Figure 40 shows comparisons of basic electron and Z distributions, Figure 41 shows a comparison of the diem invariant mass peak and Figure 42 and Figure 43 show comparisons of basic jet distributions ².

6.3.3.3 $Z/\gamma^* (\rightarrow e^+e^-) + \geq 2$ Jet Sample

Figure 44 shows comparisons of basic electron and Z distributions, Figure 45 shows a comparison of the diem invariant mass peak and Figure 46, Figure 47 and Figure 48 show comparisons of basic jet distributions.

¹We observe an excess of events in the electron η distribution at $\eta = -0.5$ and $\eta = 0.7$. This feature is still under investigation and is also present in other $D\bar{O}$ analyses.

²We observe an excess of events in the jet η distributions at $\eta = -0.4$. This feature is still under investigation. We checked η_{det} vs ϕ_{det} and η_{det} vs p_T distributions. The feature was more pronounced in the initial Pass 1 dataset of the analysis.

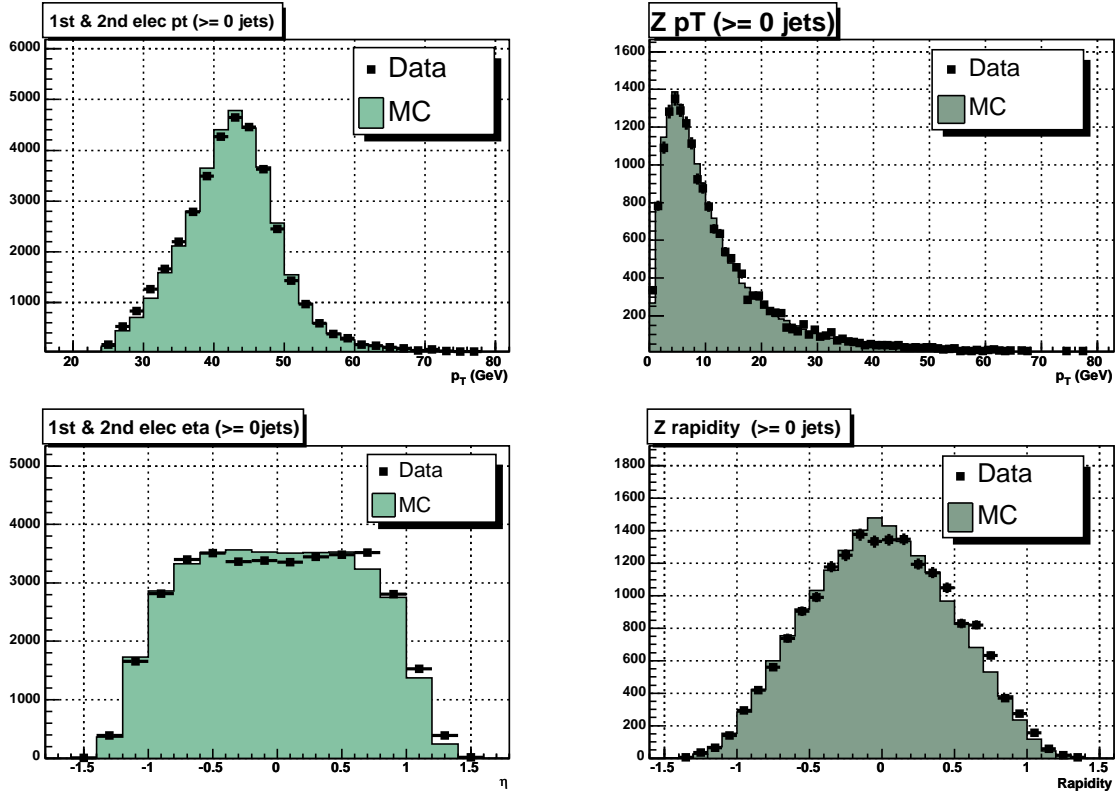


Figure 38. p_T of both Z electrons (top left), physics η of both Z electrons (bottom left), Z p_T (top right), Z rapidity (bottom right) for the $Z/\gamma^* \rightarrow e^+e^-$ inclusive sample in data and MC (PYTHIA).

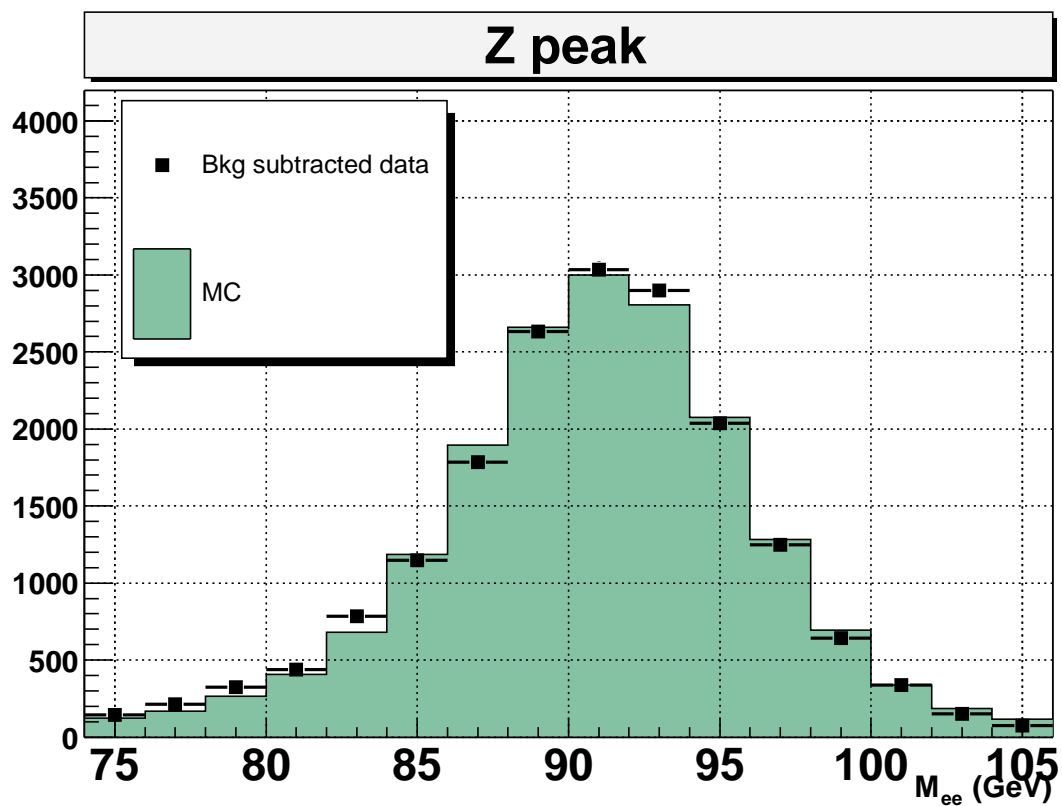


Figure 39. Dielectron invariant mass comparison for the $Z/\gamma^* \rightarrow e^+e^-$ inclusive sample in data and MC (PYTHIA). Data is background subtracted.

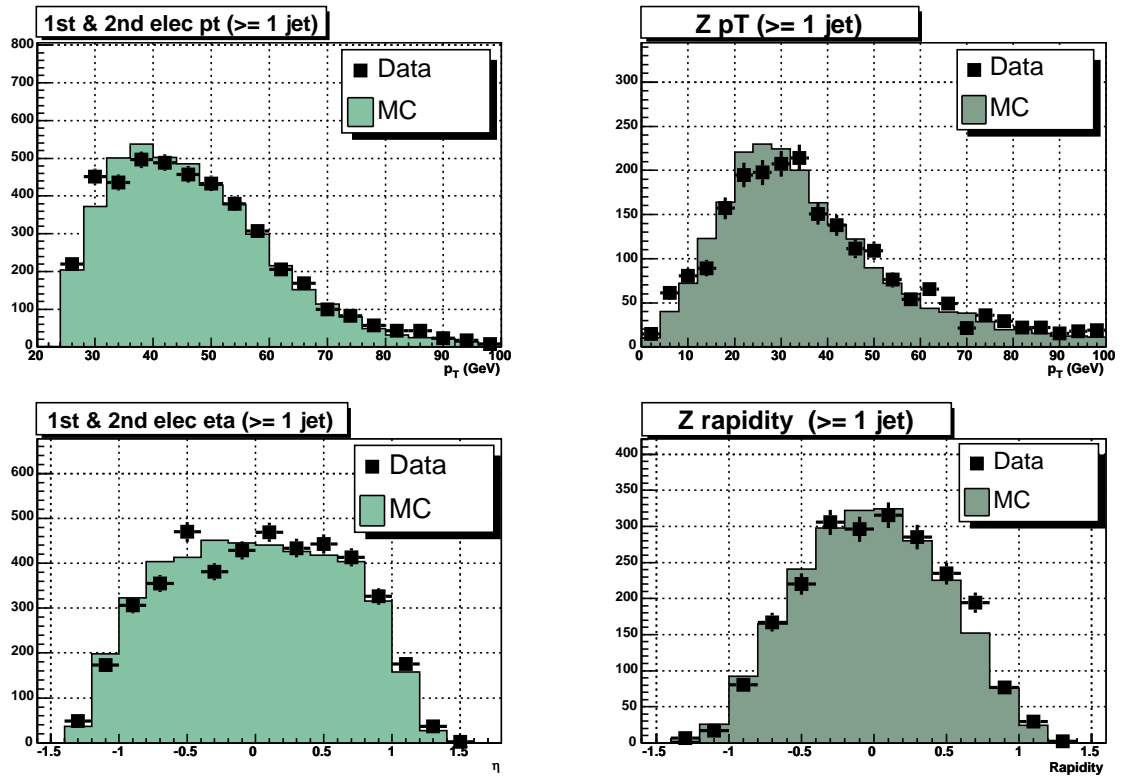


Figure 40. p_T of both Z electrons (top left), physics η of both Z electrons (bottom left), Z p_T (top right), Z rapidity (bottom right) for the $Z/\gamma^* \rightarrow e^+e^- + \geq 1 \text{ jet}$ sample in data and MC (ALPGEN).

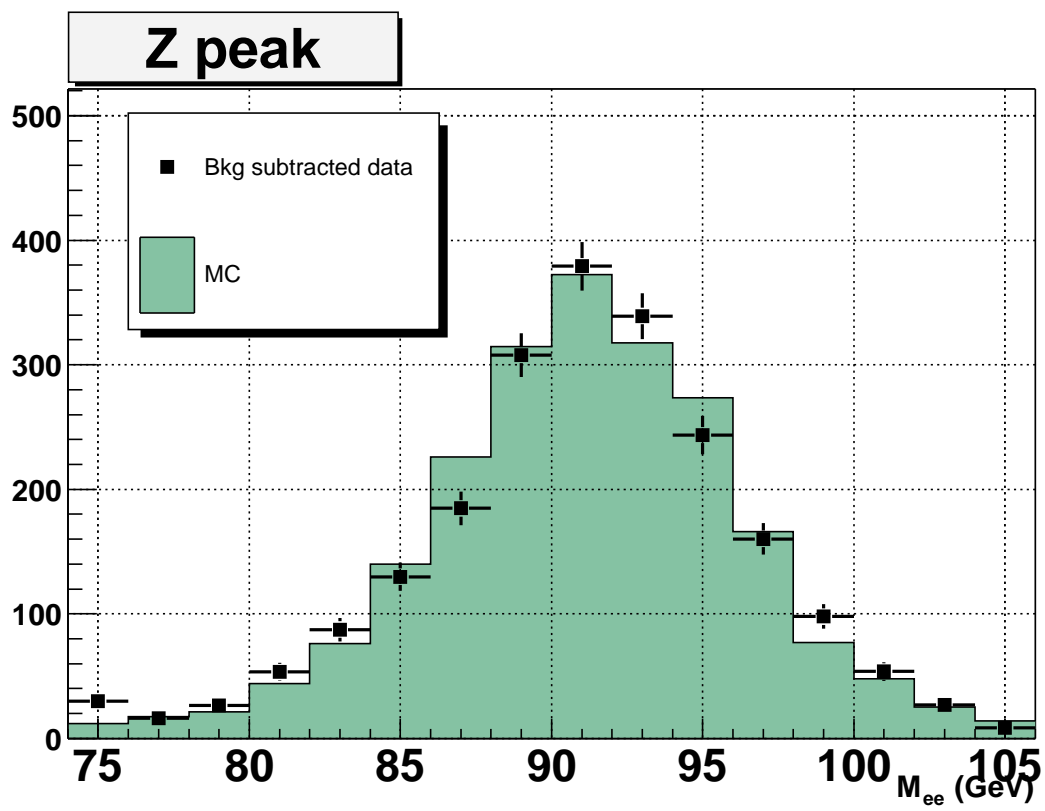


Figure 41. Diem invariant mass comparison for the $Z/\gamma^* \rightarrow e^+e^- + \geq 1$ jet sample in data and MC (ALPGEN). Data is background subtracted.

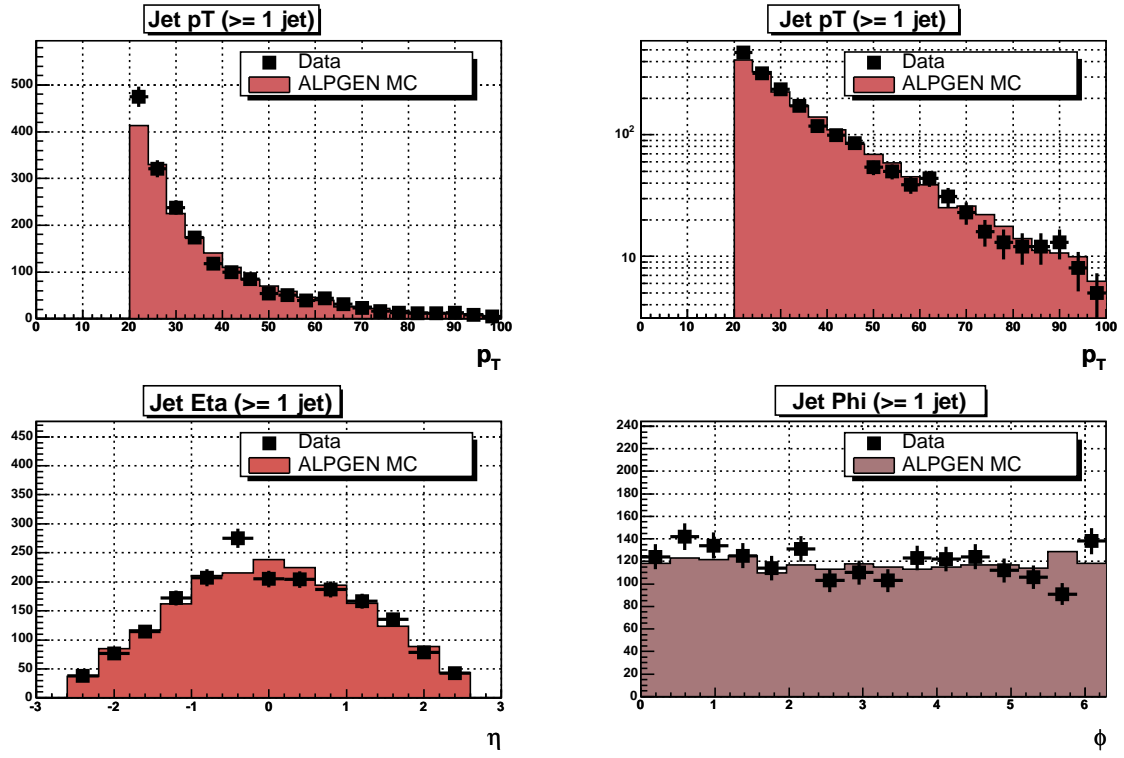


Figure 42. p_T (linear and logarithmic), physics η and physics Φ of all jets for the $Z/\gamma^* \rightarrow e^+e^- + \geq 1 \text{ jet}$ sample in data and MC (ALPGEN).

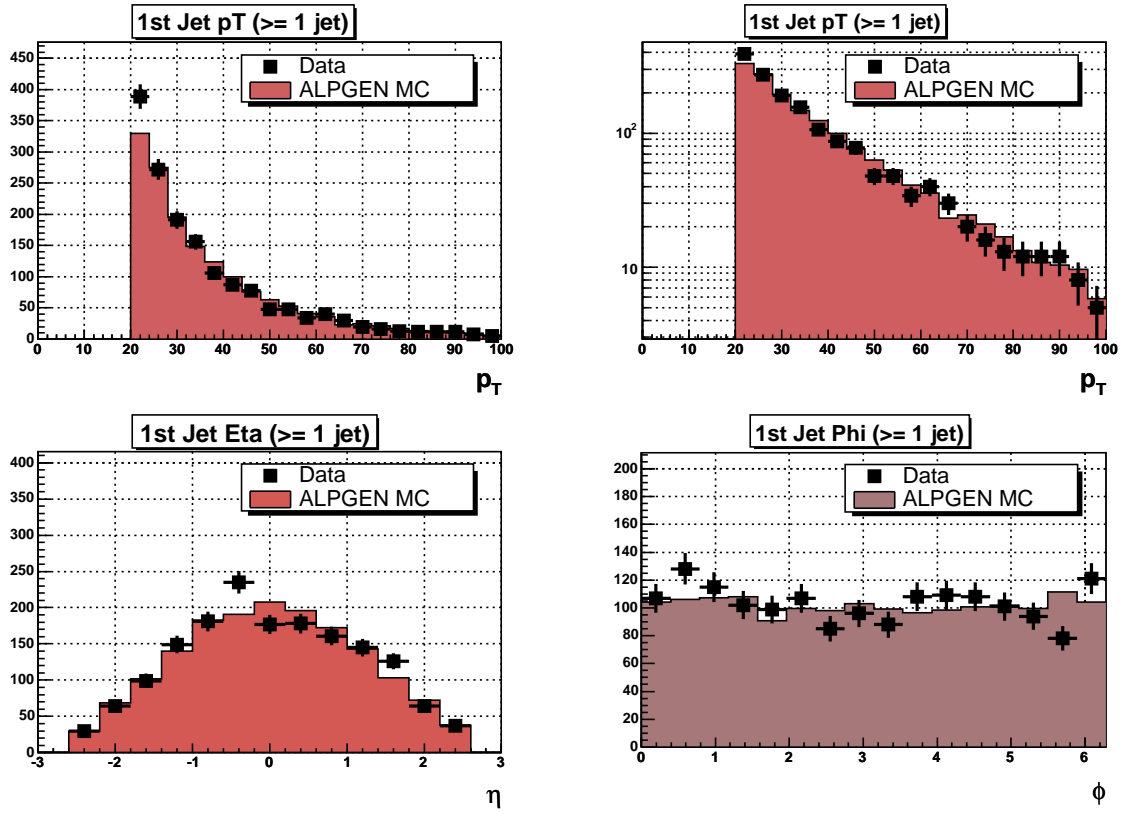


Figure 43. p_T (linear and logarithmic), physics η and physics Φ of the leading jets for the $Z/\gamma^* \rightarrow e^+e^- + \geq 1$ jet sample in data and MC (ALPGEN).

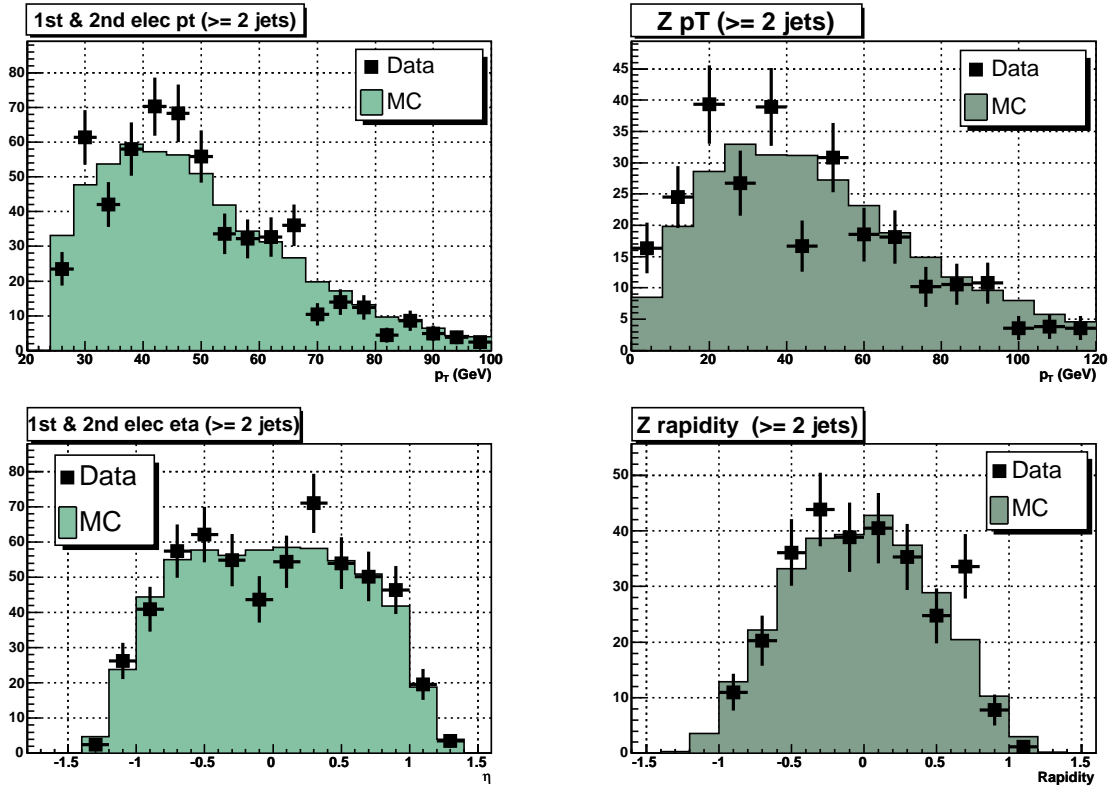


Figure 44. p_T of both Z electrons (top left), physics η of both Z electrons (bottom left), Z p_T (top right), Z rapidity (bottom right) for the $Z/\gamma^* \rightarrow e^+e^- + \geq 2 \text{ jet}$ sample in data and MC (ALPGEN).

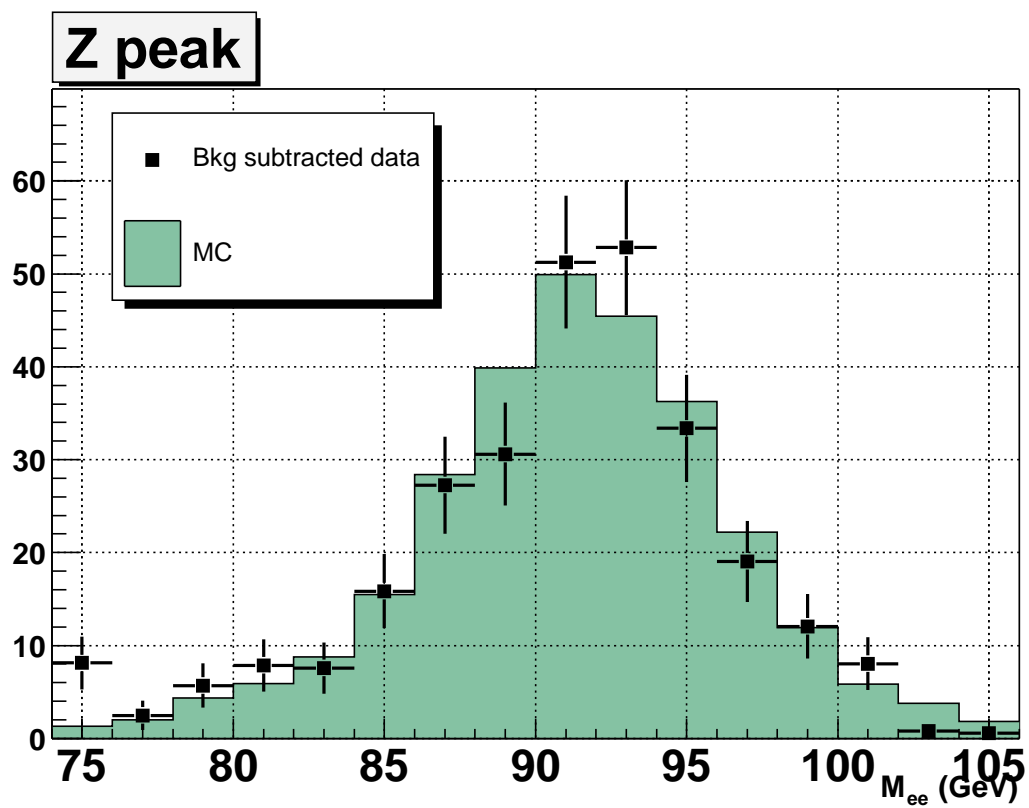


Figure 45. Diem invariant mass comparison for the $Z/\gamma^* \rightarrow e^+e^- + \geq 2$ jet sample in data and MC (ALPGEN). Data is background subtracted.

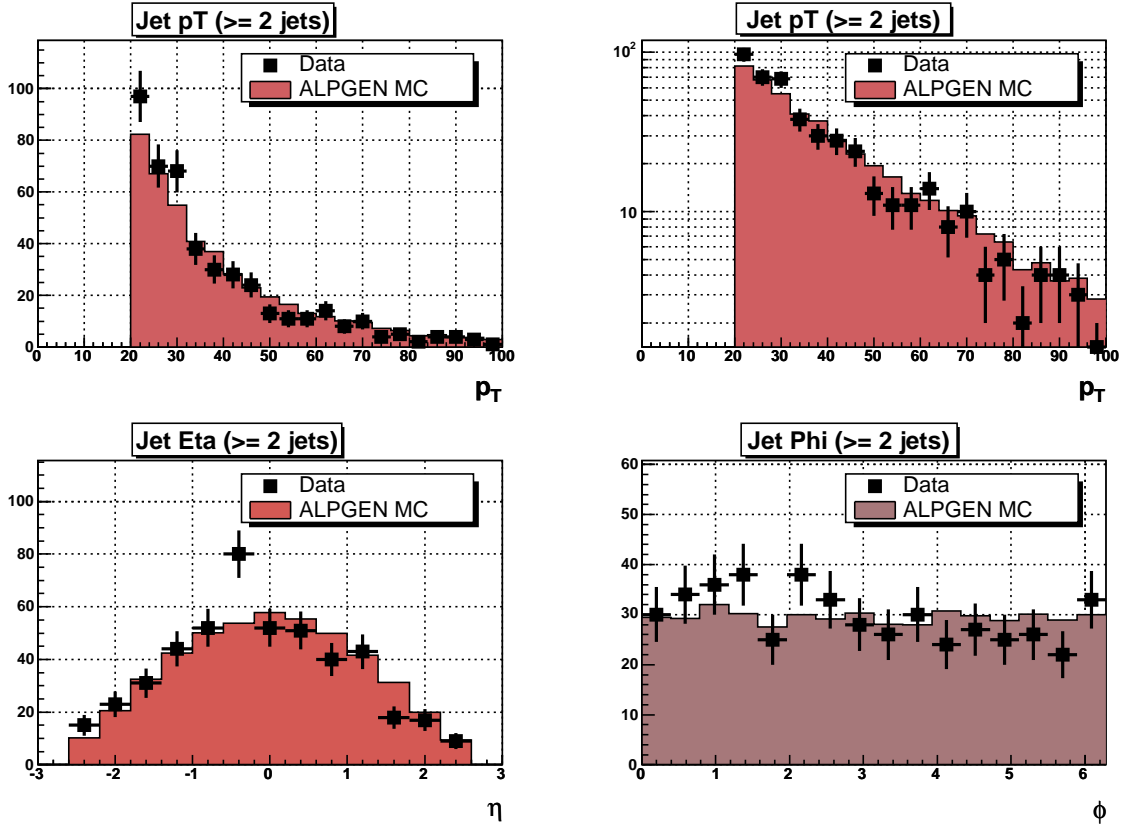


Figure 46. p_T (linear and logarithmic), physics η and physics Φ of all jets for the $Z/\gamma^* \rightarrow e^+e^- + \geq 2 \text{ jet}$ sample in data and MC (ALPGEN).

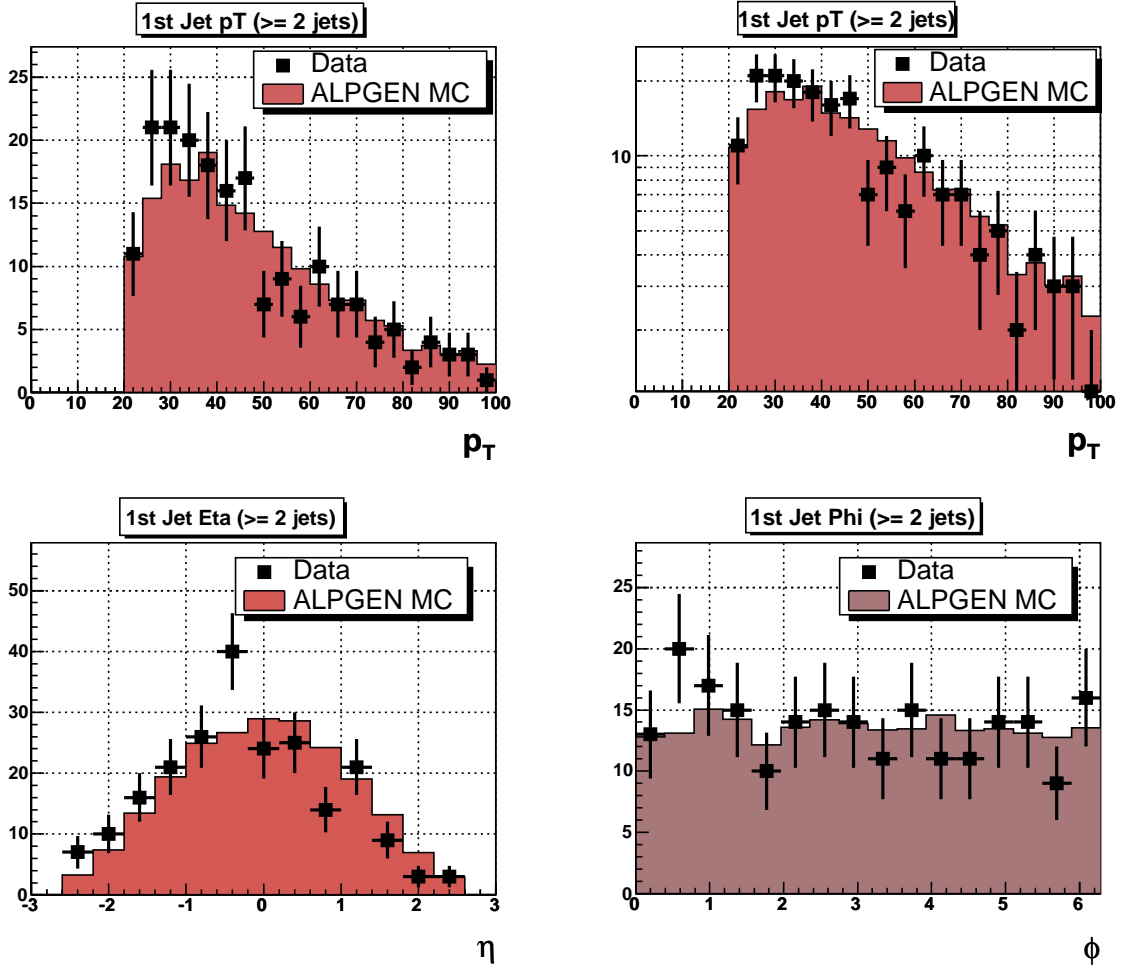


Figure 47. p_T (linear and logarithmic), physics η and physics Φ of the leading jets for the $Z/\gamma^* \rightarrow e^+e^- + \geq 2 \text{ jet}$ sample in data and MC (ALPGEN).

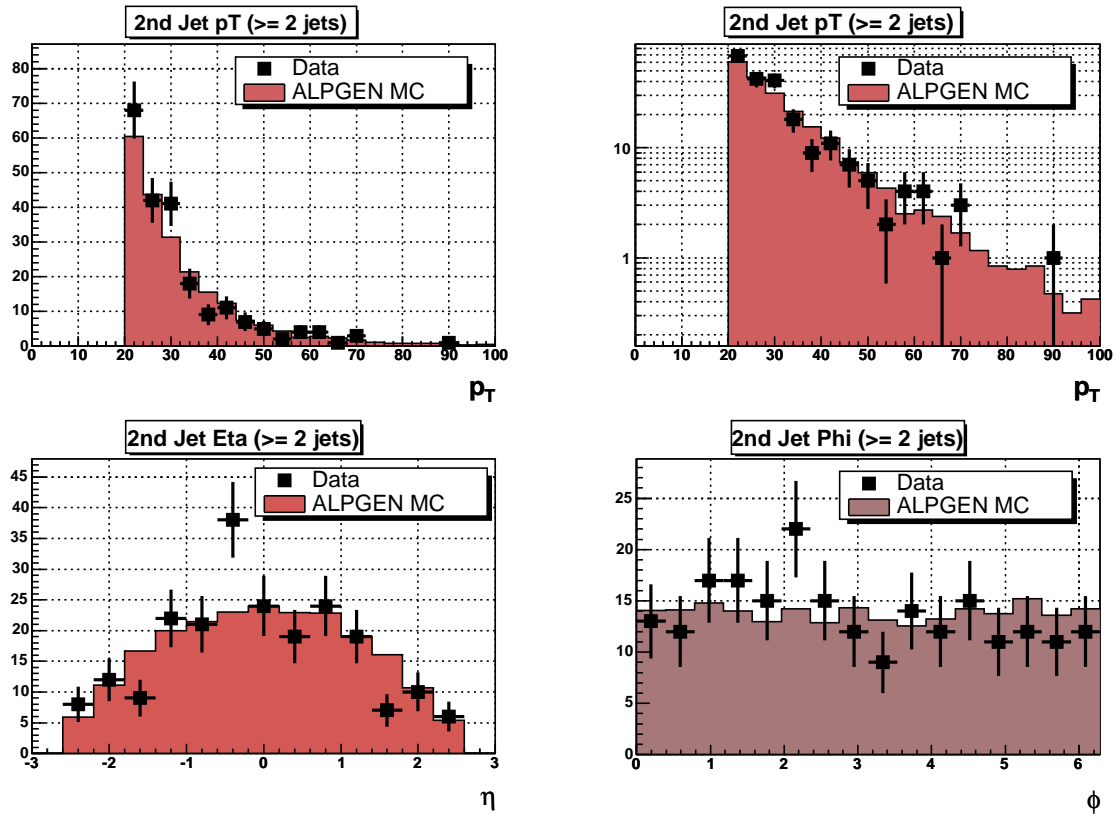


Figure 48. p_T (linear and logarithmic), physics η and physics Φ of the next to leading jets for the $Z/\gamma^* \rightarrow e^+e^- + \geq 2$ jet sample in data and MC (ALPGEN).

6.4 $Z/\gamma^* (\rightarrow e^+e^-)$ Inclusive Cross Section

In order to determine the $Z/\gamma^* \rightarrow e^+e^-$ inclusive cross section we evaluate the following equation:

$$\sigma \times \text{BR}(Z/\gamma^* \rightarrow e^+e^-) = \frac{N - B}{\mathcal{L} \times \varepsilon} \quad (6.3)$$

$N - B$ is the number of signal events which is estimated from the diem invariant mass histogram after background subtraction. The primary background is from multi-jet production from QCD processes in which the jets have a large electromagnetic component or they are mismeasured in such a way that they pass the electron selection criteria. The shape of the QCD background in the diem invariant mass histogram follows an exponential distribution.

Our goal is to measure the cross section for diem pairs where both γ^* (*Drell-Yan*) and Z boson exchange contribute. Contributions from pure Z boson decays will show up as a peak around the Z mass at ≈ 91 GeV in the diem invariant mass histogram. The Drell-Yan component follows an exponential distributions.

The total integrated luminosity of the dataset \mathcal{L} is approximately 343 pb^{-1} .

The efficiency ε to measure e^+e^- pairs coming from Z/γ^* decays can be split up into the following contributions:

$$\varepsilon_{tot} = \varepsilon_{trigger} \cdot \varepsilon_{EM} \cdot \varepsilon_{track} \cdot \varepsilon_{acceptance} \quad (6.4)$$

where $\varepsilon_{trigger}$ is the efficiency of the event to have at least one electron to pass all trigger levels, ε_{EM} is the efficiency of reconstructing two EM clusters which pass all electron ID cuts, ε_{track} is the efficiency of finding at least one track which matches an EM cluster and $\varepsilon_{acceptance}$ is the

efficiency of the kinematic and geometric electron cuts, the diem invariant mass cut and the primary vertex cut. Practically, we apply all efficiencies (except for $\varepsilon_{acceptance}$) as corrections to the diem invariant mass histogram. This procedure is outlined in the following chapters.

6.4.1 Efficiencies

6.4.1.1 Trigger Efficiency

The combined efficiency of all triggers per electron is studied with a *tag-and-probe method* using Z candidate events with invariant mass between 70 and 110 GeV. For this method, both Z candidate electrons are considered as possible “tags”. An electron becomes a “tag” if it passes trigger requirements for at least one unscaled trigger in the trigger combination. To pass the requirements of a trigger, an electron must have a matching trigger object at each level which passes all cuts for the corresponding trigger. Both the tag and probe electrons must satisfy the following requirements:

- $p_T > 20$ GeV
- EM Fraction > 0.9
- Isolation < 0.15
- H-Matrix(7) < 12
- Track match with $P(\chi^2) > 0.01$

The probe electron must have matching trigger objects at L1, L2 and L3 within $\Delta R = \sqrt{\Delta\eta^2 + \Delta\phi^2}$ of 0.4.

Trigger efficiencies are parameterized versus EM object p_T and derived separately for pre-v12

and v12 data. In cases where the L2 subsystem was not present (all runs with run numbers $\leq 169,523$) only L1 and L3 trigger objects were used. The average trigger efficiencies for the pre-v12 and v12 datasets are (with statistical errors):

- $\varepsilon_{pre-v12}(\text{Trigger}) = 94.6\% \pm 0.3\%$
- $\varepsilon_{v12}(\text{Trigger}) = 98.2\% \pm 0.1\%$

Figure 49 shows the parameterized trigger efficiencies for both datasets.

We correct for trigger inefficiencies in the following way:

- In a given event we use the trigger efficiency curves to get the trigger efficiencies ε_1 and ε_2 for the two EM objects (based on p_T).
- To get the event based trigger efficiency, we need to take into account all permutations for the two EM objects to fire a trigger:

$$\varepsilon_{trigger} = \varepsilon_1 \cdot (1 - \varepsilon_2) + \varepsilon_2 \cdot (1 - \varepsilon_1) + \varepsilon_1 \cdot \varepsilon_2 = \varepsilon_1 + \varepsilon_2 - \varepsilon_1 \cdot \varepsilon_2 \quad (6.5)$$

- The inverse of $\varepsilon_{trigger}$ is applied as a corrective weight when we fill the diem invariant mass histogram.
- We use the corrected diem invariant mass histogram to derive the number of signal events for the cross section calculation.

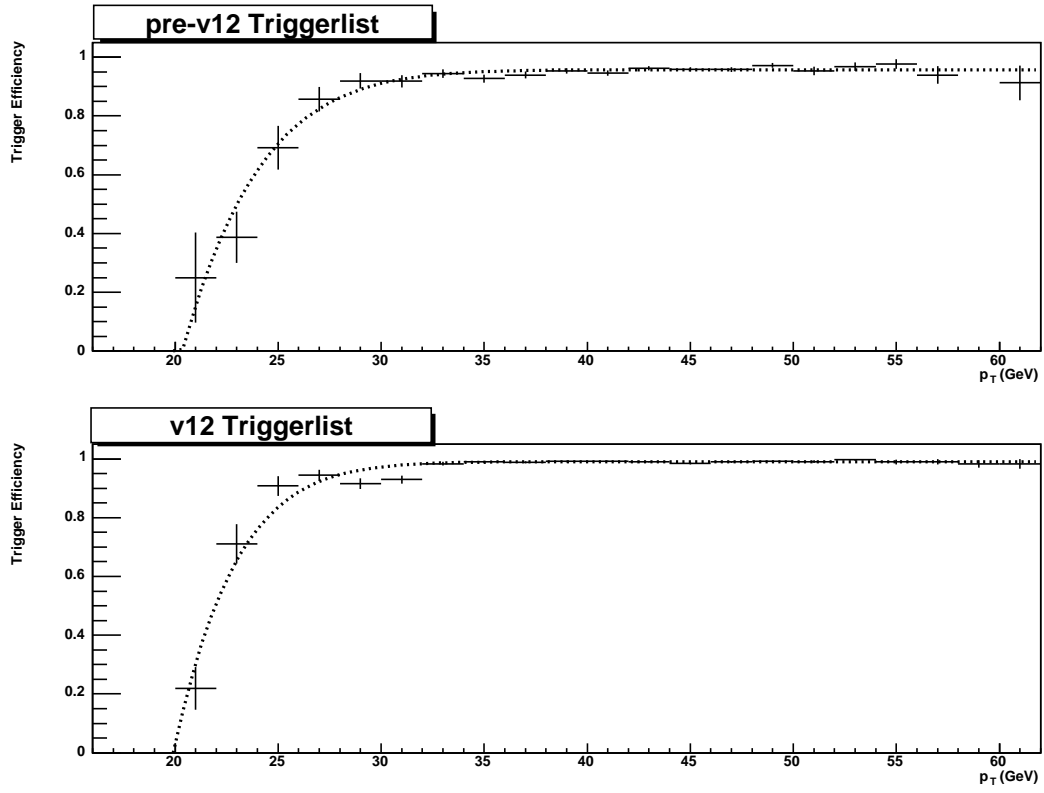


Figure 49. Trigger efficiencies for pre-v12 (top) and v12 (bottom) datasets vs EM object p_T

6.4.1.2 EM Reconstruction and Identification Efficiency

To determine EM efficiencies a tag and probe method is used where the tag leg consists of an electron candidate and the probe leg of a track. The tag electron must pass all the electron selection cuts, have a good track match and satisfy trigger requirements for the event. There must also be a second track (probe track) in the event. Both tag- and probe-tracks must pass the following selection criteria (60):

- stereo track¹
- $25 \text{ GeV} < p_T < 80 \text{ GeV}$
- χ^2 probability for best track < 8 (using the distance in η/Φ and E/p)
- Distance of closest approach between track and beam position in the R- Φ plane $< 0.3\text{cm}$
- Δz_{vertex} of the two tracks $< 4\text{cm}$
- $|\eta_{\text{detector}}| < 1.1$

Tag electron selection criteria:

- ID = 10 or ± 11
- EMFraction > 0.9
- Isolation < 0.15
- H-Matrix(7) < 12

¹Requiring hits in stereo layers of the tracking system.

- $p_T > 25$ GeV
- $|\eta_{det}| < 1.1$
- No fiducial restrictions in ϕ
- Matched with tag track within $\Delta R = \sqrt{\Delta\eta^2 + \Delta\phi^2} = \sqrt{0.1^2 + 0.1^2}$ of 0.14
- Must have fired the trigger

Ways to reduce possible background contamination:

- tag- and probe-tracks are required to have opposite signs
- Missing $E_T < 15$ GeV

Additional requirements:

- $|PVZ| < 60$ cm
- Tag-electron-probe-track invariant mass cut: $70 \text{ GeV} < M_{ee} < 110 \text{ GeV}$
- Sideband background subtraction¹ (only used to derive average efficiencies).

Once an event is found which satisfies all of the above requirements, a denominator histogram is filled, i.e. probe track ϕ and p_T histograms for parameterized efficiencies and tag-electron-probe-track diem invariant mass histograms for average efficiencies. In the case a reconstructed EM cluster is found nearby the probe-track ($\Delta R = \sqrt{\Delta\eta^2 + \Delta\phi^2} = \sqrt{0.1^2 + 0.1^2} = 0.14$) which

¹This method uses the sidebands of the diem invariant mass distribution to estimate background and extrapolate it into the signal region.

passes the EMID cuts (HMx, EMF, Iso), the respective numerator histogram is filled.

The average EM reco and ID efficiencies in data and MC are (with statistical errors):

- $\varepsilon_{data}(\text{EM}) = 88.9\% \pm 0.3\%$
- $\varepsilon_{MC}(\text{EM}) = 93.1\% \pm 0.1\%$

For average efficiencies we reduce the background to a minimum by requiring opposite sign tracks and missing $E_T < 15$ GeV. In addition we subtract background using the sidebands in the tag-electron-probe-track invariant mass distribution. As a cross check we derive the average efficiency in data without sideband background subtraction. The result is within 1% of the sideband subtracted value: $88.2\% \pm 0.2\%$.

Figure 50 and Figure 51 show the EM efficiencies for data and MC in a one-dimensional parameterization. Note that the central calorimeter has narrow uninstrumented regions between the azimuthal module boundaries (*phi cracks*). An EM object entering the calorimeter near these boundaries can lose a portion of its energy to these cracks, which results in decreased EM efficiencies for these regions.

We correct for EM inefficiencies in the following way:

- In a given event we use two-dimensional efficiency curves (versus p_T and Φ) to estimate the EM efficiencies ε_1 and ε_2 for the two EM objects (based on their p_T and Φ).
- To estimate the event based EM efficiency we take the product of ε_1 and ε_2 :

$$\varepsilon_{EM} = \varepsilon_1 \cdot \varepsilon_2 \tag{6.6}$$

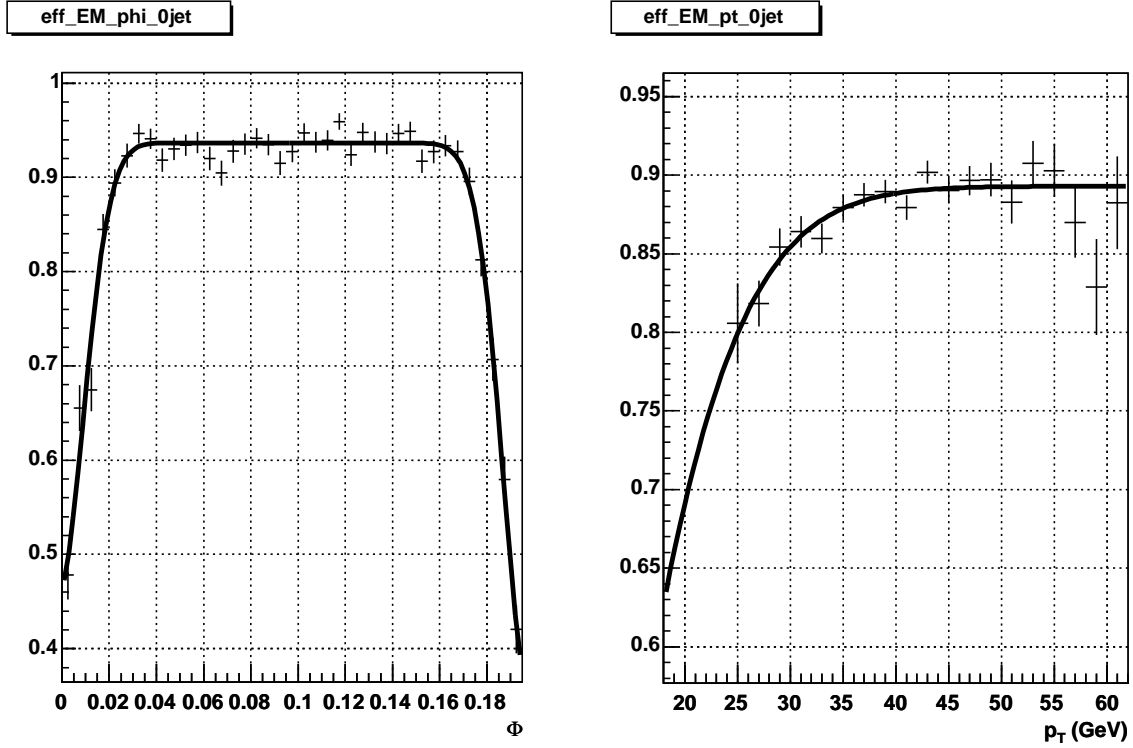


Figure 50. EM efficiencies versus probe track Φ and p_T in data. The Φ distribution shows the $\text{modulus}(\Phi, \frac{2\pi}{32})$ distribution to illustrate the effect of the calorimeter Φ -module boundaries.

- The inverse of ε_{EM} is applied as a corrective weight when we fill the diem invariant mass histogram.

6.4.1.3 EM-Track Match Efficiency

Average track finding and matching efficiencies are derived using diem invariant mass histograms (Figure 52 to Figure 55).

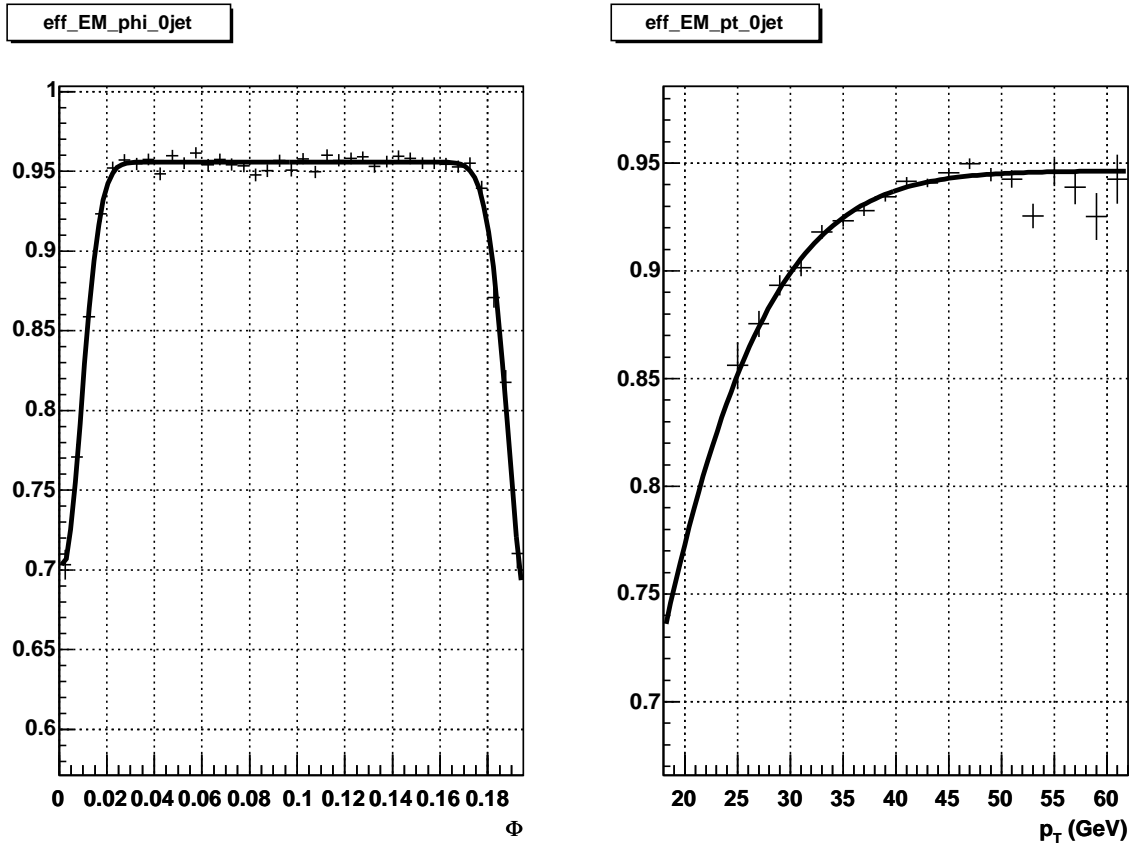


Figure 51. EM efficiencies versus probe track Φ and p_T in MC. The Φ distribution shows the modulus($\Phi, \frac{2\pi}{32}$) distribution to illustrate the effect of the calorimeter Φ -module boundaries.

Using a convolution of a Gaussian and Breit-Wigner fit for the Z peak and an exponential shape to describe the QCD and Drell-Yan contributions, we extract the number of events under the Z peak from the four diem invariant mass histograms: $N_{1trk}(data)$, $N_{2trk}(data)$, $N_{1trk}(MC)$ and $N_{2trk}(MC)$. $N_{1trk}(data)$ and $N_{1trk}(MC)$ are the number of Z candidates when requiring at least one track match in data and MC; $N_{2trk}(data)$ and $N_{2trk}(MC)$ are the number of Z candidates when requiring exactly two track matches in data and MC. We use these numbers to estimate the average track finding and matching efficiencies in data and MC:

$$\varepsilon_{data}(\text{Tracking}) = \frac{2 \cdot N_{2trk}(data)}{N_{2trk}(data) + N_{1trk}(data)} = 77.1\% \pm 0.3\% \quad (6.7)$$

$$\varepsilon_{MC}(\text{Tracking}) = \frac{2 \cdot N_{2trk}(MC)}{N_{2trk}(MC) + N_{1trk}(MC)} = 87.8\% \pm 0.03\% \quad (6.8)$$

We correct for the tracking inefficiencies in the following way:

- In each event we use the average tracking efficiency $\varepsilon_{average}$.
- To get the event based tracking efficiency we need to take all permutations for one or two tracks into account:

$$\varepsilon_{tracking} = 2 \cdot \varepsilon_{average}(1 - \varepsilon_{average}) + \varepsilon_{average}^2 = 2 \cdot \varepsilon_{average} - \varepsilon_{average}^2 \quad (6.9)$$

- The inverse of $\varepsilon_{tracking}$ is applied as a corrective weight when we fill the diem invariant mass histogram.

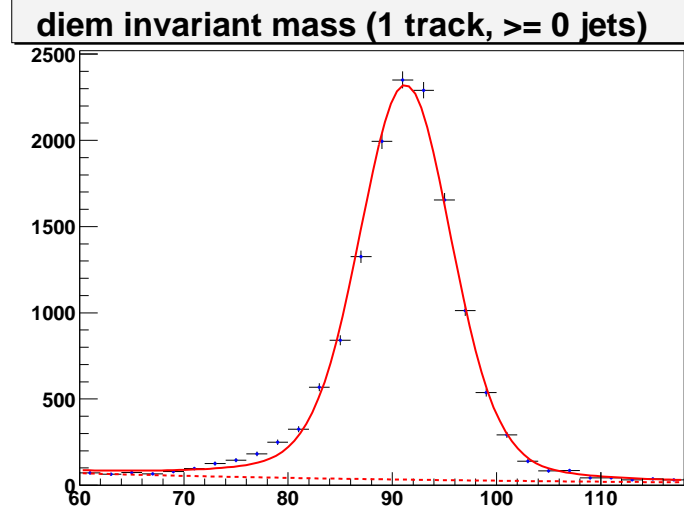


Figure 52. Invariant mass in data when requiring at least one track-matched electron.

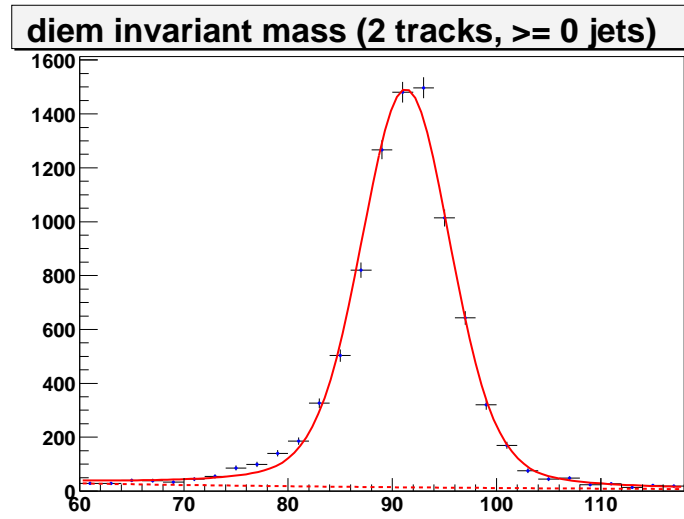


Figure 53. Invariant mass in data when requiring two track-matched electrons.

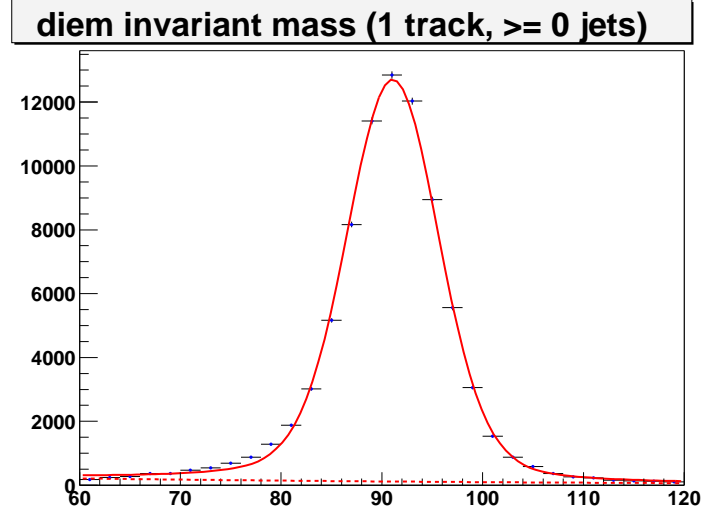


Figure 54. Invariant mass in MC when requiring at least one track-matched electron.

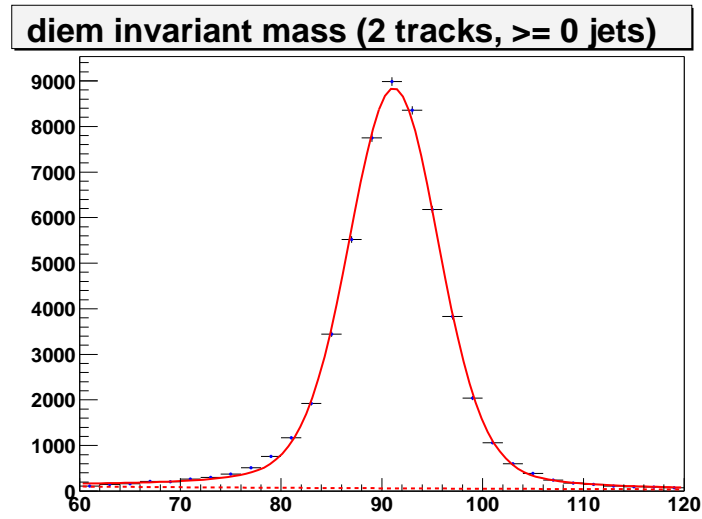


Figure 55. Invariant mass in MC when requiring two track-matched electrons.

6.4.1.4 Acceptance

We use the $Z/\gamma^* \rightarrow e^+e^-$ PYTHIA MC sample to estimate the acceptance. The numerator contains the number of events satisfying the following requirements at the reconstructed level:

- Primary vertex cut: $|PVZ| < 60$ cm
- Electron cuts: $p_T > 25$ GeV and $|\eta| < 1.1$
- Diem invariant mass cut: $75 \text{ GeV} < M_{ee} < 105 \text{ GeV}$

The denominator contains the number of events with generated Z/γ^* particles that are within the diem invariant mass window.

We estimate the acceptance with statistical error for inclusive $Z/\gamma^* \rightarrow e^+e^-$ to be:

$$\text{Acceptance}(Z/\gamma^* \rightarrow e^+e^- + \text{X}) = 21.4\% \pm 0.1\% \quad (6.10)$$

Since the numerator in the acceptance calculation involves two reconstructed electrons, we apply a corrective weight to the numerator. Based on the p_T and Φ values of the two electrons, we estimate their reconstruction efficiencies (98% on average). The product of the inverse of those reconstruction efficiencies yields the corrective weight. We also apply the Z p_T correction factor (see Chapter 6.3.2) as an additional weight in both numerator and denominator of the acceptance.

6.4.2 Cross section calculation

After applying all corrections we estimate the number of (corrected) signal events from the diem invariant mass distribution (Figure 56). We fit a convolution of a Gaussian and Breit-

Wigner shape to the Z peak and an exponential shape to describe the QCD and Drell-Yan contributions. We justify the choice of using an exponential shape for the QCD background by looking at the diem invariant mass distribution of EM object pairs that were selected by applying “anti-electron cuts”:

- All criteria that are applied to loose electron candidates as described in Section 6.2.2 except for the H-Matrix cut.
- $\text{H-Matrix}(7) > 35$
- Two of these objects per event.

In this way we select two jets with high electromagnetic energy content in the shower.

Since the Drell-Yan component is part of our signal, we need to disentangle the QCD component from the Drell-Yan component. Using the inclusive $Z/\gamma^* \rightarrow e^+e^-$ PYTHIA MC sample we determine the percentage of Drell-Yan events in $Z/\gamma^* \rightarrow e^+e^-$ decays by fitting a Gaussian and Breit-Wigner shape to the Z component and an exponential shape to the Drell-Yan component. We find that 2.06% of the events in the inclusive $Z/\gamma^* \rightarrow e^+e^-$ sample are due to Drell-Yan.

Based on these fits we extract the number of signal events from direct Z Boson and Drell-Yan decays as well as the number of QCD background events in the diem invariant mass signal window ($75 \text{ GeV} < M_{ee} < 105 \text{ GeV}$) ¹:

¹The number of signal events is derived by counting all entries for a particular M_{ee} bin and subtracting from it the number of entries from the background fit.

- Number of signal events from Z Boson and Drell-Yan decays = 18,263.8
- Number of QCD background events = 407.5

Based on the integrated luminosity (343 pb^{-1}) and the acceptance (21.4%) we calculate the inclusive $Z/\gamma^* \rightarrow e^+e^-$ cross section:

$$\sigma \times \text{BR}(Z/\gamma^* \rightarrow e^+e^-) = \frac{N - B}{\mathcal{L} \times A} = 248.9 \text{ pb} \pm 2.5(\text{stat}) \quad (6.11)$$

As an additional cross check, we perform a MC closure test. Going through the entire procedure using MC parameters only, we calculate a cross section of 179 pb with a MC input cross section of 183 pb.

6.4.3 Comparisons to other measurements

Using the inclusive PYTHIA MC sample we derive correction factors which allow us to estimate the Z/γ^* inclusive cross section for different diem invariant mass windows ¹. To calculate the correction factors we count the number of Z/γ^* candidates at the particle level within different diem invariant mass ranges and take the ratio which yields the correction that is needed to account for the change in the diem invariant mass range.

Using the cross section ratio between the inclusive Z/γ^* cross section and the inclusive Z cross section in MC, we derive another correction factor which allows us to convert the measured inclusive Z/γ^* cross section into the inclusive Z cross section (61).

¹The MC sample used a generator cut of $|\eta_Z| < 4.2$. Although no restriction in η_Z would have been preferable, we do not believe that it has a big impact on the final results.

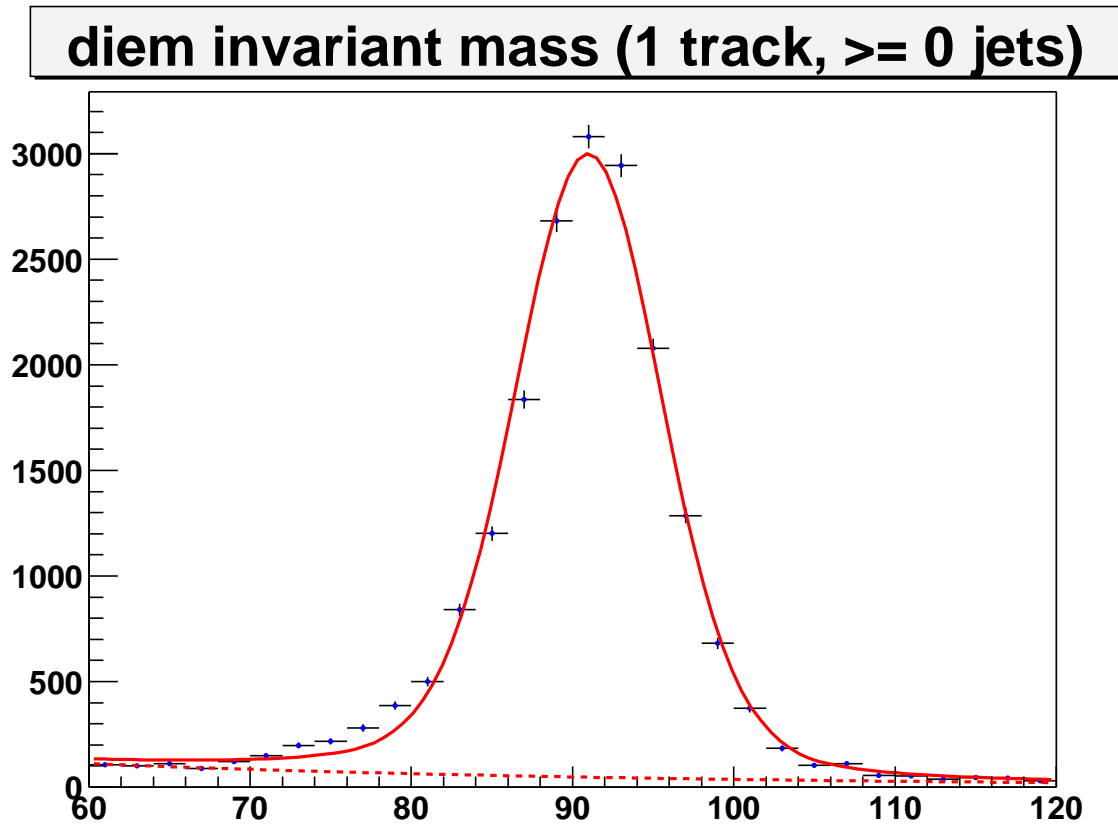


Figure 56. Diem invariant mass distribution for $Z/\gamma^* \rightarrow e^+e^- + X$ (Mean = $91.02 \text{ GeV} \pm 0.04 \text{ GeV}$, Width $4.03 \text{ GeV} \pm 0.04 \text{ GeV}$).

Process	Mass Range	Conversion
(a) Z/γ^*	$75 \text{ GeV} < M_{ee} < 105 \text{ GeV}$	248.9 pb
(b) Z/γ^*	$66 \text{ GeV} < M_{ee} < 116 \text{ GeV}$	$248.9 \text{ pb} \cdot \frac{392,174}{379,255} = 257.4 \text{ pb}$
(c) Z/γ^*	$60 \text{ GeV} < M_{ee} < 130 \text{ GeV}$	$248.9 \text{ pb} \cdot \frac{400,000}{379,255} = 262.5 \text{ pb}$
(d) Z	$60 \text{ GeV} < M_{ee} < 130 \text{ GeV}$	$248.9 \text{ pb} \cdot \frac{1.852}{1.869-0.948} = 260.2 \text{ pb}$

TABLE VI

CROSS SECTION RESULTS FOR DIFFERENT DIEM INVARIANT MASS RANGES AND PROCESSES.

Table VI lists our inclusive Z/γ^* cross section for different mass ranges, as well as the conversion into the inclusive cross section for pure Z boson exchange. We compare result (b) with the CDF measurement (62) for the inclusive Z/γ^* cross section ($66 \text{ GeV} < M_{ee} < 116 \text{ GeV}$): $255.8 \text{ pb} \pm 3.9(\text{stat})$.

$Z/\gamma^* (\rightarrow e^+e^-) + \geq n \text{ Jets Cross Section}$

In this section we outline the procedure to measure the $Z/\gamma^* \rightarrow e^+e^-$ production cross section for different inclusive jet multiplicities. For each jet multiplicity we determine the number of signal events from the diem invariant mass histograms. All efficiencies are examined for jet multiplicity dependence and applied to the diem invariant mass distributions as corrections (acceptance corrections are applied separately). We take into account jet reconstruction inefficiencies, as well as jet acceptance losses due to the electron-jet-overlap cut. The final cross sections are quoted for parton level jets (as opposed to calorimeter jets). We describe the *un-*

Jet multiplicity	pre-v12	v12
≥ 0	$94.6\% \pm 0.3\% \pm 5.0\%$	$98.2\% \pm 0.1\% \pm 5.0\%$
≥ 1	$93.1\% \pm 1.0\% \pm 5.0\%$	$96.9\% \pm 0.5\% \pm 5.0\%$
≥ 2	$95.2\% \pm 2.1\% \pm 5.0\%$	$95.5\% \pm 1.7\% \pm 5.0\%$

TABLE VII

OBJECT BASED TRIGGER EFFICIENCIES WITH STATISTICAL AND SYSTEMATIC ERRORS (RESPECTIVELY) FOR THE PRE-V12 AND V12 DATASETS FOR DIFFERENT INCLUSIVE JET MULTIPLICITIES.

smearing procedure that is used to convert calorimeter level jet multiplicities to particle level jet multiplicities.

6.5.1 Efficiencies vs Jet Multiplicity

In the following sections we use the PYTHIA MC sample to derive corrections for the inclusive sample, and ALPGEN MC samples for the n-jet corrections.

6.5.1.1 Trigger Efficiency

We do not observe significant variations in the trigger efficiencies as jet activity increases (Figure 57). Therefore the same trigger corrections as for the inclusive sample are applied (see Chapter 6.4.1.1). Table VII summarizes electron trigger efficiencies for the pre-v12 and v12 datasets for different inclusive jet multiplicities. We assign an additional systematic error of $\pm 5\%$ for all jet multiplicities.

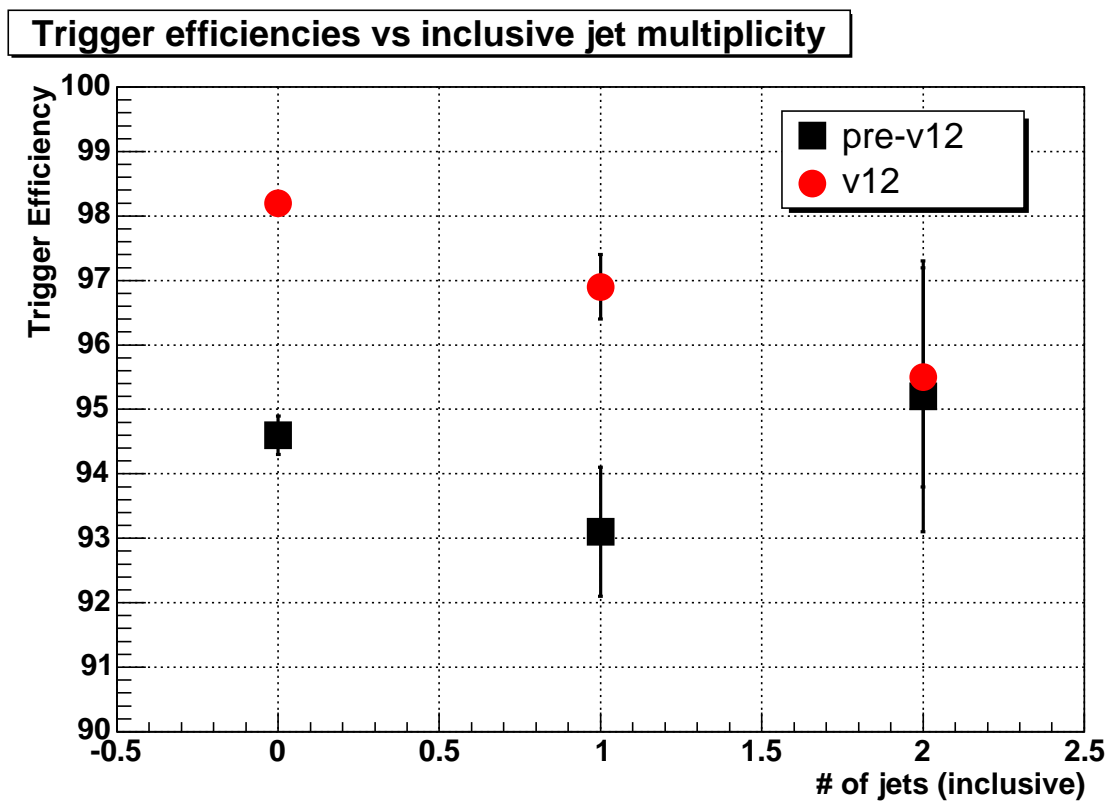


Figure 57. Average object based trigger efficiencies in data versus inclusive jet multiplicity.

6.5.1.2 EM Reconstruction and Identification Efficiency

We apply the same EM corrections as for the inclusive sample to each jet multiplicity sample (see Chapter 6.4.1.2). In addition we estimate residual inefficiencies due to additional jet activity by looking at the distribution of average electron EM reco and ID efficiencies versus jet multiplicity (Figure 58). The averaged efficiencies are derived using the procedure outlined in Chapter 6.4.1.2 for data and MC samples of different jet multiplicities.

Table VIII summarizes the electron EM reco and ID efficiencies in data and MC for different jet multiplicities. No significant change of the average efficiencies with respect to jet multiplicity is observed in data. Therefore no additional correction is applied. Due to the variation of the various efficiencies a systematic error of $\pm 3\%$ is assigned for all jet multiplicities.

Based on the drop in MC we apply a factor of 1.02^2 as a corrective weight to each event. This value is derived by taking the ratio of the EM efficiency for the inclusive sample and the average of the EM efficiencies for the 1-jet, 2-jet and 3-jet samples.

6.5.1.3 EM-Track Match Efficiency

Figure 59 and Table IX show the average object based tracking efficiencies for different jet multiplicities. In MC we use the value from the inclusive sample to correct for tracking inefficiencies for all jet multiplicities. In data we use the inclusive value for the inclusive sample, the 1-jet value for the 1-jet sample and the 2-jet value for all other jet samples.

Table X lists the systematic errors for the data efficiencies. For the 1-jet and 2-jet samples, we use the respective statistical errors as systematics. For the 3-jet, 4-jet and 5-jet samples,

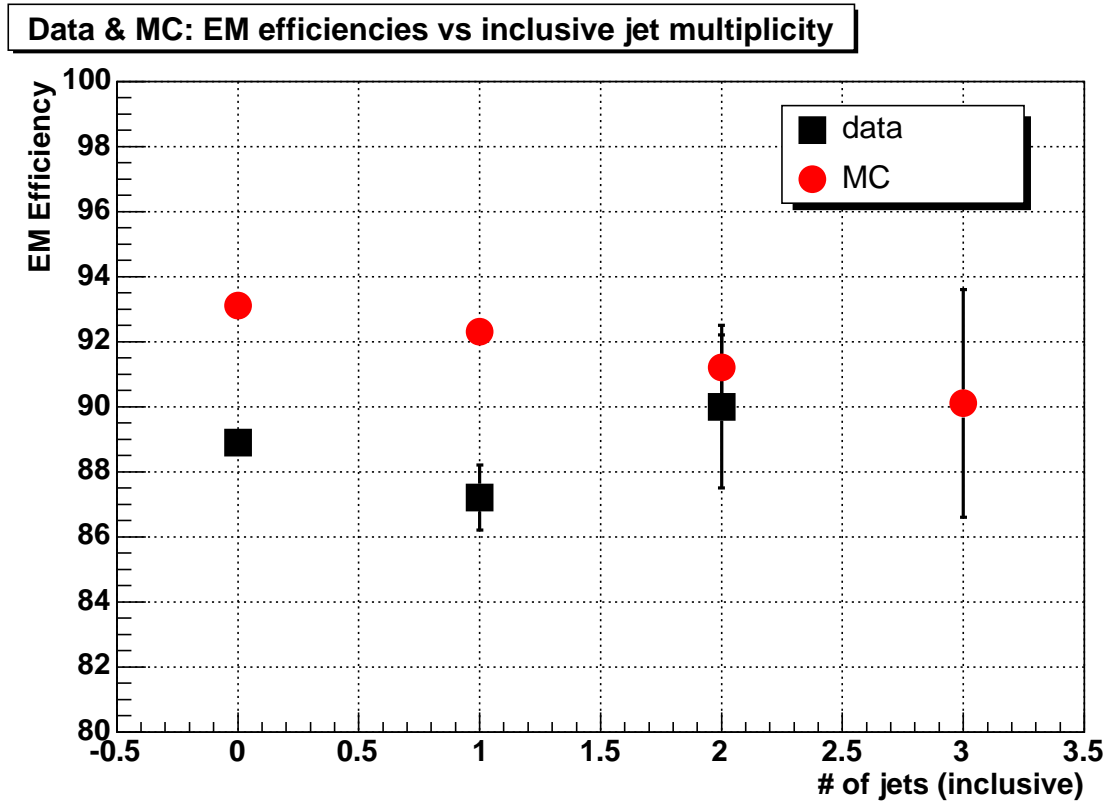


Figure 58. Average object based EM reco and ID efficiencies in data and MC versus inclusive jet multiplicity.

Jet multiplicity	data	MC
≥ 0	$88.9\% \pm 0.3\% \pm 3.0\%$	$93.1\% \pm 0.1\%$
≥ 1	$87.2\% \pm 1.0\% \pm 3.0\%$	$92.3\% \pm 0.3\%$
≥ 2	$90.0\% \pm 2.5\% \pm 3.0\%$	$91.2\% \pm 1.0\%$
≥ 3	(n/a)	$90.1\% \pm 3.5\%$

TABLE VIII

OBJECT BASED EM RECO AND ID EFFICIENCIES WITH STATISTICAL AND SYSTEMATIC ERRORS (RESPECTIVELY) IN DATA AND MC FOR DIFFERENT INCLUSIVE JET MULTIPLICITIES. THERE WAS NOT ENOUGH STATISTICS AVAILABLE TO ESTIMATE THE EM EFFICIENCY IN DATA FOR ≥ 3 JETS.

Jet multiplicity	data	MC
≥ 0	$77.1\% \pm 0.3\%$	$87.8\% \pm 0.03\%$
≥ 1	$74.5\% \pm 0.9\%$	$87.7\% \pm 0.3\%$
≥ 2	$72.1\% \pm 2.5\%$	$87.5\% \pm 0.9\%$

TABLE IX

OBJECT BASED TRACKING EFFICIENCIES WITH STATISTICAL ERRORS IN DATA AND MC FOR DIFFERENT INCLUSIVE JET MULTIPLICITIES.

we add the 2-jet statistical error in quadrature with the difference between a linear fit to the available data points and the 2-jet efficiency value.

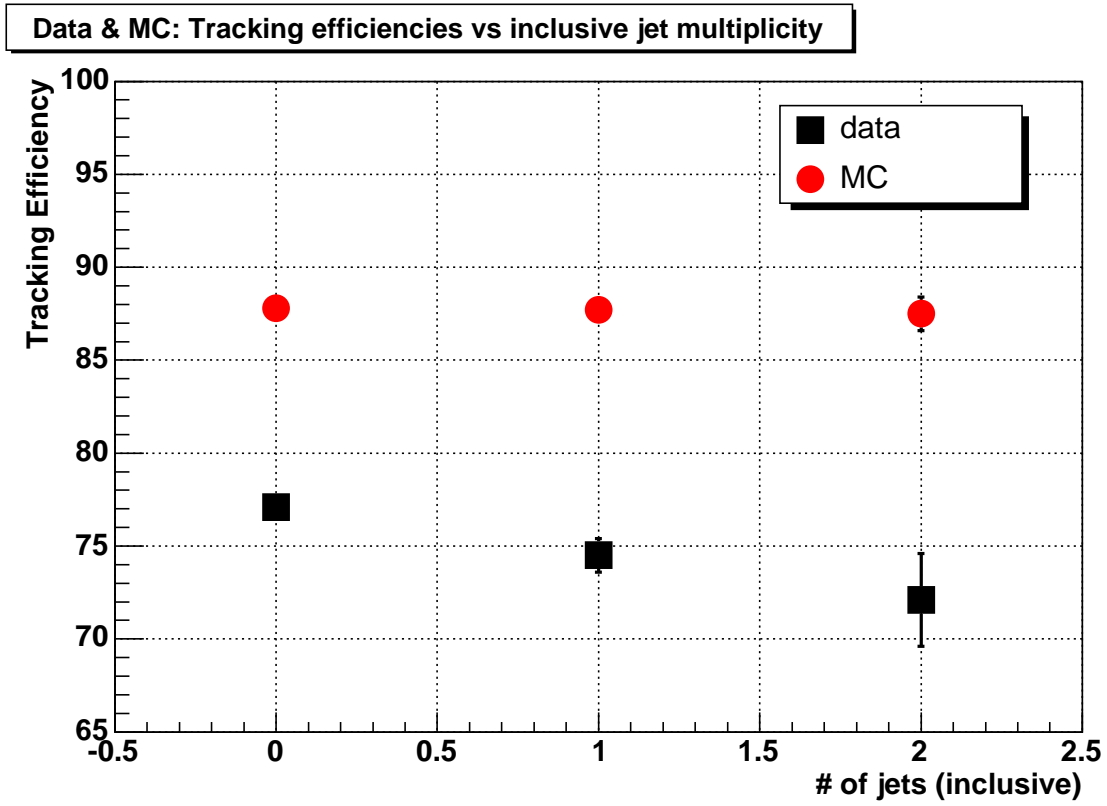


Figure 59. Average object based tracking efficiencies in data and MC versus inclusive jet multiplicity.

Jet multiplicity	Data Efficiency	Systematic Uncertainty
≥ 0	77.1%	$\pm 0.3\%$
≥ 1	74.5%	$\pm 0.9\%$
≥ 2	72.1%	$\pm 2.5\%$
≥ 3	72.1%	$\pm 3.5\%$
≥ 4	72.1%	$\pm 5.6\%$
≥ 5	72.1%	$\pm 7.9\%$

TABLE X

OBJECT BASED TRACKING EFFICIENCIES WITH SYSTEMATIC ERRORS.

6.5.1.4 Acceptance

We use the ALPGEN MC samples to estimate the acceptances for different jet multiplicities

¹. The numerator for the n -jet acceptance contains the number of events satisfying the following requirements:

- Primary vertex cut: $|PVZ| < 60$ cm
- Electron cuts: $p_T > 25$ GeV and $|\eta| < 1.1$
- Diem invariant mass cut: $75 \text{ GeV} < M_{ee} < 105 \text{ GeV}$
- Particle level jet cut: n jets with $p_T > 20$ GeV and $|\eta| < 2.5$

The denominator for the n -jet acceptance contains the number of events satisfying the following requirements:

¹The $Z+3$ jet sample is used for jet multiplicities of 3, 4, and 5.

Jet multiplicity	Acceptance
≥ 0	$21.4\% \pm 0.1\%$
≥ 1	$25.1\% \pm 0.2\%$
≥ 2	$25.4\% \pm 0.2\%$
≥ 3	$27.4\% \pm 0.3\%$
≥ 4	$28.5\% \pm 0.7\%$
≥ 5	$30.3\% \pm 1.9\%$

TABLE XI

ACCEPTANCES WITH STATISTICAL ERRORS FOR DIFFERENT JET MULTIPLICITIES.

- Generator level diem invariant mass cut: $75 \text{ GeV} < M_{ee} < 105 \text{ GeV}$
- Particle level jet cut: n jets with $p_T > 20 \text{ GeV}$ and $|\eta| < 2.5$

No additional Z p_T correction is needed since the Z p_T distributions between data and ALPGEN MC agree well (see Chapter 6.3.2). Table XI summarizes the acceptances for different jet multiplicities.

6.5.1.5 Jet Reconstruction and Identification Efficiency

To estimate the jet reco/ID efficiency in data we use the “ Z p_T balance” method to measure the scaling factor needed to adjust the MC jet reco/ID efficiency to data, and then use MC to measure the “straight” reco/ID jet efficiency with respect to the particle level jets (63). The Z p_T balance method relies on the recoil of a jet against the Z boson. We select events with Z candidates and search for a recoiling calorimeter jet opposite in Φ . We measure the “efficiency” of finding a recoiling jet as a function of the Z p_T in data and MC. The ratio of these efficiencies

in data and MC gives us the scaling factor that we apply to the MC in order to make it agree with the data jet reco/ID efficiency. We then measure the straight jet reco/ID efficiency in MC by matching particle level jets with calorimeter jets within a search cone of $\Delta R = 0.4$. The jet reco/ID efficiency is plotted versus MC particle jet p_T . The p_T values of the particle jets are smeared with the data energy resolutions (see Chapter 6.1.2.1). Figure 60 shows the data jet reconstruction efficiencies for different regions in the calorimeter.

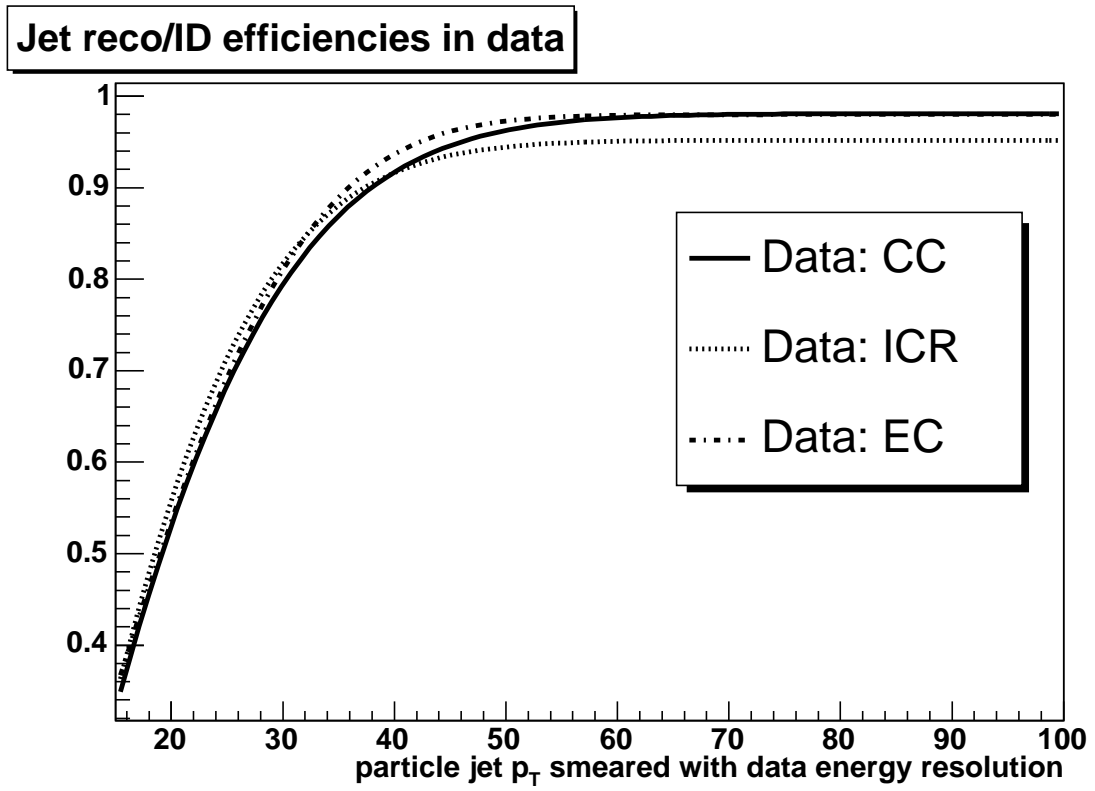


Figure 60. Jet reco/ID efficiencies in data. CC = $-0.7 < |\eta_{det}| < 0.7$, ICR = $0.7 < |\eta_{det}| < 1.5$, EC = $1.5 < |\eta_{det}| < 2.5$.

6.5.2 Cross section calculation

6.5.2.1 Unsmearing

In order to determine particle level cross sections, we unsmear the measured data jet multiplicities. We use a special $Z+1$ jet PYTHIA MC sample by choosing PYTHIA 2-to-2 subprocesses 15 and 30¹ with a parton p_T cut-off of 8 GeV and by applying vertex smearing. This sample only contains particle level jets (no detector simulation). We then apply the full data resolution smearing to the particle jet p_T as well as the data jet reco/ID efficiencies. Comparing the inclusive jet multiplicity for this MC sample with the one in data gives an idea of how well the MC describes the data (Figure 61). There is increasing disagreement at higher jet multiplicities, since PYTHIA does not include higher order contributions at the hard scatter level. We correct for this discrepancy by taking the ratio between data and MC for each inclusive jet multiplicity (Figure 62) and then applying correction factors (per event) based on the absolute values of these ratios. After this additional step we again compare the inclusive jet multiplicity spectrum in MC with the one in data and find much better agreement (Figure 63). We use this corrected MC sample to derive the final unsmearing and jet reco/ID coefficients. Figure 64 - Figure 75 compare jet p_T and η distributions between the data and MC sample. We evaluate agreement between the data and MC distributions by quoting Kolmogorov-Smirnov probabilities (64).

To calculate the coefficients we first take the inclusive jet multiplicity histogram for particle

¹ $f_i \bar{f}_i \rightarrow gZ^0$ and $f_i g \rightarrow f_i Z^0$

Jet multiplicity	Unsmearing and jet reco/ID coefficient
≥ 1	1.10 $^{+0.08}_{-0.06}$
≥ 2	1.26 $^{+0.18}_{-0.16}$
≥ 3	1.50 $^{+0.25}_{-0.24}$
≥ 4	1.90 $^{+0.52}_{-0.39}$
≥ 5	4.00 $^{+3.42}_{-1.13}$

TABLE XII

UNSMEARING AND JET RECO/ID COEFFICIENTS WITH SYSTEMATIC UNCERTAINTY DUE TO RESOLUTION AND JET RECO/ID EFFICIENCY.

level jets with $p_T > 20$ GeV and $|\eta_{physics}| < 2.5$ and divide it by the inclusive jet multiplicity histogram for particle level jets with smeared $p_T > 20$ GeV and $|\eta_{physics}| < 2.5$ (plus applying jet reco/ID efficiencies). The absolute values of these ratios yield the unsmearing and jet reco/ID coefficients which can be applied as multiplicative factors to the measured jet multiplicities in data. Figure 76 shows the numerator and denominator jet multiplicity histograms, as well as the ratio when applying jet smearing and jet reco/ID efficiencies in the denominator. For comparison Figure 77 shows the same distributions without applying jet reco/ID efficiencies, i.e. applying only jet smearing.

We use the statistical error of each unsmearing and jet reco/ID coefficient as a statistical error to the final cross sections (see Chapter 6.6.7). Table XII summarizes all coefficients.

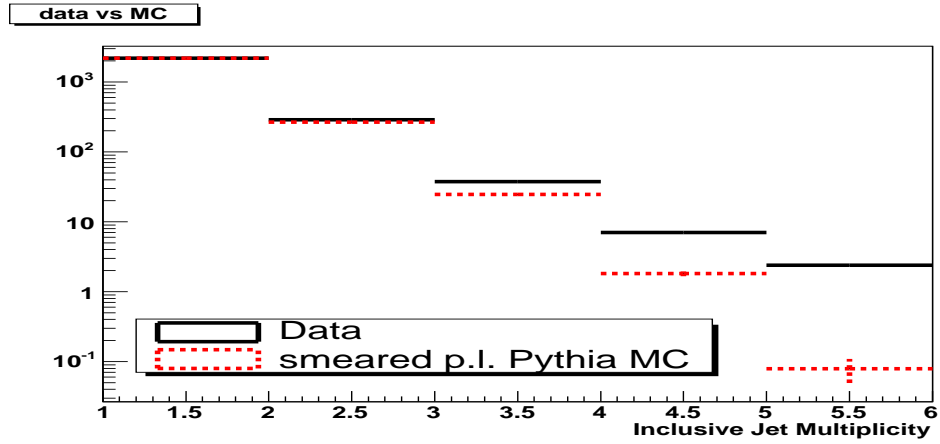


Figure 61. Comparing inclusive jet multiplicities between data and particle level MC (applying data resolution smearing and data jet reco/ID efficiencies). The distributions are normalized with respect to the first bin.

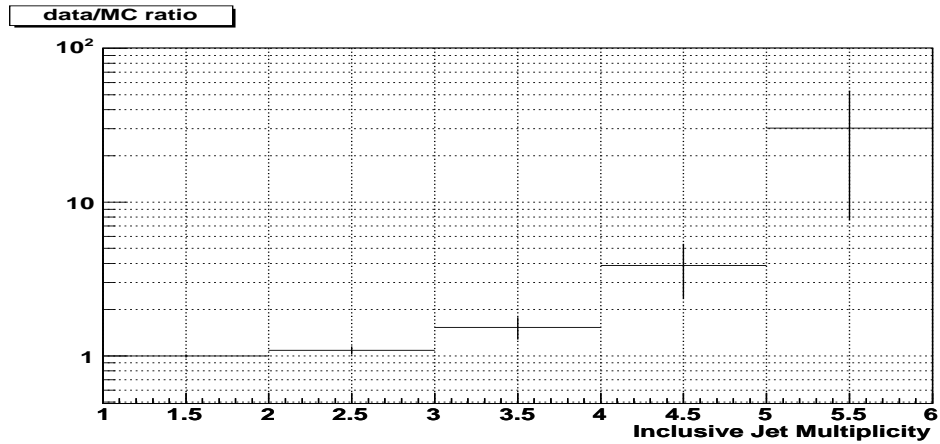


Figure 62. Ratio of MC (with smearing and jet reco/ID efficiencies) inclusive jet multiplicities and data inclusive jet multiplicities.

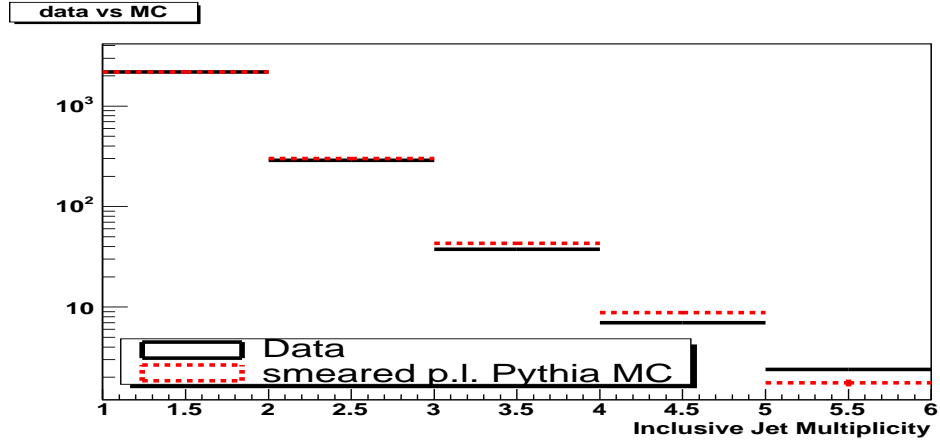


Figure 63. Comparing inclusive jet multiplicities between data and particle level MC (after applying correction factors). The distributions are normalized with respect to the first bin.

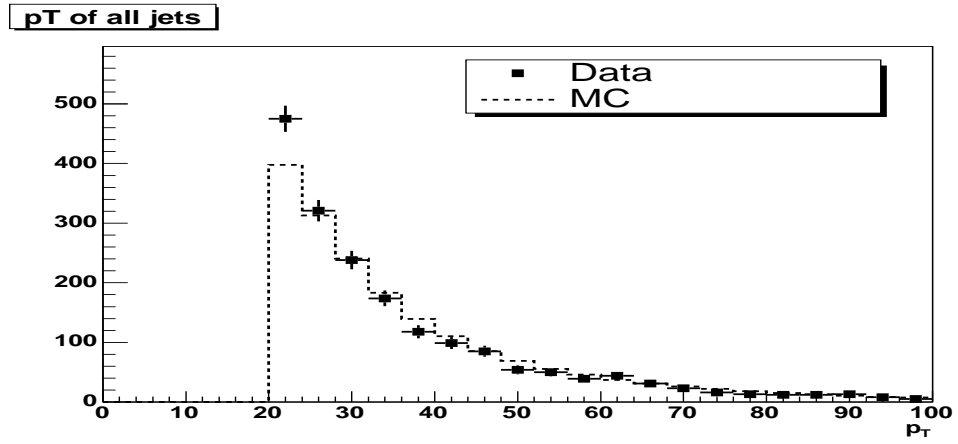


Figure 64. Comparing jet p_T for all jets between data and particle level MC (with data resolution smearing and jet reco/ID efficiencies applied).

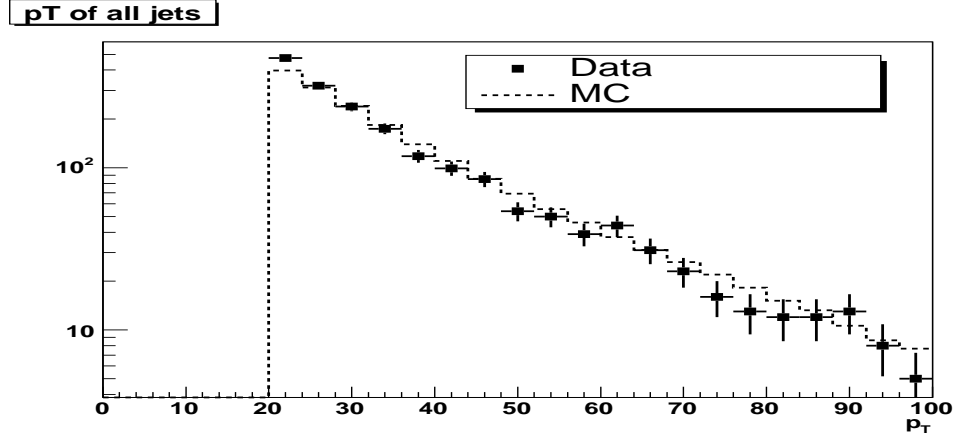


Figure 65. Comparing jet p_T for all jets between data and particle level MC (with data resolution smearing and jet reco/ID efficiencies applied).

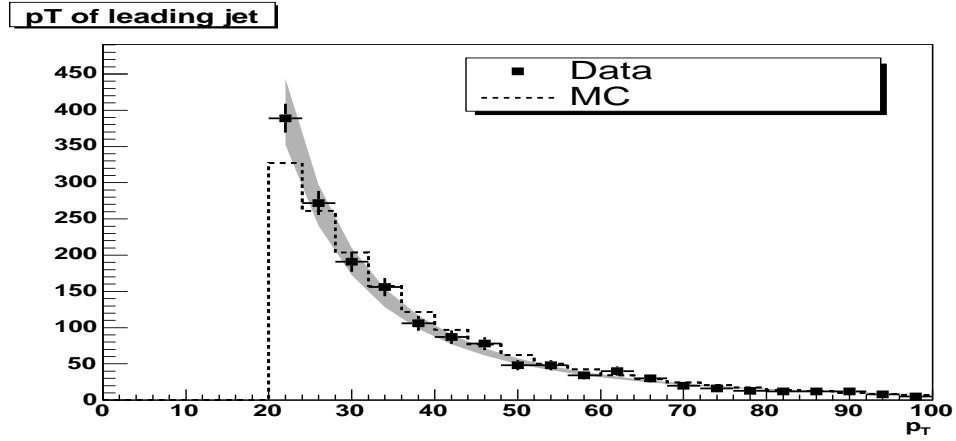


Figure 66. Comparing jet p_T for leading jets between data and particle level MC (with data resolution smearing and jet reco/ID efficiencies applied). Kolmogorov-Smirnov Probability = 0.13. The gray band shows the uncertainty due to the jet energy scale.

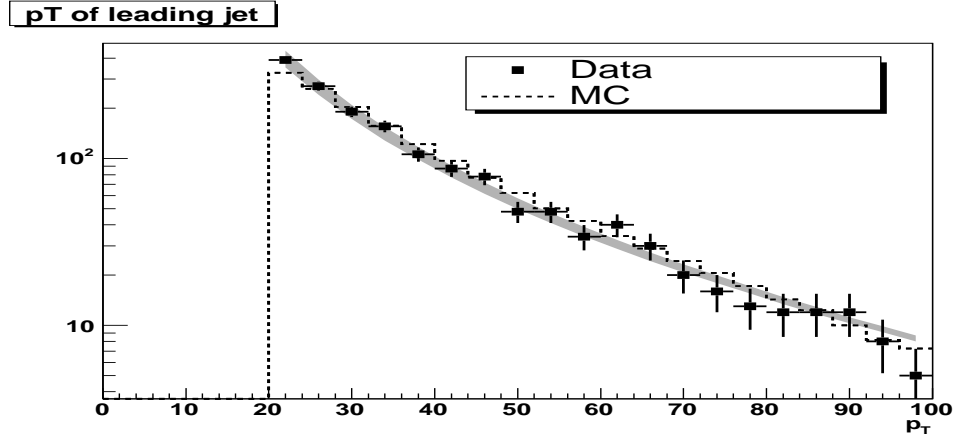


Figure 67. Comparing jet p_T for leading jets between data and particle level MC (with data resolution smearing and jet reco/ID efficiencies applied). Kolmogorov-Smirnov Probability = 0.13. The gray band shows the uncertainty due to the jet energy scale.

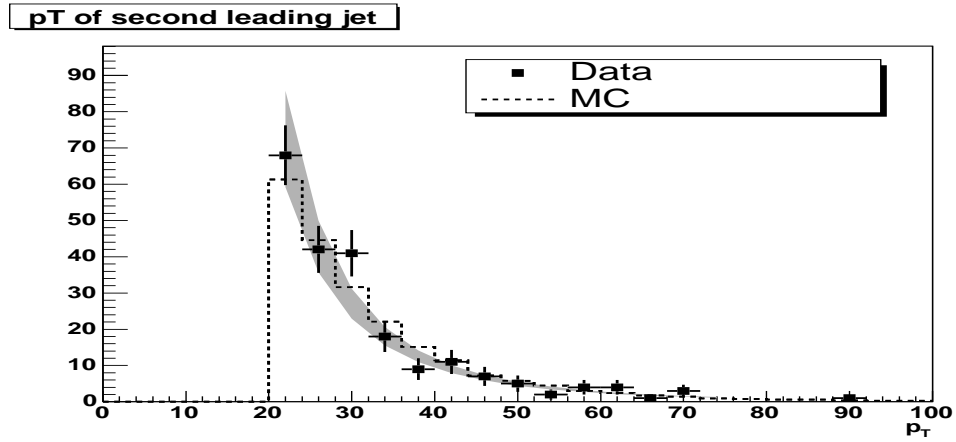


Figure 68. Comparing jet p_T for second leading jets between data and particle level MC (with data resolution smearing and jet reco/ID efficiencies applied). Kolmogorov-Smirnov Probability = 0.56. The gray band shows the uncertainty due to the jet energy scale.

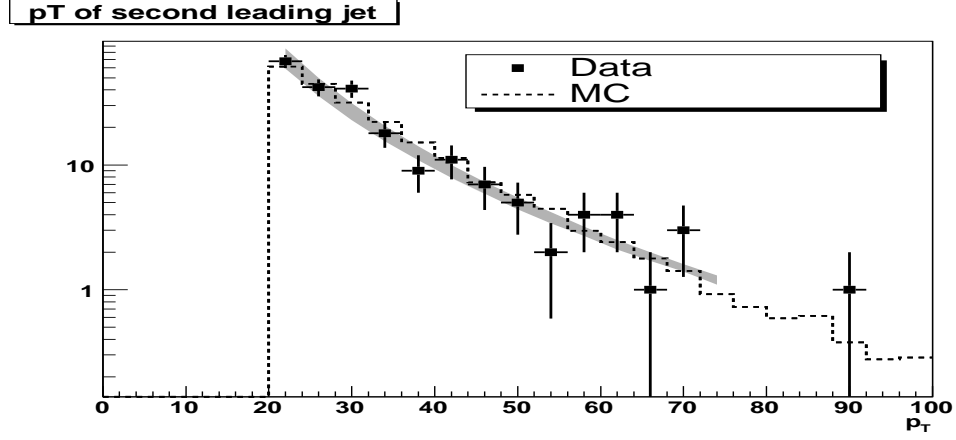


Figure 69. Comparing jet p_T for second leading jets between data and particle level MC (with data resolution smearing and jet reco/ID efficiencies applied). Kolmogorov-Smirnov Probability = 0.56. The gray band shows the uncertainty due to the jet energy scale.

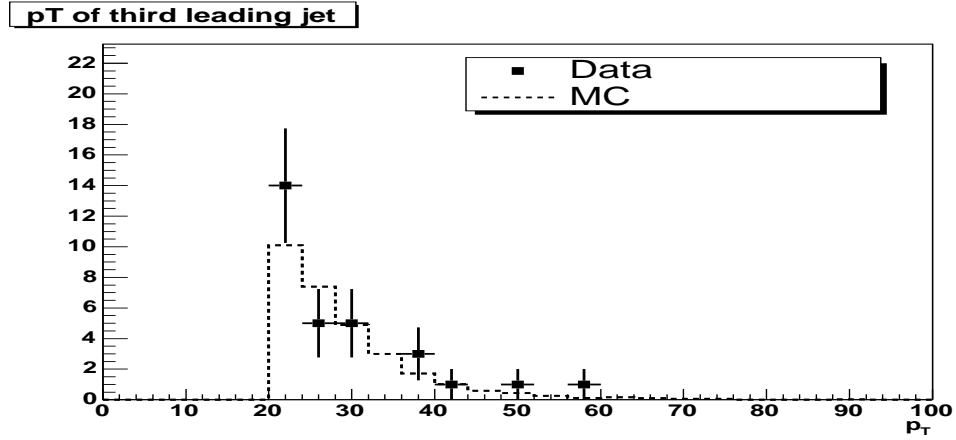


Figure 70. Comparing jet p_T for third leading jets between data and particle level MC (with data resolution smearing and jet reco/ID efficiencies applied). Kolmogorov-Smirnov Probability = 0.57.

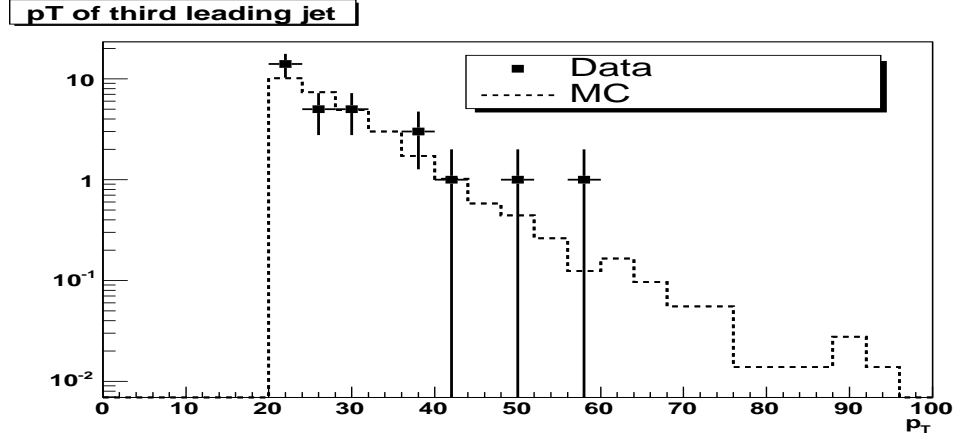


Figure 71. Comparing jet p_T for third leading jets between data and particle level MC (with data resolution smearing and jet reco/ID efficiencies applied). Kolmogorov-Smirnov Probability = 0.57.

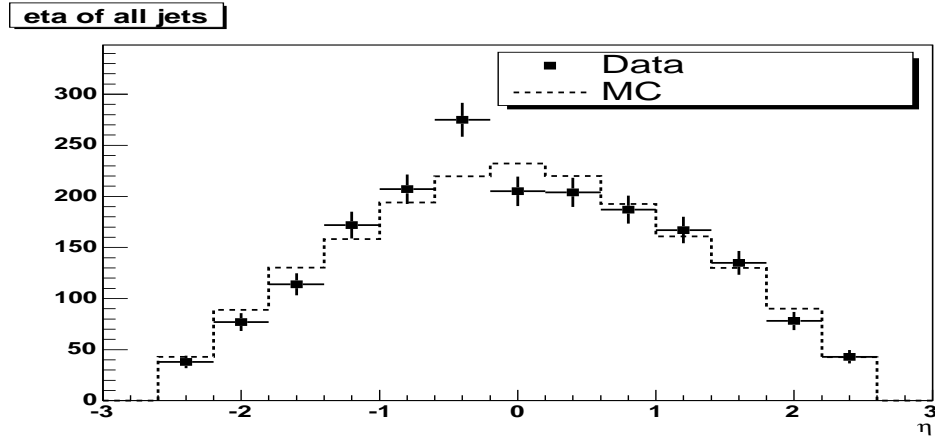


Figure 72. Comparing jet η for all jets between data and particle level MC (with data resolution smearing and jet reco/ID efficiencies applied).

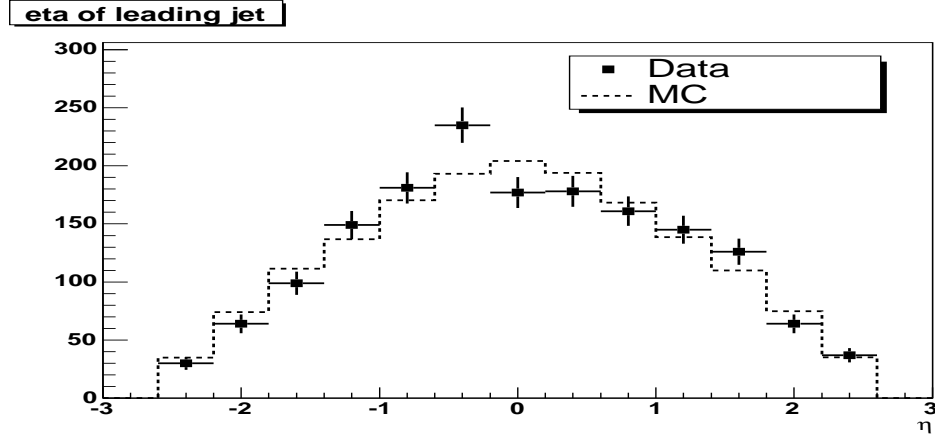


Figure 73. Comparing jet η for leading jets between data and particle level MC (with data resolution smearing and jet reco/ID efficiencies applied). Kolmogorov-Smirnov Probability = 0.70.

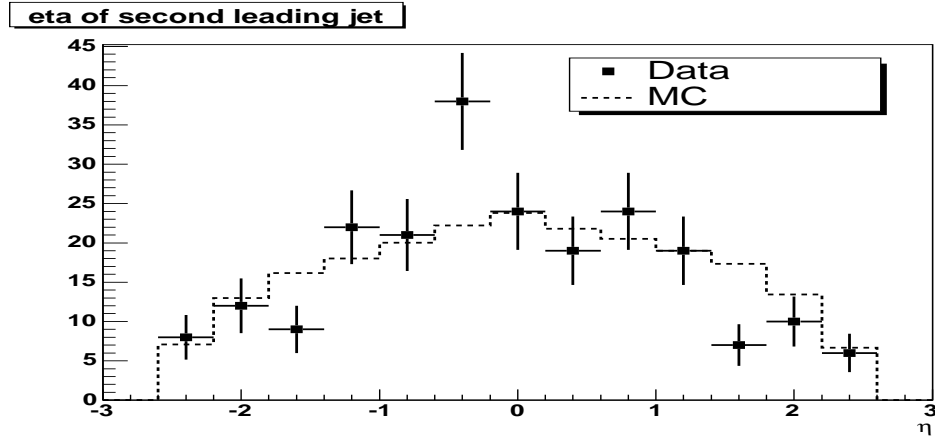


Figure 74. Comparing jet η for second leading jets between data and particle level MC (with data resolution smearing and jet reco/ID efficiencies applied). Kolmogorov-Smirnov Probability = 0.30.

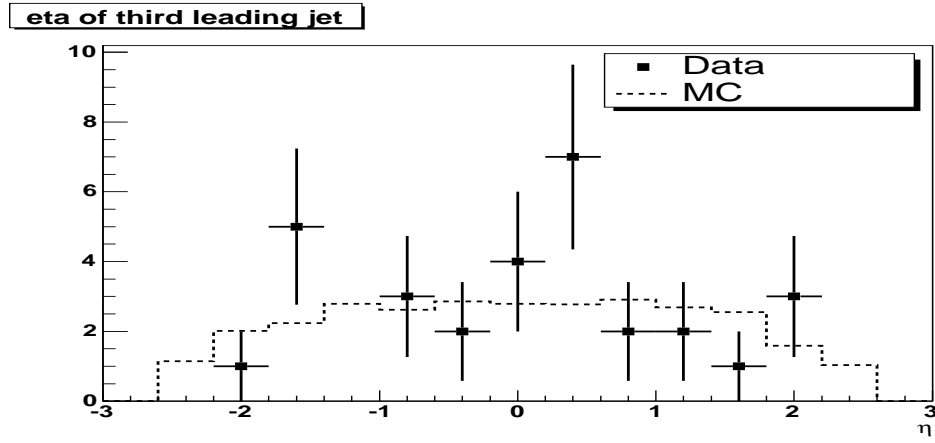


Figure 75. Comparing jet η for third leading jets between data and particle level MC (with data resolution smearing and jet reco/ID efficiencies applied). Kolmogorov-Smirnov Probability = 0.93.

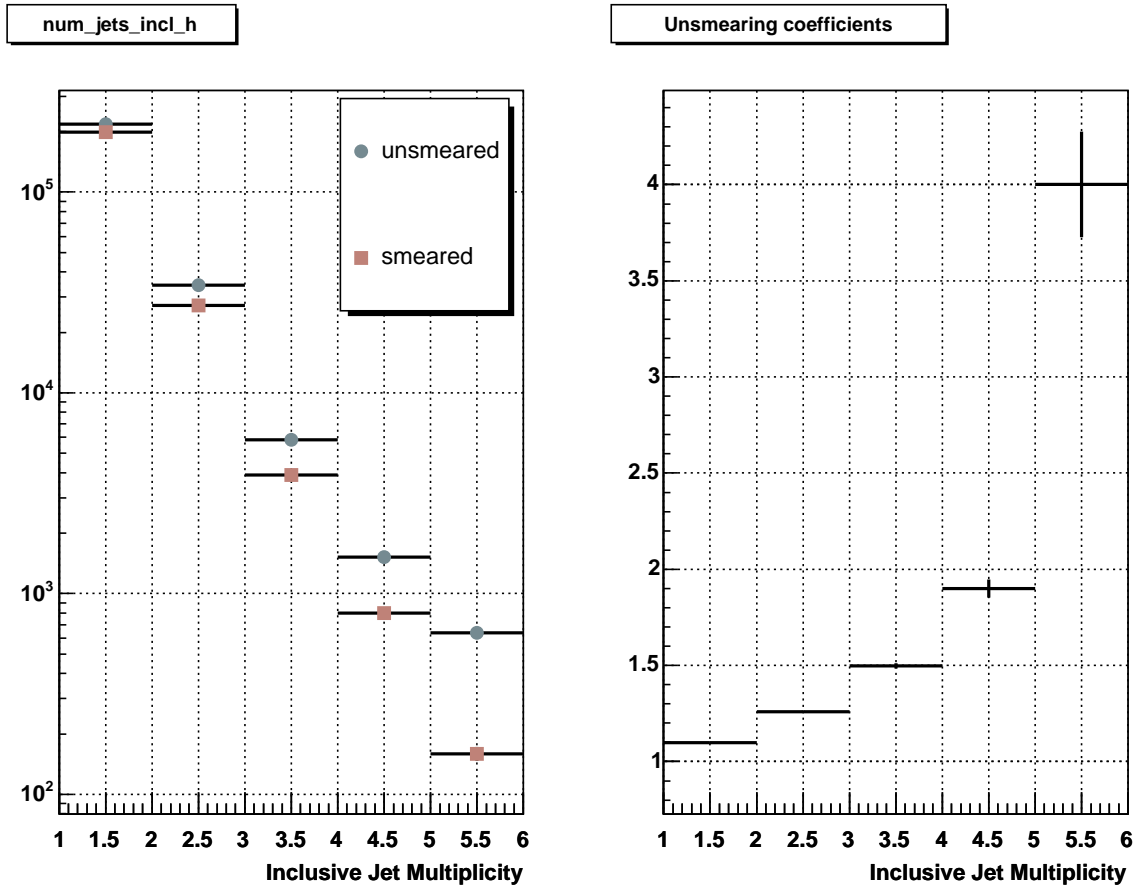


Figure 76. Unsmearing and jet reco/ID particle jet multiplicities (left) and coefficients (right).

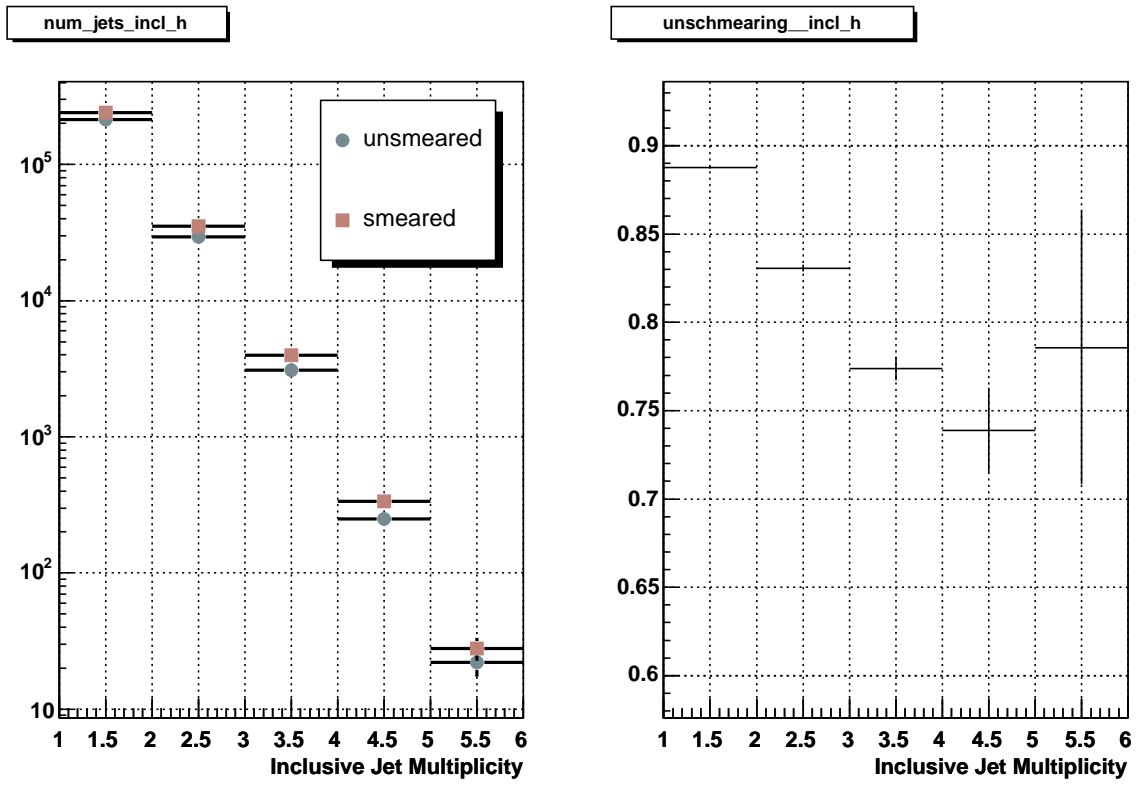


Figure 77. Unsmearing jet multiplicities (left) and coefficients (right) without applying jet reco/ID efficiencies.

6.5.2.2 Electron-Jet-Overlap Correction

Using the tag-and-probe method outlined in Chapter 6.4.1.2, we plot the ΔR distribution between probe tracks and reconstructed jets that pass all jet quality cuts except for the electron-jet-overlap cut in data and MC (Figure 78 and Figure 79).

We see an excess of entries at ΔR values of 0 and π due to fake jets (i.e. originated from the electron energy deposits) which survived the jet quality cuts. Therefore we reject all jets that are near the two electrons within $\Delta R=0.4$. Figure 80 shows the same distribution as in Figure 78 after adding the electron-jet-overlap cut. For comparison Figure 81 shows the ΔR between generated electrons and partons in data and MC.

An additional correction needs to be derived in order to account for the real jets that are removed by the electron-jet-overlap cut. Using the same MC sample as for the unsmearing studies (see Chapter 6.5.2.1) we estimate the correction factors due to the electron-jet-overlap by taking the ratio of the inclusive parton multiplicity distribution for all partons with $p_T > 20$ GeV and $|\eta| < 2.5$ and the inclusive parton multiplicity distribution for partons that are outside of the ΔR cone with respect to the electrons from the Z .

We derive correction factors using ΔR cones of size 0.4 and 0.7 and take the middle value as the final correction factors. This is done in order to account for the position resolution between partons and calorimeter jets (see Figure 82). Additionally we apply a linear fit to the final values in order to compensate for statistical fluctuations.

Table XIII summarizes the electron-jet-overlap correction factors for different jet multiplicity

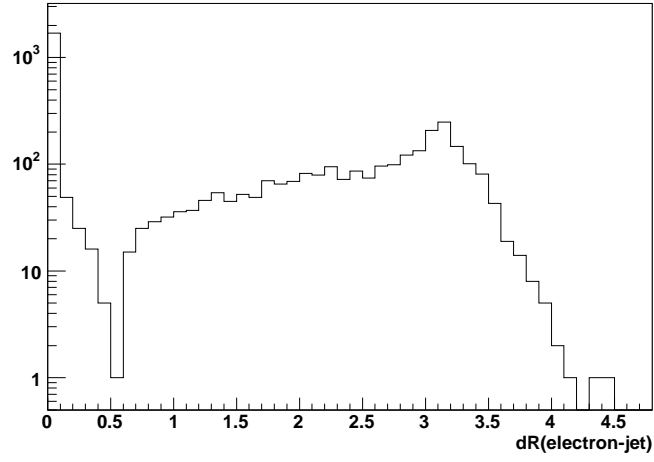


Figure 78. ΔR between probe-tracks and good jets in data (without electron-jet-overlap cut).

samples. We apply these corrections as multiplicative factors to the measured jet multiplicities in data.

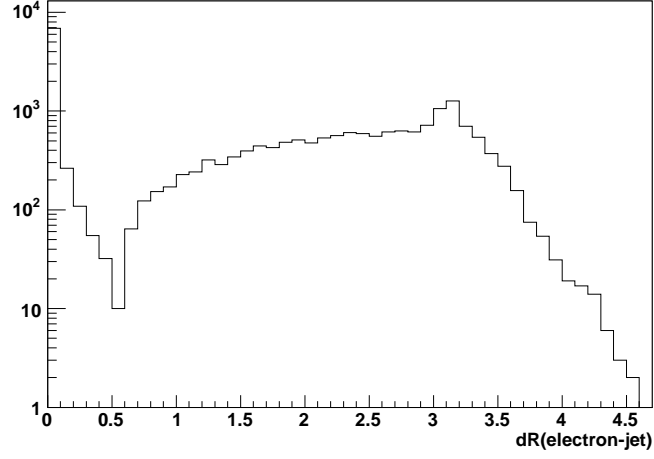


Figure 79. ΔR between probe-tracks and good jets using PYTHIA MC (without electron-jet-overlap cut).

Jet Multiplicity	Electron-Jet-Overlap Coefficient
≥ 1	1.059 ± 0.028
≥ 2	1.075 ± 0.041
≥ 3	1.092 ± 0.054
≥ 4	1.109 ± 0.067
≥ 5	1.125 ± 0.077

TABLE XIII

ELECTRON-JET-OVERLAP COEFFICIENTS WITH SYSTEMATIC UNCERTAINTIES.

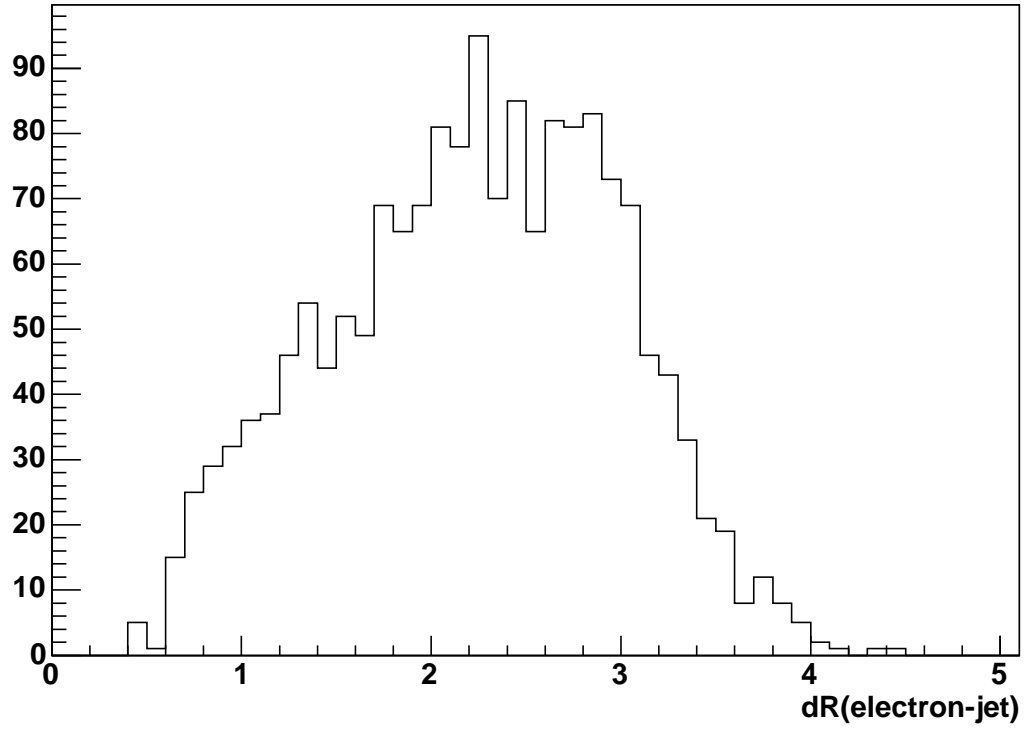


Figure 80. ΔR between probe-tracks and good jets in data (after the electron-jet-overlap cut was applied).

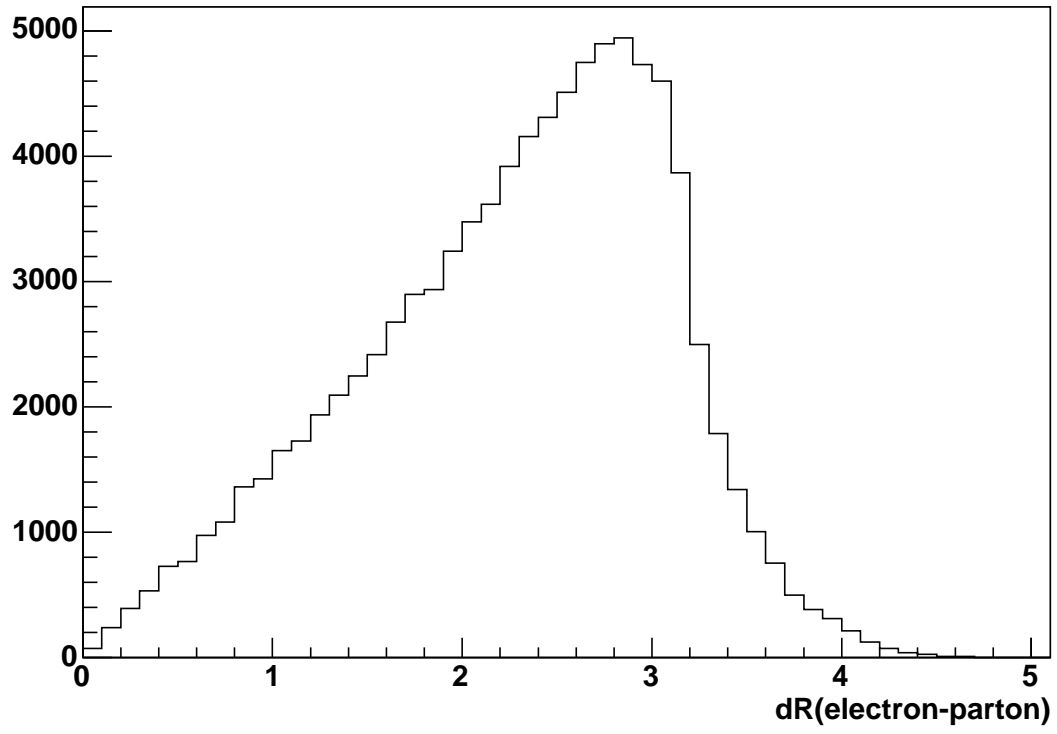


Figure 81. ΔR between generated electrons ($p_T > 25$ GeV, $|\eta| < 1.1$) and partons ($p_T > 20$ GeV, $|\eta| < 2.5$).

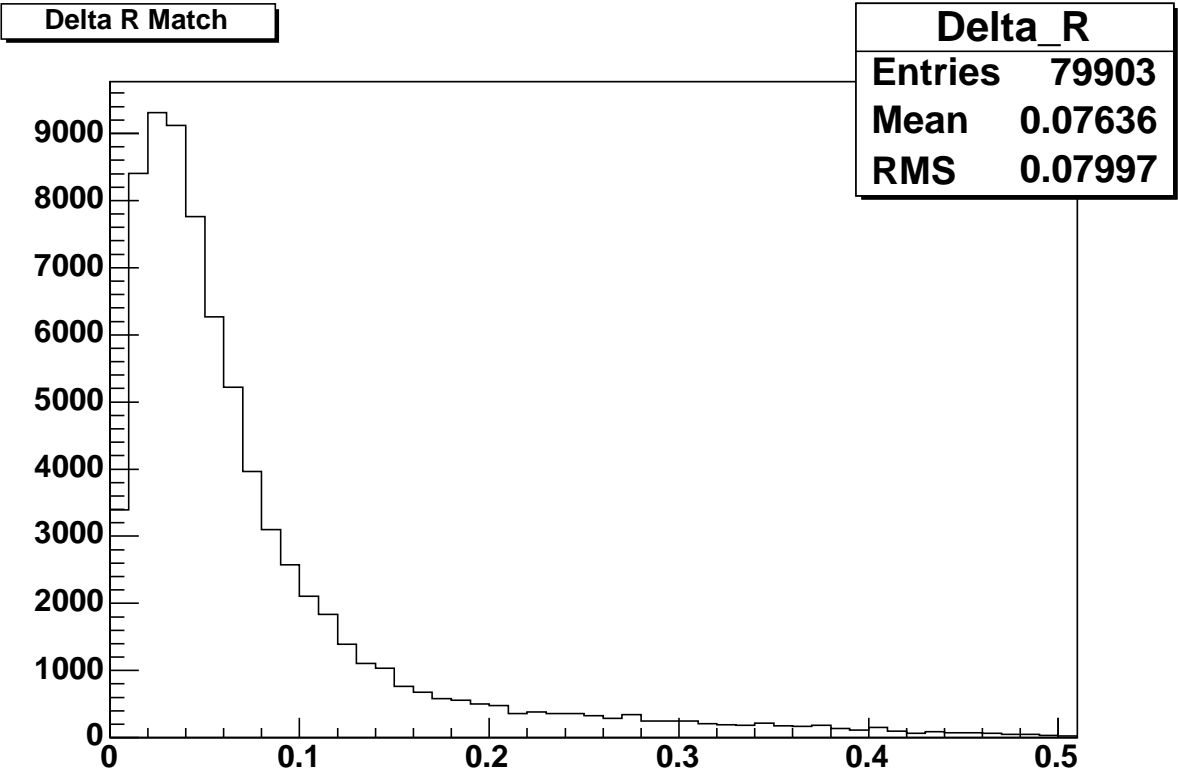


Figure 82. ΔR between partons and matched calorimeter jets ($p_T > 20$ GeV, $|\eta| < 2.5$).

Jet Multiplicity	Total number of entries	Signal	Background
≥ 1	2,625.2	2,550.7 (52.5)	74.6
≥ 2	404.5	392.0 (8.1)	12.5
≥ 3	64.7	61.6 (1.3)	3.1
≥ 4	14.7	14.7 (-)	0
≥ 5	10.8	10.8 (-)	0

TABLE XIV

NUMBER OF SIGNAL EVENTS (DRELL-YAN IN PARENTHESIS) AND NUMBER OF BACKGROUND EVENTS (QCD) FOR DIFFERENT JET MULTIPLICITIES. NUMBERS ARE CORRECTED FOR TRIGGER, EM AND TRACKING INEFFICIENCIES (AFTER APPLYING THE UNSMEARING, JET RECO/ID AND ELECTRON-JET-OVERLAP CORRECTIONS).

6.5.2.3 Cross sections

Figure 83 through Figure 87, show the diem invariant mass distributions for jet multiplicities ≥ 1 to ≥ 5 which we use to extract the number of signal and background events for the cross section calculation (corrected for trigger, EM and tracking inefficiencies). For jet multiplicities of ≥ 1 and ≥ 2 , we follow the same technique as outlined in Chapter 6.4.2. For jet multiplicities of ≥ 3 we use sidebands to estimate the background. For higher jet multiplicities there is not enough statistics to estimate any background.

Table XIV summarizes the number of signal and background events for each jet multiplicity. The fully corrected and unsmeared cross sections versus jet multiplicities (with jet $p_T > 20$ GeV, $|\eta| < 2.5$) are shown in Figure 88 with statistical errors.

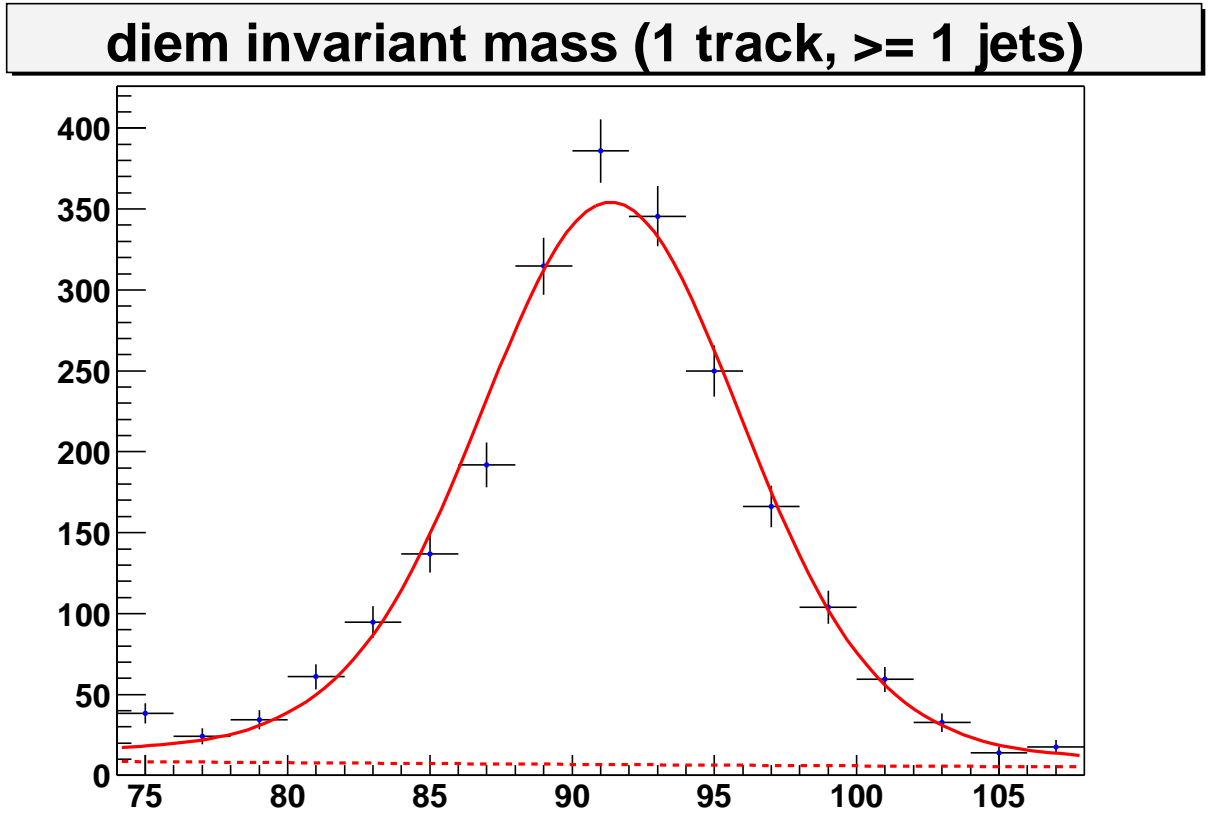


Figure 83. Diem invariant mass distribution for the $Z/\gamma^* \rightarrow e^+e^- + \geq 1$ jet sample. The solid line shows a Gaussian plus Breit-Wigner fit to the Z peak. The dashed line shows an exponential fit to the QCD and Drell-Yan contribution.

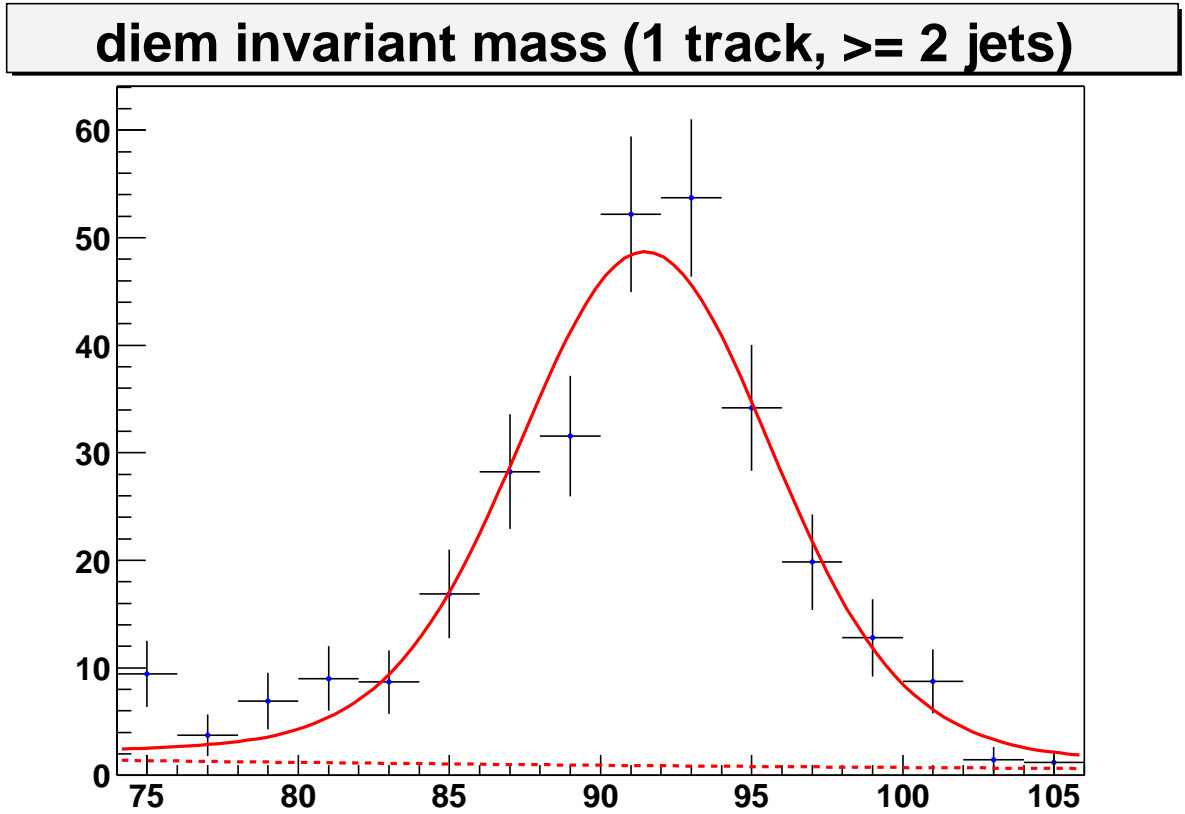


Figure 84. Diem invariant mass distribution for the $Z/\gamma^* \rightarrow e^+e^- + \geq 2$ jet sample. The solid line shows a Gaussian plus Breit-Wigner fit to the Z peak. The dashed line shows an exponential fit to the QCD and Drell-Yan contribution.

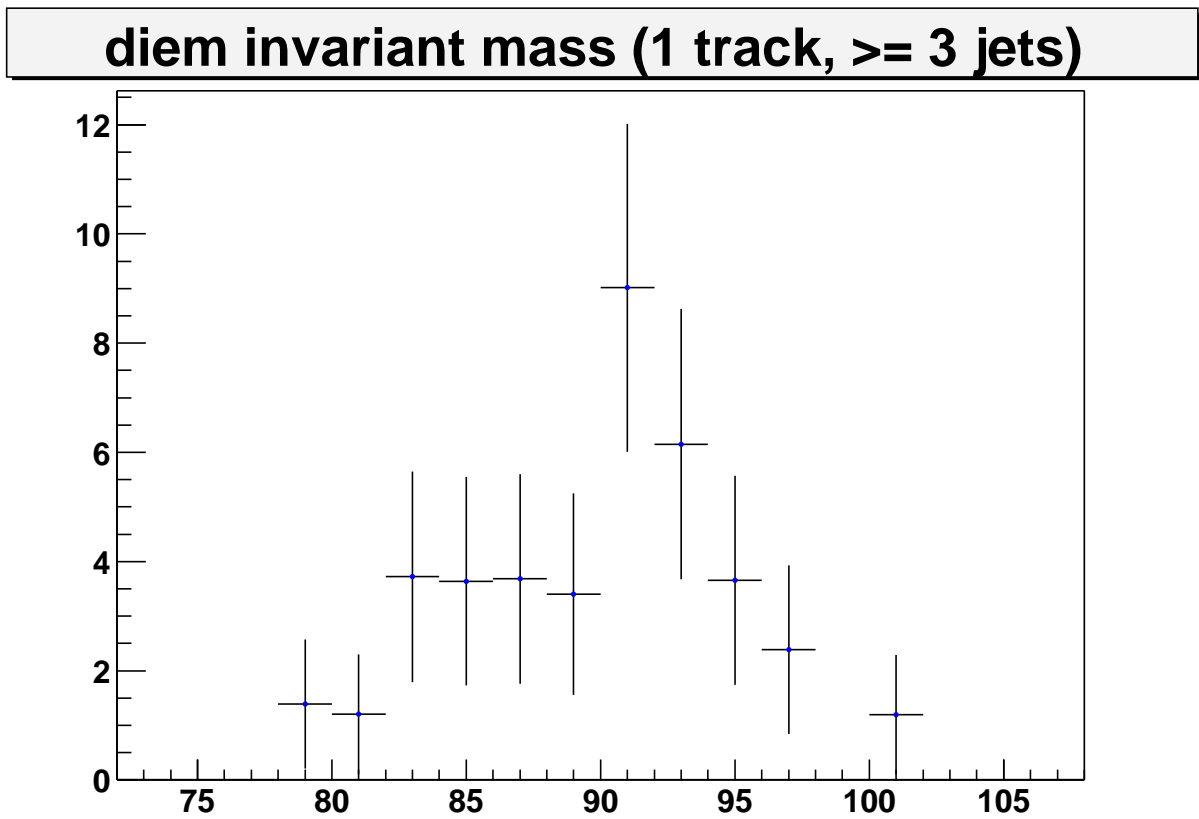


Figure 85. Diem invariant mass distribution for the $Z/\gamma^* \rightarrow e^+e^- + \geq 3$ jet sample.

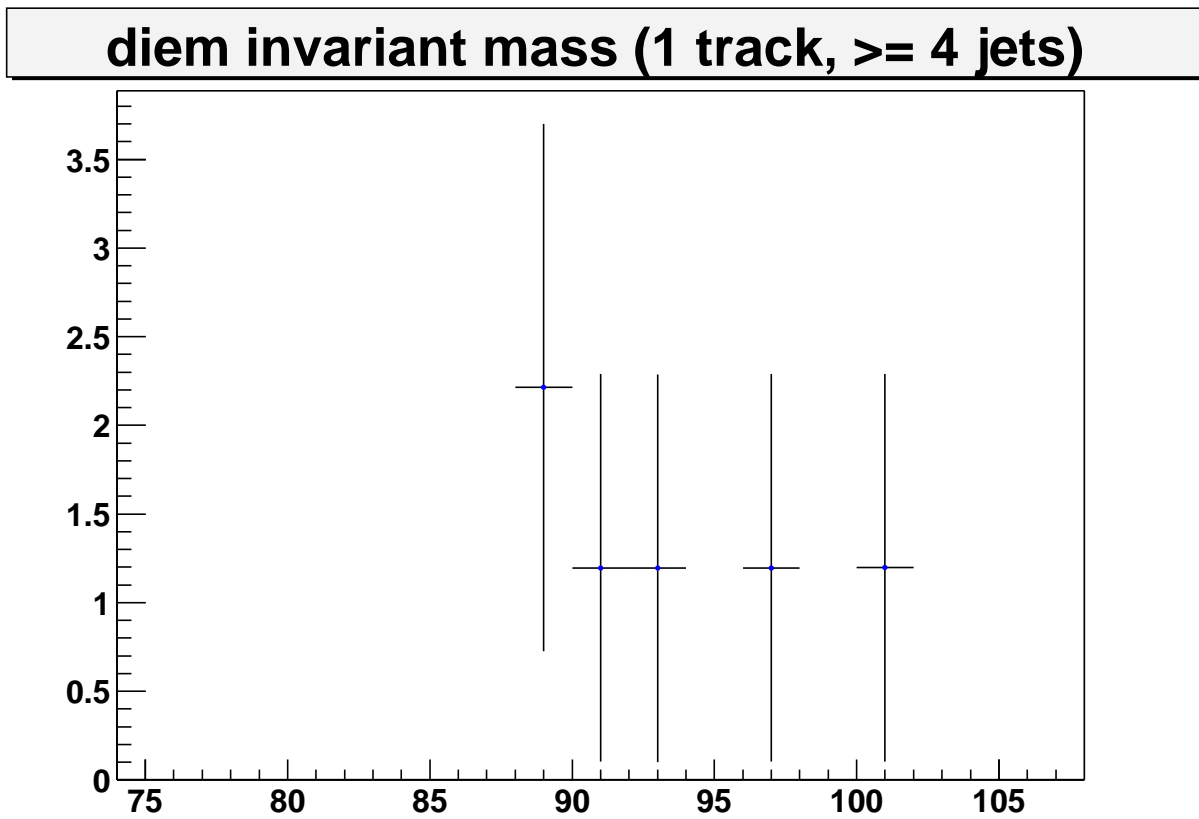


Figure 86. Diem invariant mass distribution for the $Z/\gamma^* \rightarrow e^+e^- + \geq 4$ jet sample.

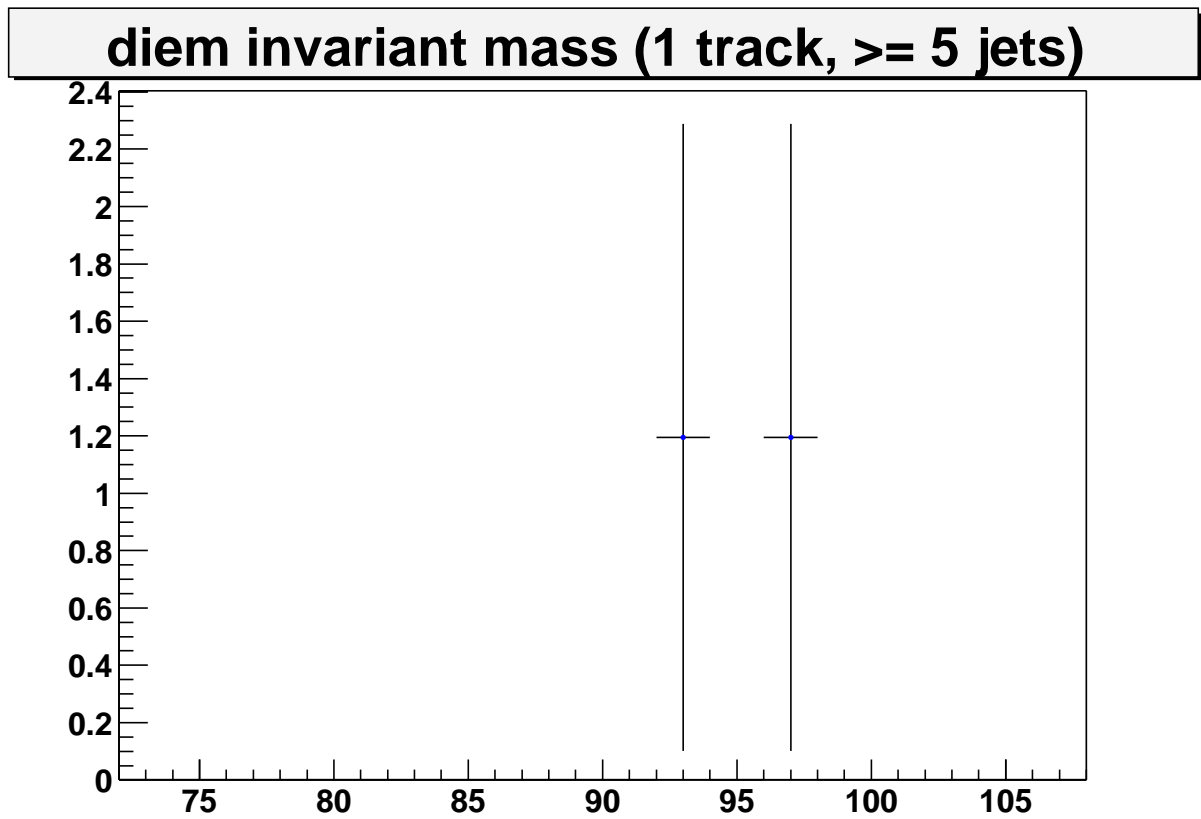


Figure 87. Diem invariant mass distribution for the $Z/\gamma^* \rightarrow e^+e^- + \geq 5$ jet sample.

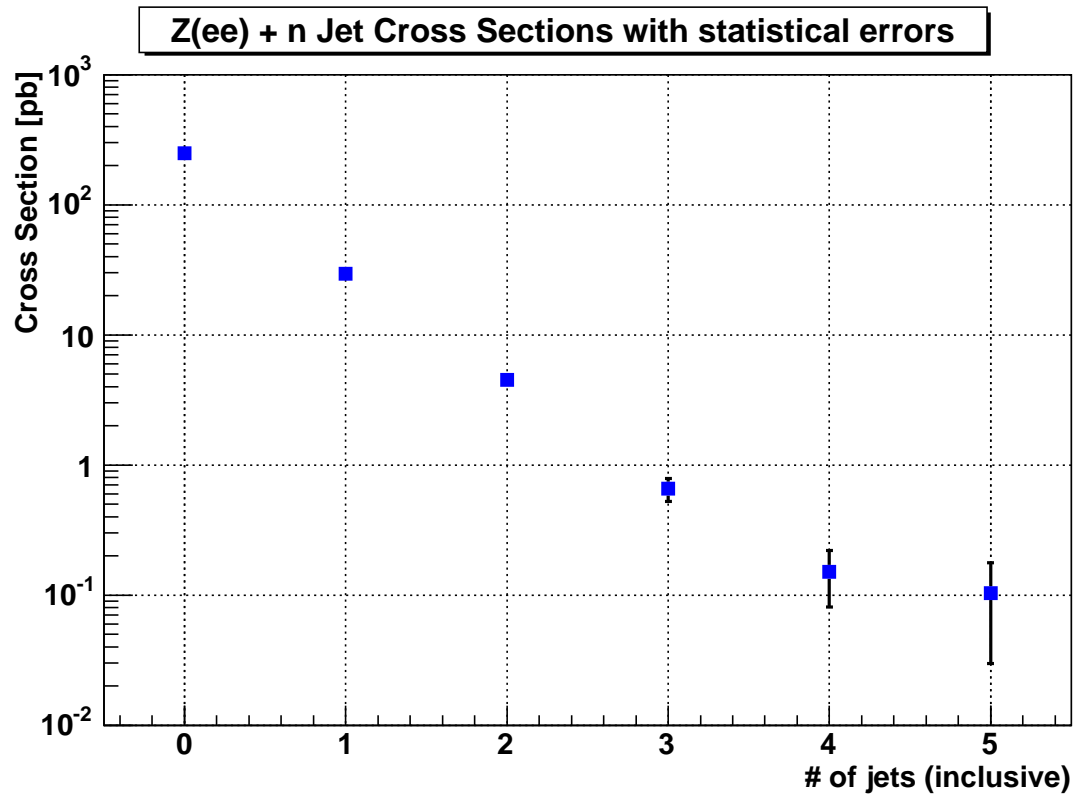


Figure 88. Cross sections for inclusive jet multiplicities with statistical errors.

Jet multiplicity	Cross Section	JES Errors
≥ 1	29.6 pb	± 2.9 pb
≥ 2	4.50 pb	± 0.83 pb
≥ 3	0.655 pb	± 0.185 pb
≥ 4	0.151 pb	± 0.057 pb
≥ 5	0.1035 pb	± 0.0520 pb

TABLE XV

FINAL CROSS SECTIONS WITH JES ERRORS.

6.6 Systematics

6.6.1 Jet Energy Scale Systematic Error

We estimate the error due to the jet energy scale (version 5.3) by moving the energy scale correction up and down by 1σ (combined systematic and statistical JES uncertainty) and subsequently rederiving the diem invariant mass histograms (corrected for trigger, EM reco/ID, and EM-Track matching inefficiencies) to get the number of corrected signal events for different jet multiplicities. We then recalculate the cross sections to estimate the JES error. Figure 89 shows the effect of the JES error on the corrected jet multiplicity distribution.

We fit the percentage errors for each jet multiplicity linearly to get a smooth curve and to be independent from statistical fluctuations. The final JES error is the maximum of the actual data error and the fit error. Table XV summarizes the JES errors. The JES errors are the dominant errors in this analysis.

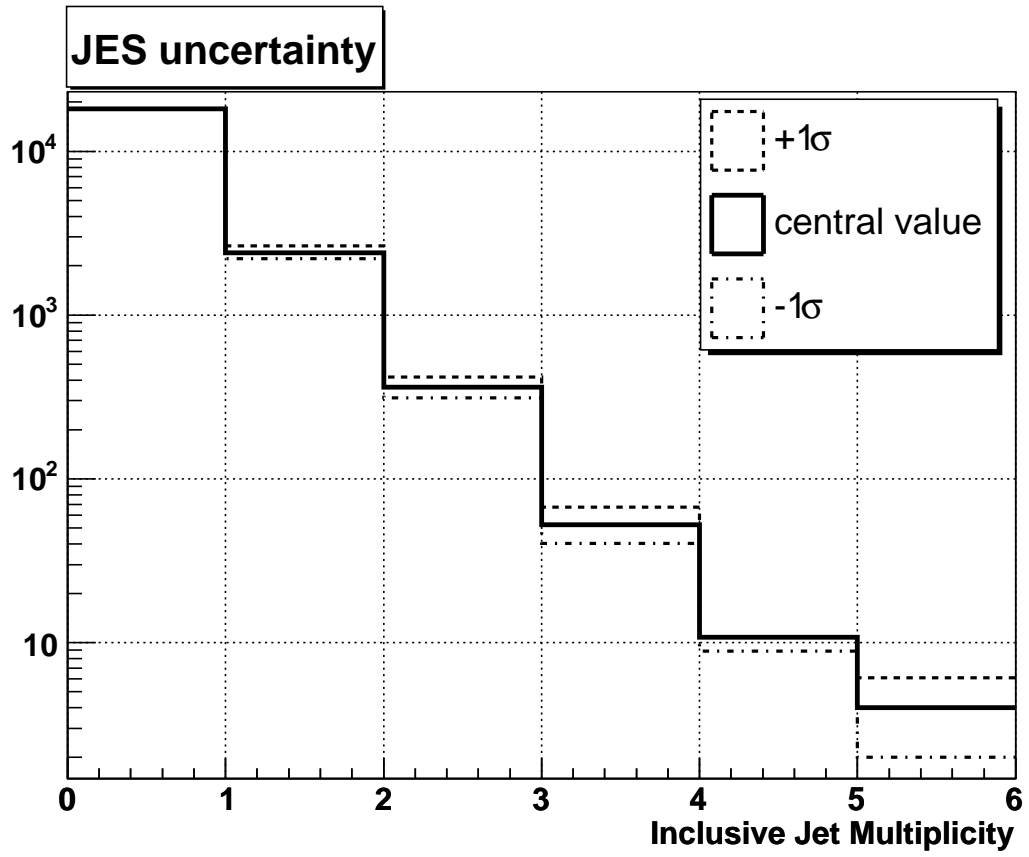


Figure 89. $\pm 1\sigma$ fluctuation of the jet energy scale (JES 5.3)

6.6.2 Systematic Error of Cross Section Unfolding

- A detailed description of the jet reco/ID efficiency errors can be found in (63). Figure 90, Figure 91 and Figure 92 show the jet reco/ID efficiencies with error bands. The errors are due to the statistical uncertainty of the scale factor and straight efficiency, the missing E_T cut, and differences between CKKW and PYTHIA MC generators. To estimate the jet reco/ID uncertainty we rederive the unsmearing and jet reco/ID correction factors using the upper and lower error bands of the jet reco/ID efficiencies.

Figure 93 shows the scale factor used in this analysis overlaid with the average scale factor determined by the Top group. Both curves agree within the error bands.

As a cross check we perform a closure test where we compare the “efficiency” of finding a recoiling jet as a function of Z p_T in data and particle level MC (Figure 94). Both the data and MC distributions have a jet p_T cut of 8 GeV applied. In addition, the MC particle jets are smeared with the data jet energy resolution. We also apply the data jet reco/ID efficiencies (by dropping jets) to the MC sample. We find good agreement between the two distributions within errors.

Table XVI summarizes the jet reco/ID errors.

- The parameterization of the jet resolution is based on JES 5.0 with T42 applied (see Chapter 6.1.2.1). We need to account for the difference between the JES 5.0 and 5.3 parameterizations. It has been shown (see Figure 95) that there is a change of approximately 5% between JES 5.1 and 5.3 (65). A conservative error of 10% is therefore assigned to account for the jet resolution uncertainty.

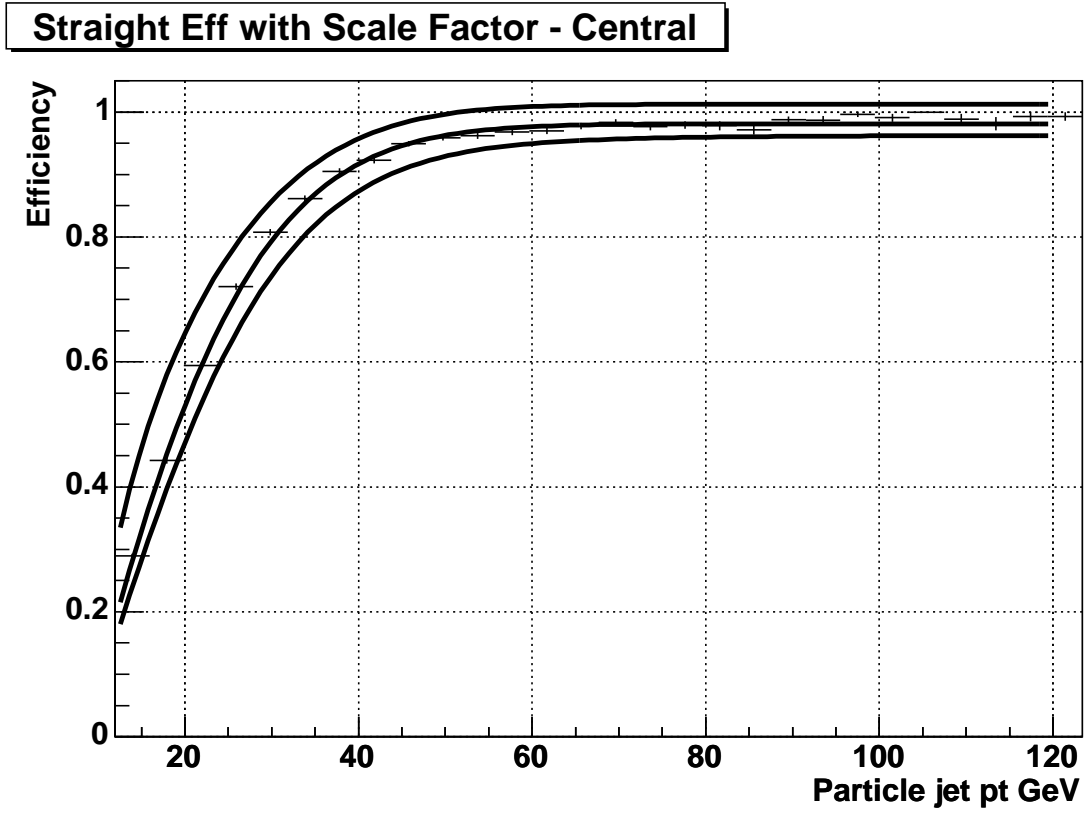


Figure 90. Jet reco/ID efficiencies with errors plotted versus particle jet p_T smeared with data energy resolution (central).

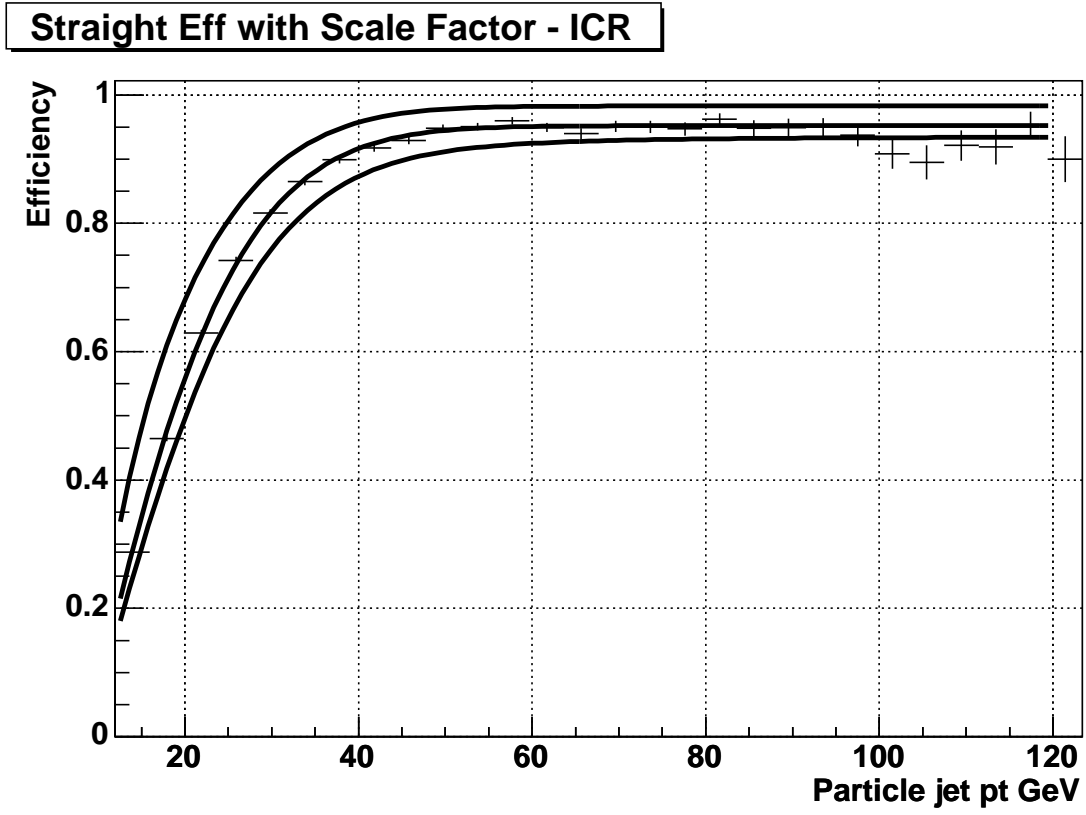


Figure 91. Jet reco/ID efficiencies with errors plotted versus particle jet p_T smeared with data energy resolution (ICR).

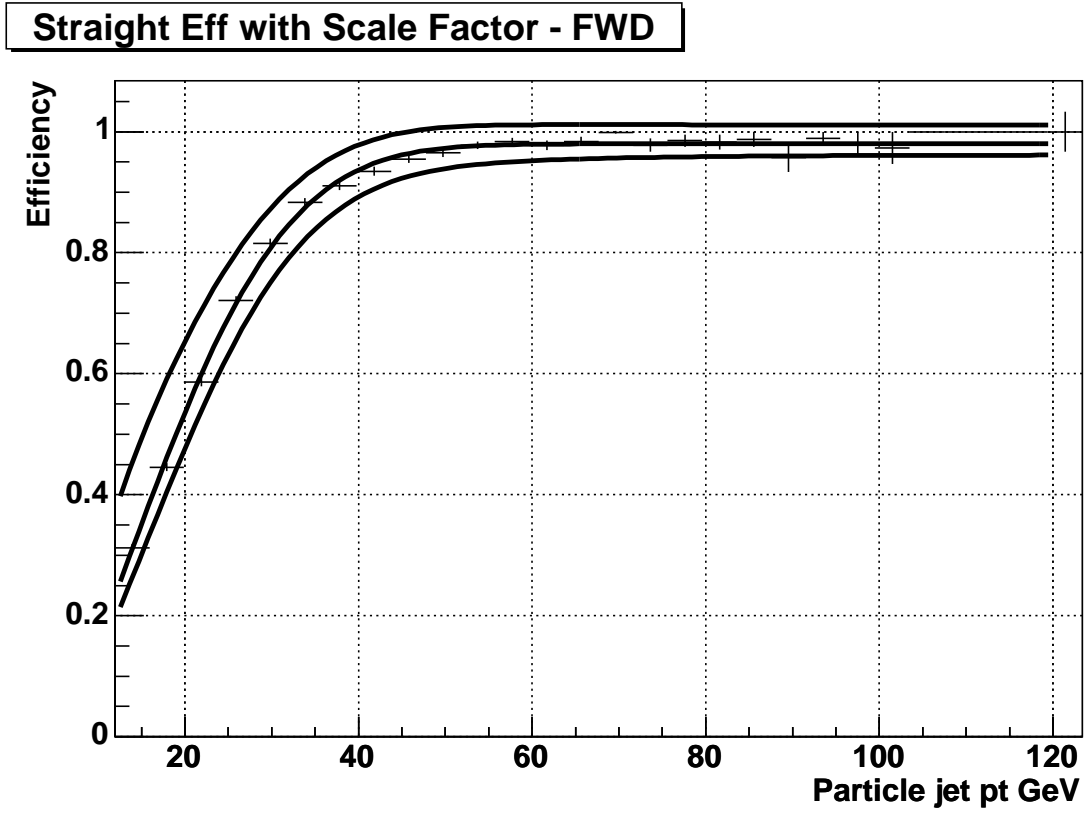


Figure 92. Jet reco/ID efficiencies with errors plotted versus particle jet p_T smeared with data energy resolution (forward).

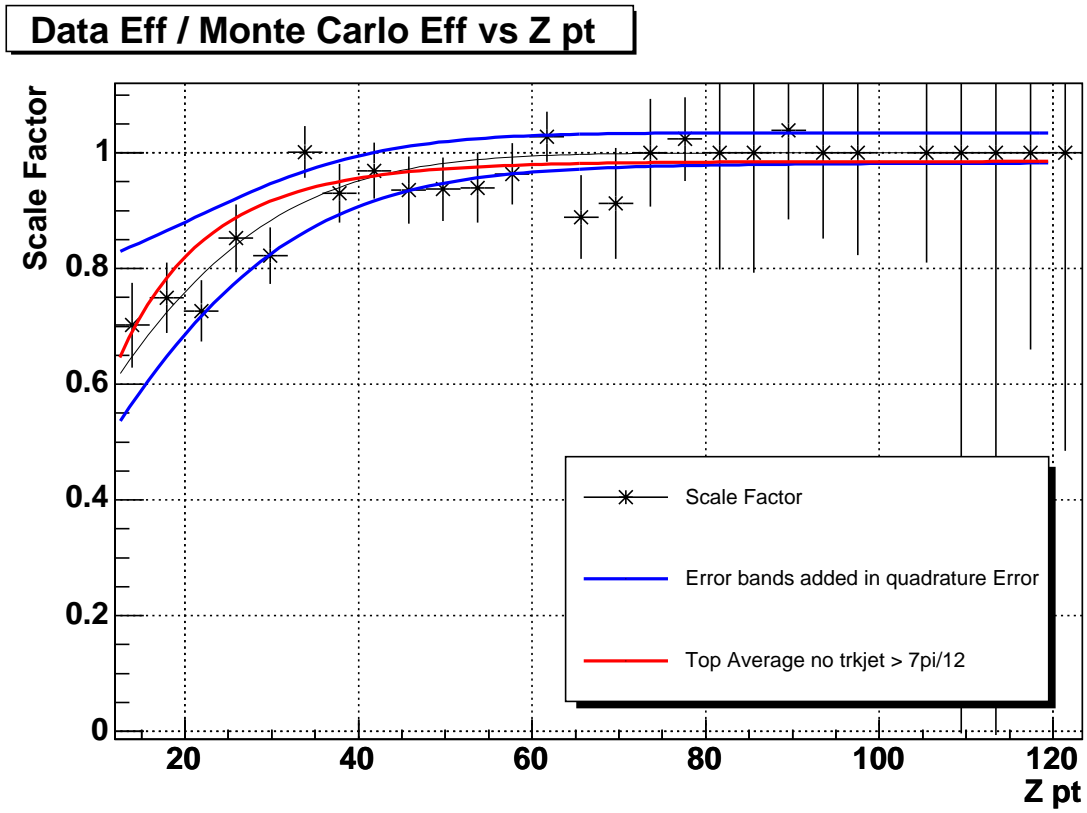


Figure 93. Comparing scale factors between the Top group and this analysis. Equivalent techniques were used in both cases.

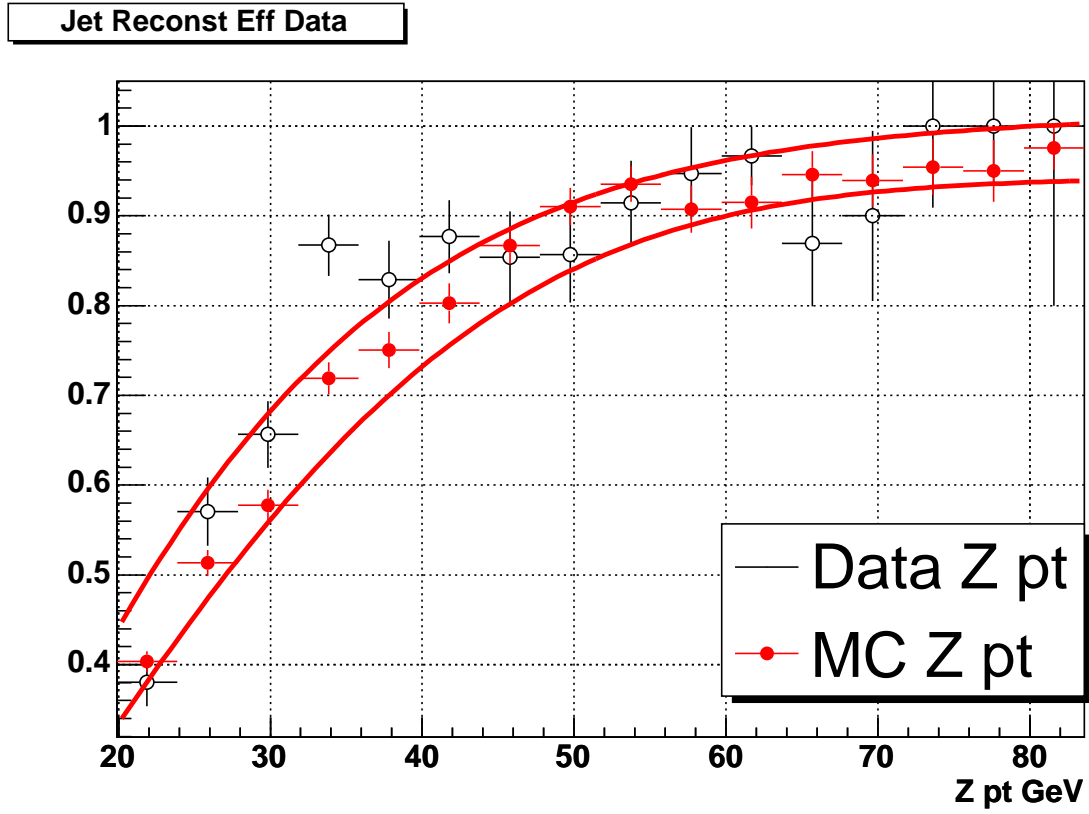


Figure 94. Comparing “efficiency” of finding a recoiling jet as a function of $Z p_T$ in data and MC.

Jet multiplicity	Cross Section	Jet Reco/ID Errors
≥ 1	29.6 pb	$+2.2$ -1.6 pb
≥ 2	4.50 pb	$+0.64$ -0.57 pb
≥ 3	0.655 pb	$+0.109$ -0.105 pb
≥ 4	0.157 pb	$+0.041$ -0.028 pb
≥ 5	0.1035 pb	$+0.0567$ -0.0287 pb

TABLE XVI

FINAL CROSS SECTIONS WITH JET RECO/ID ERRORS.

Jet Multiplicity	Cross Section	Jet Resolution Errors
≥ 1	29.6 pb	± 0.5 pb
≥ 2	4.50 pb	± 0.14 pb
≥ 3	0.655 pb	± 0.017 pb
≥ 4	0.151 pb	± 0.014 pb
≥ 5	0.1035 pb	± 0.0681 pb

TABLE XVII

FINAL CROSS SECTIONS WITH JET RESOLUTION ERRORS.

We estimate the error due to the jet resolution smearing in the unsmearing procedure (Chapter 6.5.2.1) by varying the data jet resolution by $\pm 10\%$. Table XVII summarizes the jet resolution errors.

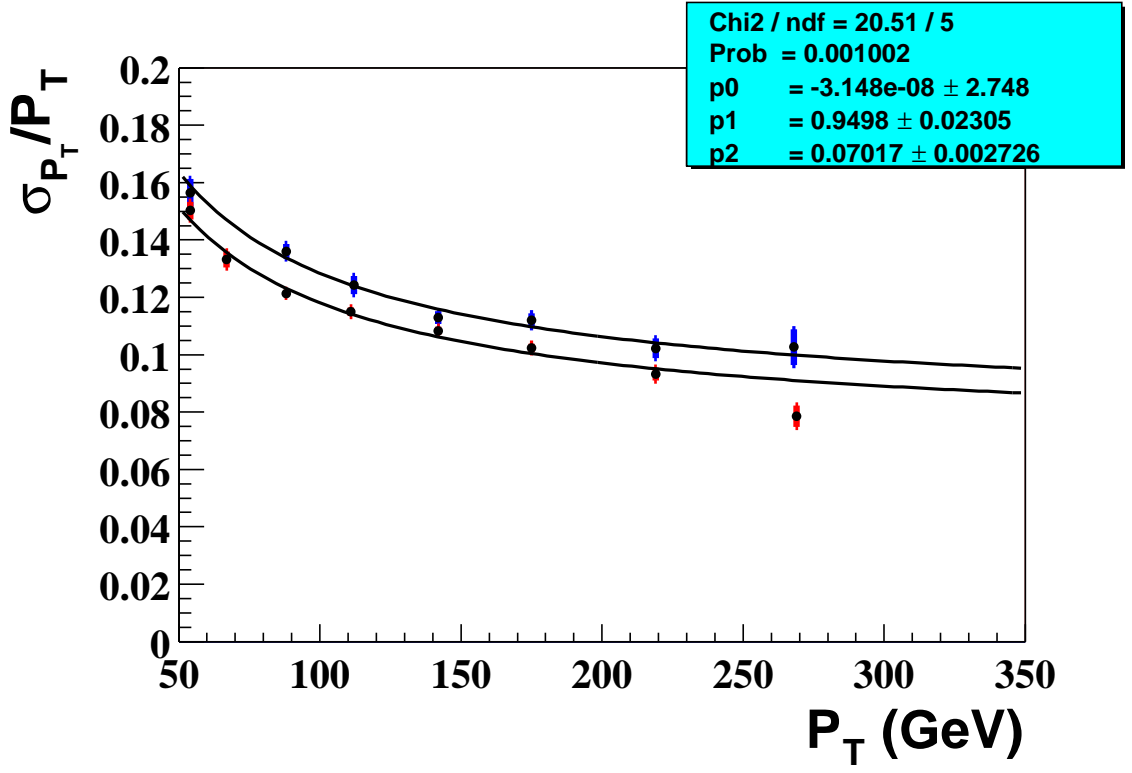


Figure 95. Comparing jet resolution for JES 5.1 (upper curve) and JES 5.3 (lower curve) in the central region of the Calorimeter. The difference is approximately 5% over the whole range.

Jet Multiplicity	Cross Section	Electron-jet-overlap Errors
≥ 1	29.6 pb	± 0.8 pb
≥ 2	4.50 pb	± 0.17 pb
≥ 3	0.655 pb	± 0.032 pb
≥ 4	0.151 pb	± 0.009 pb
≥ 5	0.1035 pb	± 0.0071 pb

TABLE XVIII

FINAL CROSS SECTIONS WITH ELECTRON-JET-OVERLAP CUT UNCERTAINTIES.

6.6.3 Electron-Jet-Overlap Systematic Error

For each jet multiplicity we derive electron-jet-overlap correction factors using $\Delta R=0.4$ and $\Delta R=0.7$ rejection cones and then use the middle value as the final correction. The systematic error is the difference between the middle values and the correction factors derived with $\Delta R=0.4$ and $\Delta R=0.7$. Additionally we apply a linear fit to the final errors in order to compensate for statistical fluctuations.

Table XVIII summarizes the systematic errors for the electron-jet-overlap cut.

6.6.4 Luminosity Systematic Error

The error due to the uncertainty in the luminosity measurement is 6.5% (16). Table XIX summarizes the luminosity errors.

Jet multiplicity	Cross Section	Luminosity Errors
≥ 0	248.9 pb	± 16.2 pb
≥ 1	29.6 pb	± 1.9 pb
≥ 2	4.50 pb	± 0.29 pb
≥ 3	0.655 pb	± 0.043 pb
≥ 4	0.151 pb	± 0.010 pb
≥ 5	0.1035 pb	± 0.0067 pb

TABLE XIX

FINAL CROSS SECTIONS WITH LUMINOSITY ERRORS.

6.6.5 Systematic Errors due to Efficiencies

In the following we take the systematic uncertainties of the object based efficiencies from Chapters 6.5.1.1 to 6.5.1.3, convert them into event based systematic uncertainties, and then propagate those uncertainties to the cross sections.

6.6.5.1 Trigger Efficiency

We estimate a relative systematic error of $\pm 1\%$ due to the variations in the trigger efficiencies versus jet multiplicity (see Chapter 6.5.1.1):

$$\varepsilon_{Object}(\text{pre-v12, inclusive sample}) = 94.6\%, \quad \delta\varepsilon_{Object} = 5\% \quad (6.12)$$

$$\varepsilon_{Event} = 2 \cdot \varepsilon_{Object} - \varepsilon_{Object}^2 = 99.7\% \quad (6.13)$$

$$\varepsilon_{Event}(-1\sigma) = 2 \cdot (\varepsilon_{Object} - \delta\varepsilon_{Object}) - (\varepsilon_{Object} - \delta\varepsilon_{Object})^2 = 98.9\% \quad (6.14)$$

$$\text{Relative Error} = \frac{99.7\% - 98.9\%}{99.7\%} = 0.8\% \approx 1\% \quad (6.15)$$

6.6.5.2 EM Reconstruction and Identification Efficiency

We estimate a relative systematic error of $\pm 7\%$ due to the variations in the EM reco and ID efficiencies versus jet multiplicity (see Chapter 6.5.1.2):

$$\varepsilon_{Object}(\text{data, inclusive sample}) = 88.9\%, \quad \delta\varepsilon_{Object} = 3\% \quad (6.16)$$

$$\varepsilon_{Event} = \varepsilon_{Object}^2 = 79.0\% \quad (6.17)$$

$$\varepsilon_{Event}(-1\sigma) = (\varepsilon_{Object} - \delta\varepsilon_{Object})^2 = 73.8\% \quad (6.18)$$

$$\text{Relative Error} = \frac{79.0\% - 73.8\%}{79.0\%} = 6.6\% \approx 7\% \quad (6.19)$$

6.6.5.3 EM-Track Match Efficiency

Table XX summarizes the relative systematic uncertainties due to the variations in the EM-Track matching efficiencies versus jet multiplicity (see Chapter 6.5.1.3). We estimate the uncertainties based on the following equations:

$$\varepsilon_{Object}(\text{data, n-jet sample}) = \varepsilon_n, \quad \delta\varepsilon_{Object}(\text{data, n-jet sample}) = \delta\varepsilon_n \quad (6.20)$$

$$\varepsilon_{Event} = 2 \cdot \varepsilon_n - \varepsilon_n^2 \quad (6.21)$$

$$\varepsilon_{Event}(-1\sigma) = 2 \cdot (\varepsilon_n - \delta\varepsilon_n) - (\varepsilon_n - \delta\varepsilon_n)^2 \quad (6.22)$$

Jet Multiplicity	Relative Error
≥ 1	0.5%
≥ 2	1.5%
≥ 3	2.3%
≥ 4	3.7%
≥ 5	5.5%

TABLE XX

RELATIVE ERRORS DUE TO UNCERTAINTY IN EM-TRACK MATCHING EFFICIENCIES.

$$\text{Relative Error} = \frac{\varepsilon_{Event} - \varepsilon_{Event}(-1\sigma)}{\varepsilon_{Event}} \quad (6.23)$$

6.6.5.4 Overall Efficiency Systematic Error

Table XXI summarizes the overall systematic error due to the efficiencies after adding all contributions in quadrature.

6.6.6 Jet Promotion Systematic Error

We study the effect of additional jets from multiple interactions within the same beam crossing, i.e. *jet promotion*. We compare jet multiplicities of events that have exactly one reconstructed primary vertex with events that have at least two reconstructed primary vertices (Table XXII).

The two samples are normalized with respect to the number of events in the inclusive jet multiplicity bin. Initially the single vertex sample contains 7,848 events and the 2 (or more)

Jet Multiplicity	Cross Section	Efficiency Errors
≥ 1	29.6 pb	± 2.1 pb
≥ 2	4.50 pb	± 0.32 pb
≥ 3	0.655 pb	± 0.047 pb
≥ 4	0.151 pb	± 0.011 pb
≥ 5	0.1035 pb	± 0.0093 pb

TABLE XXI

OVERALL SYSTEMATIC UNCERTAINTIES DUE TO EFFICIENCIES (TRIGGER, EM, TRACKING).

vertex sample contains 5,900 events.

We conclude that the jet promotion effect is small since the discrepancy between the two samples is within the statistical error.

We also compare the average number of reconstructed primary vertices for different jet multiplicity samples (Table XXIII) and do not see an effect within statistical errors.

6.6.7 Statistical Uncertainty

The statistical uncertainty has three contributions:

- We estimate the error due to the total number of corrected events δN_{corr} (corrected for Trigger, EM and Tracking inefficiencies) with the following Equation:

$$\delta N_{corr} = \sqrt{(w_{average} \cdot \delta N_{uncorr})^2 + (N_{uncorr} \cdot \delta w_{average})^2} \quad (6.24)$$

Jet multiplicity	Exactly one primary vertex	At least two primary vertices
≥ 0	5,900	5,900
≥ 1	705	696
≥ 2	92	97
≥ 3	11	16
≥ 4	3	1
≥ 5	1	1

TABLE XXII

NUMBER OF EVENTS FOR DIFFERENT INCLUSIVE JET MULTIPLICITIES WHEN REQUIRING EXACTLY ONE RECONSTRUCTED PRIMARY VERTEX AND AT LEAST TWO RECONSTRUCTED PRIMARY VERTICES. ENTRIES ARE NORMALIZED WITH RESPECT TO THE 2 VERTEX SAMPLE.

Jet multiplicity	Average number of primary vertices
≥ 1	1.583 ± 0.852
≥ 2	1.622 ± 0.911
≥ 3	1.733 ± 0.814
≥ 4	1.4 ± 0.8
≥ 5	2.0 ± 1.0

TABLE XXIII

AVERAGE NUMBER OF RECONSTRUCTED PRIMARY VERTICES FOR DIFFERENT JET MULTIPLICITIES.

where N_{corr} is the total number of corrected events, N_{uncorr} is the total number of uncorrected events, and $w_{average}$ is the average weight used to correct for EM, Trigger and Tracking inefficiencies (≈ 1.36).

- We estimate the error due to the number of background events δB by fitting an exponential function $a \cdot \exp(b \cdot x)$ to the measured number of QCD events (Figure 96) and then using the error due to the two fitting parameters a and b as the uncertainty. The error of the exponential fit takes into account that the fitting parameters a and b are correlated:

$$f(x) = a \cdot \exp(b \cdot x) \quad (6.25)$$

$$\delta f(x) = \sqrt{\left(\frac{\partial f}{\partial a} \cdot \delta a\right)^2 + \left(\frac{\partial f}{\partial b} \cdot \delta b\right)^2 + 2 \cdot \frac{\partial f}{\partial a} \cdot \frac{\partial f}{\partial b} \cdot \text{covariance}(a, b)} \quad (6.26)$$

- We add an additional error due to the statistical uncertainty of the acceptances (see Table XI).
- We add the statistical uncertainty due to the unsmearing and jet reco/ID coefficients (see Chapter 6.5.2.1).

Table XXIV summarizes the statistical errors.

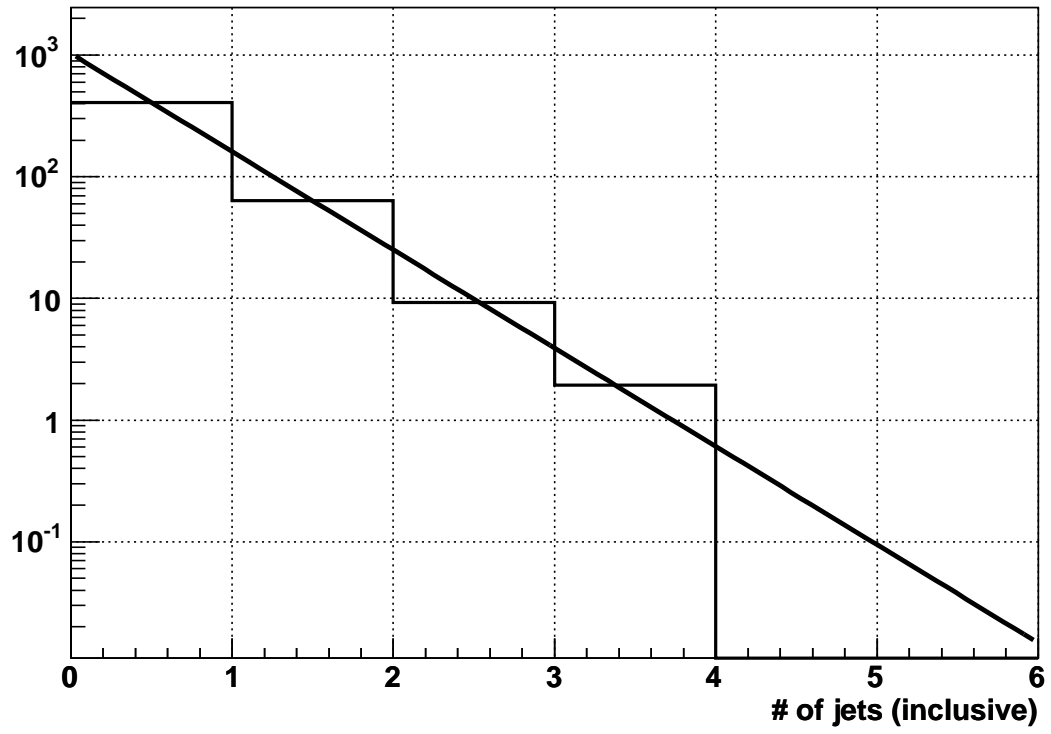


Figure 96. Exponential fit to the number of QCD events for different inclusive jet multiplicities.

Jet Multiplicity	Cross Section	Statistical Uncertainty
≥ 0	248.9 pb	± 2.5 pb
≥ 1	29.6 pb	± 0.8 pb
≥ 2	4.50 pb	± 0.32 pb
≥ 3	0.655 pb	± 0.129 pb
≥ 4	0.151 pb	± 0.070 pb
≥ 5	0.1035 pb	± 0.0738 pb

TABLE XXIV

CROSS SECTIONS WITH STATISTICAL ERRORS.

CHAPTER 7

CONCLUSIONS

7.1 Final Results

We measure the $Z/\gamma^*(\rightarrow e^+e^-)+\geq n$ Jet Cross Sections covering jet multiplicities of 0 to 5. The result is presented in terms of the absolute cross sections and cross section ratios normalized with respect to the inclusive cross section.

Table XXV summarizes all measured cross sections, together with uncertainties due to statistics, systematics, and luminosity. It also lists the number of fully corrected signal events for each jet multiplicity sample. Table XXVI and Figure 97 compare the measured cross sections with results from MCFM and CKKW MC simulations (see Chapter 5). The CKKW cross sections are normalized with respect to the measured cross section for the 1-jet sample. The matrix element generation of the CKKW samples was done up to jet multiplicities of 3. Higher jet multiplicities are due to parton showering and hadronization simulated with PYTHIA.

Table XXVII and Figure 98 compare the cross section ratios with results from MCFM and CKKW MC simulations. For cross section ratios (R_n) the luminosity measurement uncertainties cancel. All other systematic uncertainties contribute as shown in the following equation:

$$\delta R_n = \frac{\delta \sigma_n}{\sigma_0}, \quad \text{with } \sigma_0 = 248.9 \text{ pb.} \quad (7.1)$$

Jet Multiplicity	# of Signal Events	$Z/\gamma^*(\rightarrow e^+e^-)+\geq n$ Jet Cross Section
≥ 0	18,263.8	248.9 pb $\pm 2.5(\text{stat}) \pm 16.2(\text{lumi})$
≥ 1	2,550.7	29.6 pb $\pm 0.81(\text{stat}) \begin{smallmatrix} +4.3 \\ -4.0 \end{smallmatrix}(\text{sys}) \pm 1.9(\text{lumi})$
≥ 2	391.9	4.50 pb $\pm 0.32(\text{stat}) \begin{smallmatrix} +1.1 \\ -1.1 \end{smallmatrix}(\text{sys}) \pm 0.29(\text{lumi})$
≥ 3	63.6	0.655 pb $\pm 0.13(\text{stat}) \begin{smallmatrix} +0.22 \\ -0.22 \end{smallmatrix}(\text{sys}) \pm 0.043(\text{lumi})$
≥ 4	15.3	0.151 pb $\pm 0.070(\text{stat}) \begin{smallmatrix} +0.072 \\ -0.066 \end{smallmatrix}(\text{sys}) \pm 0.010(\text{lumi})$
≥ 5	6.8	0.104 pb $\pm 0.074(\text{stat}) \begin{smallmatrix} +0.10 \\ -0.06 \end{smallmatrix}(\text{sys}) \pm 0.0067(\text{lumi})$

TABLE XXV

CROSS SECTIONS FOR DIFFERENT INCLUSIVE JET MULTIPLICITIES. NUMBER OF SIGNAL EVENT ENTRIES HAVE UNSMEARING, JET RECO/ID AND ELECTRON-JET-OVERLAP CORRECTIONS APPLIED.

We also compare jet p_T distributions for different jet multiplicities between data and ALP-GEN+PYTHIA MC simulations (Figure 99).

We find our results to be in good agreement with QCD predictions.

7.2 Future Plans

Future work on this analysis at DØ includes the use of CKKW samples with matrix element generation of up to 5 jets. This will further improve cross section comparisons at higher jet multiplicities, as well as unsmearing results.

Additional background processes also need to be evaluated. Preliminary studies indicate that contributions from backgrounds such as $Z/\gamma^* \rightarrow \tau^+\tau^-$ are small.

Jet Multiplicity	Measured Cross Section	MCFM	CKKW
≥ 0	248.9 pb ± 16.4 (tot)	241.5 pb ± 0.1 (stat)	-
≥ 1	29.6 pb $^{+4.8}_{-4.6}$ (tot)	26.2 pb ± 0.044 (stat)	29.6 pb
≥ 2	4.50 pb $^{+1.2}_{-1.2}$ (tot)	5.21 pb ± 0.069 (stat)	5.22 pb
≥ 3	0.655 pb $^{+0.26}_{-0.26}$ (tot)	-	0.798 pb
≥ 4	0.151 pb $^{+0.10}_{-0.10}$ (tot)	-	0.096 pb
≥ 5	0.104 pb $^{+0.13}_{-0.10}$ (tot)	-	0.008 pb

TABLE XXVI

COMPARING MEASURED CROSS SECTIONS WITH RESULTS FROM MCFM AND CKKW.

Jet multiplicity	$\frac{\sigma(Z/\gamma^*(\rightarrow e^+e^-)+\geq n Jets)}{\sigma_{Z/\gamma^*}} [\cdot 10^{-3}]$	MCFM	CKKW
≥ 1	119.1 ± 3.3 (stat) $^{+17.2}_{-16.2}$ (sys)	108.4	119.1
≥ 2	18.1 ± 1.3 (stat) $^{+4.5}_{-4.3}$ (sys)	21.6	21.0
≥ 3	2.6 ± 0.52 (stat) $^{+0.90}_{-0.89}$ (sys)	-	3.2
≥ 4	0.61 ± 0.28 (stat) $^{+0.29}_{-0.27}$ (sys)	-	0.39
≥ 5	0.42 ± 0.30 (stat) $^{+0.42}_{-0.24}$ (sys)	-	0.03

TABLE XXVII

COMPARING MEASURED CROSS SECTION RATIOS WITH RESULTS FROM MCFM AND CKKW.

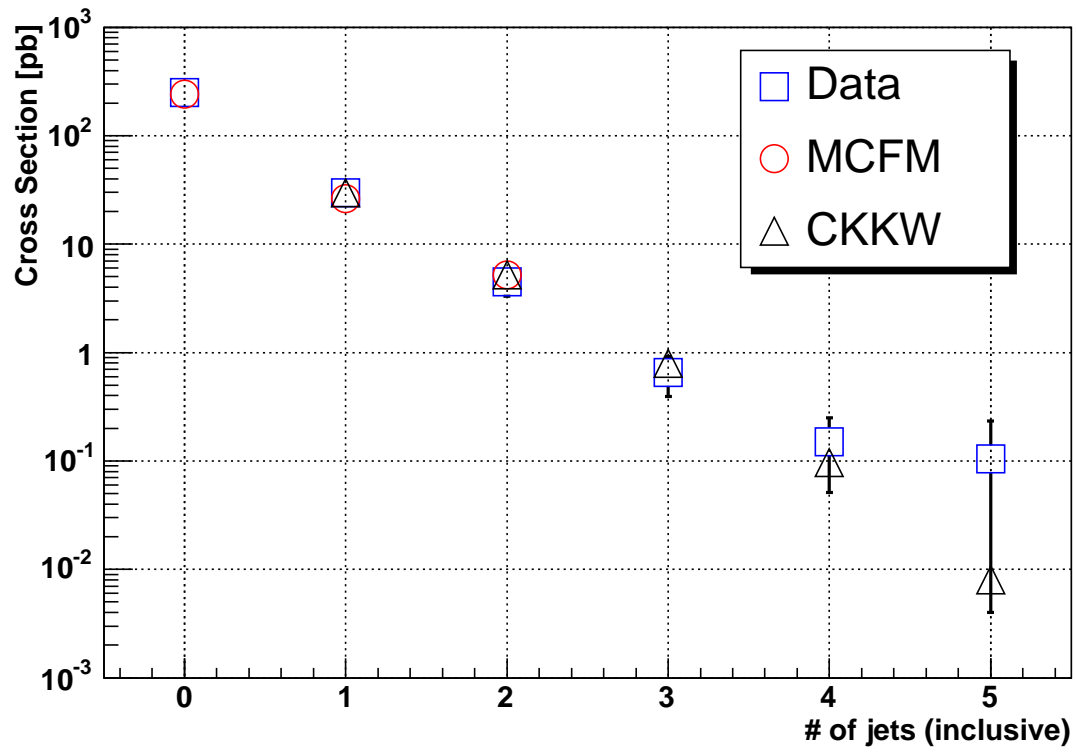


Figure 97. Cross sections for inclusive jet multiplicities in data (with total errors) compared with MCFM and CKKW.

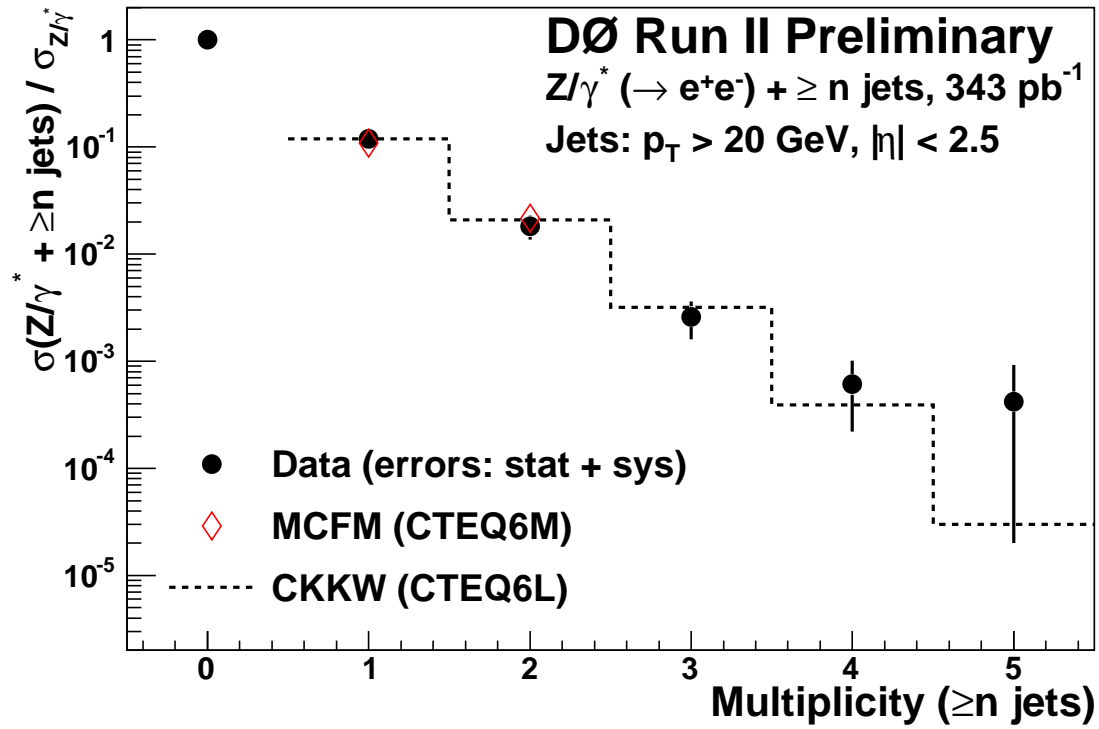


Figure 98. Ratios of the $Z/\gamma^*(\rightarrow e^+e^-) + \geq n$ jet cross sections to the total inclusive $Z/\gamma^* \rightarrow e^+e^-$ cross section versus n . The errors on the data include the combined statistical and systematic uncertainties. The line (CKKW) represents the predictions of LO Matrix Element calculations using PYTHIA for parton showering and hadronization, normalized to the measured $Z/\gamma^* + \geq 1$ jet cross section ratio. The open circles represent the MCFM predictions.

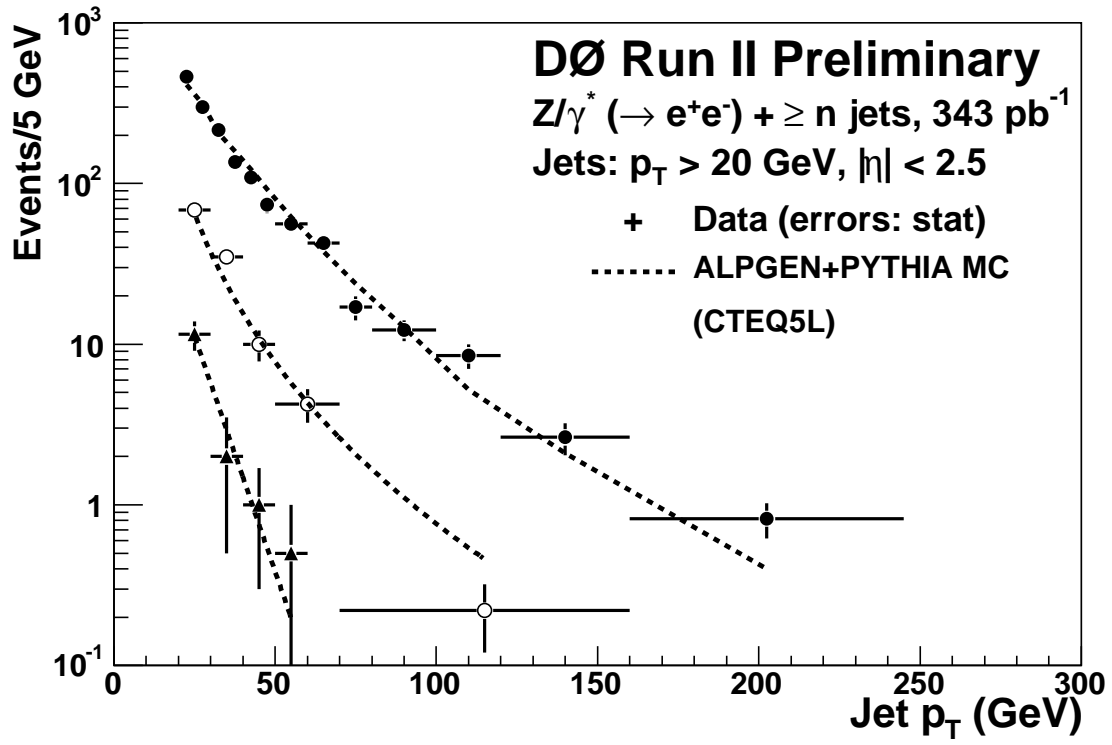


Figure 99. Data to theory (ALPGEN+PYTHIA) comparison for the highest p_T jet distribution in the $Z + \geq 1$ jet sample, for the second highest p_T jet distribution in the $Z + \geq 2$ jet sample and for the third highest p_T jet distribution in the $Z + \geq 3$ jet sample. The errors on the data are only statistical.

APPENDICES

Appendix A

THE DØ COLLABORATION

R. Piegaia, A. Salles

Universidad de Buenos Aires, Buenos Aires, Argentina

G.A. Alves, J. Barreto, H. da Motta, M.-E. Pol, M.S. Rangel, F.A.S. Rezende, M. Souza,

M. Vaz

LAFEX, Centro Brasileiro de Pesquisas Físicas, Rio de Janeiro, Brazil

A.C.S. Assis Jesus, M. Begalli, W. Carvalho, C. De Oliveira Martins, S. Greder,

J.R.P. Mahon, H.B. Malbouisson, J. Molina, L. Mundim, V. Oguri, N. Oliveira,

W.L. Prado da Silva, R.F. Rodrigues, A. Santoro, A. Sznajder

Universidade do Estado do Rio de Janeiro, Rio de Janeiro, Brazil

E.M. Gregores, S.M. Lietti, P.G. Mercadante, S.F. Novaes

Instituto de Física Teórica, Universidade Estadual Paulista, São Paulo, Brazil

S. Beale, C. Belanger-Champagne, K. Chan, Y. Coadou, D. Gillberg, Z. Liu, R.W. Moore,

D.C. O'Neil, W. Taylor, B. Vachon, M.C. Vetterli

University of Alberta, McGill University, Simon Fraser University and York

University, Canada

H.S. Mao

Institute of High Energy Physics, Beijing, People's Republic of China

L. Han, J. Yi

University of Science and Technology of China, Hefei, People's Republic of China

C. Avila, B. Gómez, D. Mendoza, J.P. Negret, R. Ramirez, J.M.R. Roldan

Universidad de los Andes, Bogotá, Colombia

V. Hynek, J. Kvita, R. Leitner, K. Soustruznik

Charles University, Center for Particle Physics, Prague, Czech Republic

P. Homola, Z. Hubacek, R. Otec, V. Simak, P. Vokac

Czech Technical University, Prague, Czech Republic

A. Kupco, M. Lokajicek, V. Vrba

**Institute of Physics, Academy of Sciences, Center for Particle Physics, Prague,
Czech Republic**

B. Hoeneisen

Universidad San Francisco de Quito, Quito, Ecuador

F. Badaud, P. Gay, Ph. Gris, V. Lesne, F. Tissandier

**Laboratoire de Physique Corpusculaire, IN2P3-CNRS, Université Blaise Pascal,
Clermont-Ferrand, France**

Y. Arnoud, F. Chevallier, S. Crépe-Renaudin, A.-M. Magnan, G. Sajot, J. Stark, C. Yu

**Laboratoire de Physique Subatomique et de Cosmologie, IN2P3-CNRS,
Université de Grenoble, Grenoble, France**

L. Berntzon, S. Calvet, M.-C. Cousinou, A. Duperrin, E. Kajfasz, S. Kermiche, A. Mendes,
E. Nagy, M. Talby

CPPM, IN2P3-CNRS, Université de la Méditerranée, Marseille, France

L. Duflot, J.-F. Grivaz, M. Jaffré, N. Makovec, P. Pétroff

Laboratoire de l'Accélérateur Linéaire, IN2P3-CNRS, Orsay, France

B. Andrieu, U. Bassler, G. Bernardi, E. Busato, L. Sonnenschein, S. Trincas-Duvoid,
J.-R. Vlimant

LPNHE, Universités Paris VI and VII, IN2P3-CNRS, Paris, France

M. Agelou, M. Besançon, F. Déliot, P. Demine, P. Lutz, M. Michaut, E. Perez, C. Royon,
V. Shary, B. Tuchming, D. Vilanova

DAPNIA/Service de Physique des Particules, CEA, Saclay, France

J.-L. Agram, D. Bloch, F. Charles, B. Clément, A. Gay, W. Geist, D. Gelé, A.-C. Le Bihan,
A. Lounis, I. Ripp-Baudot, V. Siccardi

**IReS, IN2P3-CNRS, Université Louis Pasteur Strasbourg, and Université de
Haute Alsace, France**

N. Estre, G. Grenier, T. Kurča, P. Lebrun, J.P. Martin, T. Millet, G.S. Muanza, P. Verdier
**Institut de Physique Nucléaire de Lyon, IN2P3-CNRS, Université Claude
Bernard, Villeurbanne, France**

C. Autermann, M. Erdmann, T. Hebbeker, D. Käfer, C. Magass, A. Meyer
RWTH Aachen, III. Physikalisches Institut A, Aachen, Germany

J. Meyer, A. Quadt, C. Schwanenberger, N. Wermes
Universität Bonn, Physikalisches Institut, Bonn, Germany

U. Blumenschein, V. Buescher, I. Fleck, H. Fox, G. Herten, K. Jakobs, J.-P. Konrath,
O. Mundal, C. Noeding, M. Titov, I. Torchiani

Universität Freiburg, Physikalisches Institut, Freiburg, Germany

C. Ay, M. Hohlfeld, T. Kuhl, D. Meder, S. Tapprogge, T. Trefzger, C. Zeitnitz
Universität Mainz, Institut für Physik, Mainz, Germany

O. Biebel, M. Binder, J. Elmsheuser, F. Fiedler, P. Haefner, B. Leonhardt, T. Nunnemann,
D. Schaile, P. Schieferdecker, R. Ströhmer

Ludwig-Maximilians-Universität München, München, Germany

K. Hamacher, A. Harel, H. Hoeth, S. Kersten, P. Mättig, C. Schmitt, M. Vaupel

Fachbereich Physik, University of Wuppertal, Wuppertal, Germany

S.B. Beri, V. Bhatnagar, R. Kaur, J.M. Kohli

Panjab University, Chandigarh, India

B. Choudhary, A. Kumar, M. Naimuddin, K. Ranjan, R.K. Shivpuri

Delhi University, Delhi, India

B.S. Acharya, P. Banerjee, S. Banerjee, S. Chakrabarti, A. Chandra, S.R. Dugad, P.K. Mal,

N.K. Mondal, K.J. Rani

Tata Institute of Fundamental Research, Mumbai, India

M. Cwiok, M.W. Grünewald

University College Dublin, Dublin, Ireland

S.H. Ahn, S.J. Hong, T.J. Kim, K.S. Lee, S.K. Park

Korea Detector Laboratory, Korea University, Seoul, Korea

H. Castilla-Valdez, E. De La Cruz-Burelo, P.L.M. Podesta-Lerma, A. Sánchez-Hernández

CINVESTAV, Mexico City, Mexico

K. Bos, S. Caron, P. de Jong, J.G. Hegeman, P. Houben, G.G.G. Massaro, P.J. van den Berg,

W.M. van Leeuwen, M. Vreeswijk

**FOM-Institute NIKHEF and University of Amsterdam/NIKHEF, Amsterdam,
The Netherlands**

M. Anastasoae, L.S. Ancu, S.J. de Jong, F. Filthaut, C.F. Galea, M.H. Kirby, N.A. Naumann

Radboud University Nijmegen/NIKHEF, Nijmegen, The Netherlands

V.M. Abazov, G.D. Alexeev, D.V. Bandurin, G. Erusalimtshev, G. Golovanov, A.M. Kalinin,

Y.M. Kharzheev, E.V. Komissarov, V.L. Malyshev, Y.P. Merekov, S.Y. Porokhovoi,

N.A. Russakovich, A.A. Shishkin, N.B. Skachkov, V.V. Tokmenin, L.S. Vertogradov,

Y.A. Yatsunenko

Joint Institute for Nuclear Research, Dubna, Russia

A. Evdokimov, V. Gavrilov, P. Polozov, G. Safronov, V. Stolin, V.I. Turtikov

Institute for Theoretical and Experimental Physics, Moscow, Russia

E.E. Boos, S. Bunichev, L.V. Dudko, P. Ermolov, D. Karmanov, A. Koubarovsky,

V.A. Kuzmin, A. Leflat, M. Merkin, V.I. Rud, S. Sherstnev, E.G. Zverev

Moscow State University, Moscow, Russia

V.A. Bezzubov, S.P. Denisov, S.A. Efremov, V.N. Evdokimov, A.V. Ferapontov,
A.K. Klimenko, V.M. Korablev, V.I. Koreshev, A.V. Kozelov, E.A. Kozlovsky, V.V. Lipaev,
A.V. Popov, A.A. Shchukin, Y.V. Sinkin, D.A. Stoyanova, I.A. Vasilyev, S.A. Zvyagintsev

Institute for High Energy Physics, Protvino, Russia

G. Alkhazov, S. Anufriev, V. Kim, A. Lobodenko, P. Neustroev, G. Obrant, Y. Scheglov,

L. Uvarov, S. Uvarov

Petersburg Nuclear Physics Institute, St. Petersburg, Russia

B. Åsman, C. Clément, P. Eerola, T. Ekelöf, N. Gollub, P. Hansson, S. Lager,

B. Lund-Jensen, T. Moa, J. Strandberg

Lund University, Royal Institute of Technology, Stockholm University, and

Uppsala University, Sweden

M. Audsley Hammond, I. Bertram, C. Biscarat, G. Borissov, B. Davies, M. Doidge,

A.J. Finch, M. Lewin, P. Love, A. Rakitine, P.N. Ratoff, A. Sopczak

Lancaster University, Lancaster, United Kingdom

C. Barnes, R. Beuselinck, I. Blackler, F. Blekman, C.P. Buszello, G. Davies, J.F. Hassard,

A. Jenkins, R. Jesik, P. Jonsson, P. Lewis, L. Lobo, M. Petteni, S. Robinson, T. Scanlon,

F. Villeneuve-Seguiér, P. Vint

Imperial College, London, United Kingdom

B. Cox, T. Edwards, M. Ford, J. Monk, M. Owen, K. Peters, S. Söldner-Rembold, P. Telford,

A.S. Turcot, T.R. Wyatt

University of Manchester, Manchester, United Kingdom

N.M. Giao, D. Han, T.M. Ngoc, H.T.K. Trang, T.D. Tu

Hochiminh City Institute of Physics, Hochiminh City, Vietnam

S. Anderson, S. Burke, E. Cheu, B. Gmyrek, K. Johns, J. Leveque, R. McCroskey, M. Shupe,

P. Tamburello, J. Temple, E.W. Varnes

University of Arizona, Tucson, Arizona 85721, USA

R.J. Madaras, M. Strovink

Lawrence Berkeley National Laboratory and University of California, Berkeley,

California 94720, USA

R.E. Hall

California State University, Fresno, California 93740, USA

S. Choi, R. Clare, J. Ellison, R. Gelhaus, A.P. Heinson, I. Iashvili, P.M. Perea, S.J. Wimpenny

University of California, Riverside, California 92521, USA

T. Adams, A. Askew, S. Blessing, N.J. Buchanan, D. Duggan, Y. Gershtein, S. Hagopian,
V. Hagopian, D. Kau, J. Lazoflores, W.M. Lee, J. Miao, S. Nelson, H.B. Prosper, J. Sekaric,
S. Sengupta, S. Sumowidagdo, S. Tentindo-Repond, H.D. Wahl

Florida State University, Tallahassee, Florida 32306, USA

B. Baldin, J.F. Bartlett, L. Bellantoni, R. Bernhard, P.C. Bhat, A. Boehnlein, A. Bross,
S. Burdin, W.E. Cooper, M. Demarteau, D. Denisov, H.T. Diehl, M. Diesburg, V.D. Elvira,
J. Estrada, H.E. Fisk, S. Fu, S. Fuess, E. Gallas, K. Gounder, H. Greenlee, S. Grünendahl,
G. Gutierrez, K. Hanagaki, R. Illingworth, A.S. Ito, M. Johnson, A. Jonckheere, A. Juste,
P. Kasper, B. Klima, S. Krzywdzinski, F. Lehner, Q.Z. Li, D. Lincoln, R. Lipton, A.L. Lyon,
Y. Maravin, M. Martens, K.W. Merritt, M. Mulders, A. Nomerotski, V. O'Dell, N. Oshima,
V.M. Podstavkov, P.A. Rapidis, P. Rubinov, G. Savage, V. Sirotenko, R.P. Smith, L. Stutte,
M. Tomoto, M. Weber, D. Wicke, M. Wobisch, J. Womersley, R. Yamada, T. Yasuda,
M. Zanabria, D. Zhang

Fermi National Accelerator Laboratory, Batavia, Illinois 60510, USA

M. Adams, M. Buehler, M. Camuyrano, C.E. Gerber, J.M. Heinmiller, G.J. Otero y Garzón,
E. Shabalina, A. Stone, T. Ten, N. Varelas

University of Illinois at Chicago, Chicago, Illinois 60607, USA

L. Bagby, G. Blazey, D. Chakraborty, A. Dyshkant, M. Eads, M. Fortner, D. Hedin,
J.G.R. Lima, A.K.A. Maciel, X. Song, N.M. Tran, S. Uzunyan, A. Zatserklyaniy, V. Zutshi

Northern Illinois University, DeKalb, Illinois 60115, USA

T. Andeen, D. Buchholz, G.A. Davis, M. Gagliardi, J. Hays, H. Schellman, D. Strom,
S. Yacoob, S.W. Youn

Northwestern University, Evanston, Illinois 60208, USA

R. Abrams, D. Bauer, J. Rieger, K. Stevenson, R. Van Kooten, L. Welty, D. Zieminska,
A. Zieminski

Indiana University, Bloomington, Indiana 47405, USA

O. Boeriu, N.M. Cason, E. Galyaev, A. Goussiou, M.D. Hildreth, D. Karmgard,
A. Kharchilava, D. Lam, H. Luo, M. Lynker, Y. Pogorelov, R. Ruchti, W.D. Shephard,
P. Svoisky, J. Torborg, J. Warchol, M. Wayne, N. Xuan

University of Notre Dame, Notre Dame, Indiana 46556, USA

O. Atramentov, J.M. Hauptman

Iowa State University, Ames, Iowa 50011, USA

P. Baringer, A. Bean, L. Christofek, D. Coppage, J. Gardner, C. Hensel, S. Jabeen,
T. Moulik, G.W. Wilson

University of Kansas, Lawrence, Kansas 66045, USA

M. Ahsan, T.A. Bolton, K. Harder, D. Onoprienko, F. Rizatdinova, M. Shamim, R.A. Sidwell,

M. Smith, E. Von Toerne

Kansas State University, Manhattan, Kansas 66506, USA

M. Das, Z.D. Greenwood, N. Parashar, L. Sawyer, J. Steele

Louisiana Tech University, Ruston, Louisiana 71272, USA

A. Baden, S. Eno, N.J. Hadley, C. Jarvis, S. Kunori, J. Mans, M.P. Sanders, T. Toole,

M. Verzocchi, L. Wang, M. Wetstein, M. Yan

University of Maryland, College Park, Maryland 20742, USA

K.M. Black, J.M. Butler, D.K. Cho, A. Das, S.N. Fatakia, L. Feligioni, U. Heintz, J. Kasper,

M. Narain

Boston University, Boston, Massachusetts 02215, USA

G. Alverson, E. Barberis, S. Doulas, R. Harrington, G. Hesketh, S. Reucroft, D. Shpakov,

D.R. Wood

Northeastern University, Boston, Massachusetts 02115, USA

A. Alton, J.D. Degenhardt, A. Magerkurth, H.A. Neal, J. Qian, Z. Zhao, B. Zhou

University of Michigan, Ann Arbor, Michigan 48109, USA

M. Abolins, J. Benitez, R. Brock, J. Dyer, D. Edmunds, R. Hauser, J. Kalk, J. Kozminski,
J. Linnemann, B.G. Pope, R. Schwienhorst, R. Unalan, H. Weerts

Michigan State University, East Lansing, Michigan 48824, USA

A. Melnitchouk, B. Quinn

University of Mississippi, University, Mississippi 38677, USA

A. Bellavance, K. Bloom, D. Claes, A. Dominguez, C. Lundstedt, S. Malik, G.R. Snow,
M. Voutilainen

University of Nebraska, Lincoln, Nebraska 68588, USA

W. Fisher, J. Haley, A. Schwartzman, C. Tully

Princeton University, Princeton, New Jersey 08544, USA

T. Bose, G. Brooijmans, H. Evans, A. Haas, C. Johnson, I. Katsanos, D. Khatidze,
B. Kothari, S. Lammers, J. Mitrevski, M. Mulhearn, J. Parsons, P.M. Tuts

Columbia University, New York, New York 10027, USA

M. Begel, J. Cammin, K.M. Chan, R. Demina, T. Ferbel, C. Garcia, G. Ginther, A. Khanov,
T. Negrini, S.-J. Park, M.-A. Pleier, P. Slattery, M. Zielinski

University of Rochester, Rochester, New York 14627, USA

S. Desai, H. Dong, P.D. Grannis, J. Guo, J.D. Hobbs, Y. Hu, R. McCarthy, Y.D. Mutaf,
N. Parua, M. Rijssenbeek, R.D. Schamberger, S. Towers, D. Tsybychev, A. Yurkewicz, J. Zhu

State University of New York, Stony Brook, New York 11794, USA

S. Kahn, J. Kotcher, A. Patwa, S. Protopopescu, S. Snyder, K. Yip

Brookhaven National Laboratory, Upton, New York 11973, USA

J. Snow

Langston University, Langston, Oklahoma 73050, USA

B. Abbott, P. Gutierrez, I. Hall, S. Jain, M. Kopal, A. Pompoš, H. Severini, P. Skubic,

M. Strauss

University of Oklahoma, Norman, Oklahoma 73019, USA

B.C.K. Casey, D. Chapin, D. Cutts, R. Hooper, S. Kesisoglou, G. Landsberg,

S.E.K. Mattingly, R. Partridge, Y. Xie, H.D. Yoo

Brown University, Providence, Rhode Island 02912, USA

A. Brandt, D. Brown, K. De, F. Jaafari, V. Kaushik, H. Kim, J. Li, M. Sosebee, B. Spurlock,

M.A. Strang, A. Vartapetian, A. White, J. Yu

University of Texas, Arlington, Texas 76019, USA

R. Kehoe, P. Renkel

Southern Methodist University, Dallas, Texas 75275, USA

P. Bargassa, M. Cooke, M. Corcoran, S.J. Lee, D. Mackin, H. Miettinen, P. Padley,

G. Pawloski

Rice University, Houston, Texas 77005, USA

R. Hirosky, A. Kryemadhi, K. Nelson

University of Virginia, Charlottesville, Virginia 22901, USA

T.H. Burnett, T. Gadfort, A. Garcia-Bellido, G. Gaudio, H.J. Lubatti, G. Watts, T. Zhao

University of Washington, Seattle, Washington 98195, USA

Appendix B

THE LEVEL 2 TRIGGER SYSTEM AND ALPHA BOARDS

Level 2 is an essential part of the DØ trigger and data acquisition system (66), (67), (68), (69). It was designed to provide a reduction in the event rate by a factor of 10 within a 100 μsec time window while inducing less than 5% deadtime. As outlined in Chapter 3.4.2 the L2 trigger system is organized as a two-stage *stochastic pipeline*. In the first step (*preprocessing stage*) sub-detector based proto-objects are formed by preprocessors. The second step (*global processing*) combines the information provided by the preprocessors to make the event-wide L2 trigger decision. One advantage of this design is that each preprocessor is able to operate in parallel, independently from all other preprocessors. This allows to avoid deadtime since decision times can vary significantly from event to event. Additionally up to 16 events can be queued in buffers (*FIFOs*) between the stages. Figure 100 illustrates the relation between sub-detectors, and L1/L2 trigger elements.

B.1 The Standard Level 2 Crate

All L2 systems occupy 9U^1 VME crates (70):

- Forward Muon Preprocessor (L2MUF)
- Central Muon Preprocessor (L2MUC)

¹1U = 1.75 in

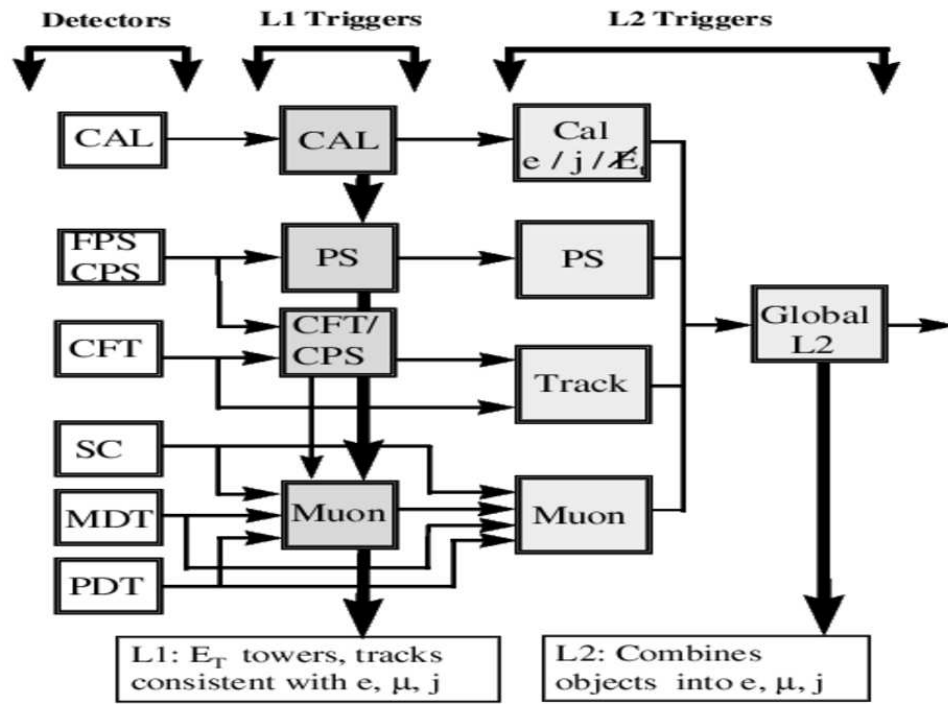


Figure 100. L1 and L2 trigger elements. Horizontal arrows are indicating the dataflow.

- Calorimeter Preprocessor (L2CAL)
- Preshower Preprocessor (L2PS)
- Tracking Preprocessor (L2CTT/L2STT)
- Global Processor (L2GBL)

Each crate contains a 64-bit VME bus (71) and a custom-built high-speed bus (*Magic Bus*, or MBus) for data-handling on an auxiliary backplane (72). The 128 bit MBus supports data rates of up to 320 Mbit/s. Figure 101 shows a schematic view of the L2CAL crate with its main components:

MPM (*Multi Port Memory*): A Bit3 MPM card is used as the VME crate controller. It downloads run-time parameters and reports monitoring data to the Trigger Control Computer (TCC¹).

VBD (*VME Buffer Driver*): A VBD card is used to write data to the L3 system. The VBD cards were later replaced by VME single board computers (SBC).

Workers/Administrator (*Alpha Boards*): The Alpha Boards perform the main processing step within the L2 trigger system. Their main purpose is the application of the L2 trigger algorithms (*Worker*). They also handle additional event processing and local trigger control tasks (*Administrator*). A detailed overview of the Alpha Board system architecture is given in Chapter B.2. The Alpha Boards were later substituted by *Beta Boards* (73).

¹TCC handles run control, downloads run-specific information, and collects monitoring data.

MBT (*Magic Bus Transceiver*): The MBT cards (74) receive L1 information and broadcast it to the Worker/Administrator via the MBus. After preprocessing is finished, the outputs are sent to the L2 Global Processor (L2GBL). The MBT cards also receive information regarding L1 trigger accepts, L2 trigger decisions, and system-wide initializations (*Serial Command Link Initialize*, or SCLinit). Depending on the processing load additional *Assistant MBTs* can be added to the *Pilot MBT*.

Specialized hardware: In some cases additional specialized hardware for data conversion and processing is added. In the case of the L2CAL crate the L1 input signals arrive in the form of fiber-optic cables. A special converter card (*Fiber Input Converter*, or FIC) translates optical into electrical signals (75).

B.2 Level 2 Alpha Processors

The overall design of the Alpha Board (Figure 102, Reference (76)) is based on the layout of the DEC ¹ PC164 motherboard (77). It features a 500 MHz Alpha CPU running under real-time Linux. In addition to the internal PCI bus several elements supporting VME and MBus interfaces have been added. Figure 103 shows a schematic view of the Alpha Board. The main components are described in the following.

B.2.1 PC164 Based Design

The Alpha Board uses the first commercially available 64-bit RISC processor: a 500 MHz Alpha 21164 CPU (78), (79). It can execute 2-4 instructions per cycle. The 500 MHz CPU

¹Digital Equipment Corp. merged with Compaq Computer Corp. in 1998.

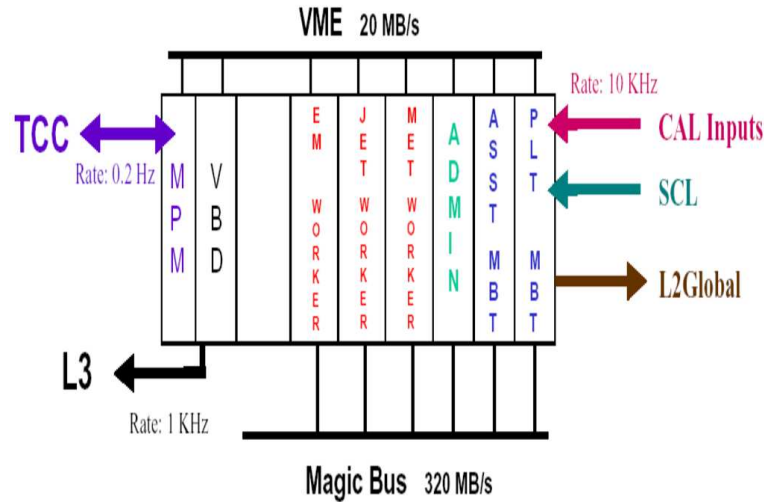


Figure 101. Layout of Level 2 calorimeter (L2CAL) crate with main components.

frequency is generated by a 50 MHz oscillator by means of a divide-by-10 phase-locked loop circuit.

The Alpha Board has several caches implemented, both onchip (integrated into the CPU) and external. 8 kB data and instruction caches (Dcache and Icache, respectively) buffer the most frequently used data and instructions to speed up processing. A secondary onchip 96 kB mixed data and instruction cache (Scache) is also used. A third level of external cache (4 MB) is not being utilized.

An interface between the CPU, main memory, and the PCI bus is provided by the 21172 Core Logic Chipset (Figure 104, Reference (80)). The 21172 Chipset consists of the 21172-CA chip (CIA) which provides the interface between the CPU and the PCI bus. It also provides

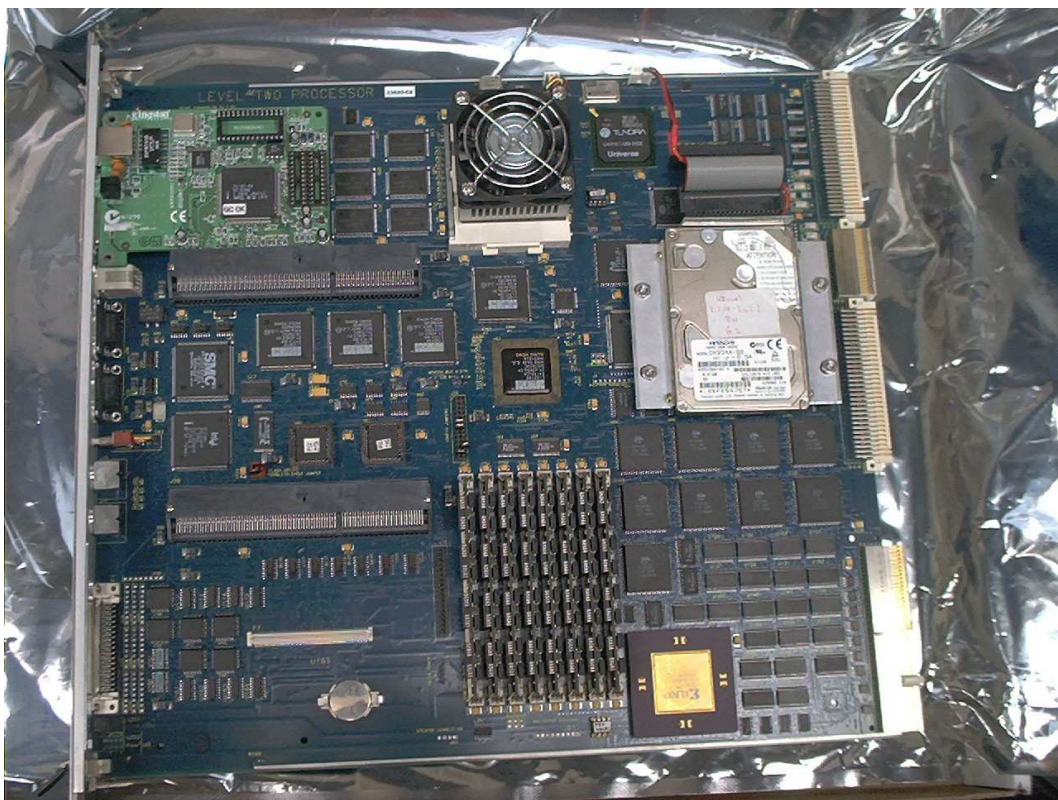


Figure 102. Level 2 Alpha Board with Ethernet card and hard disk drive.

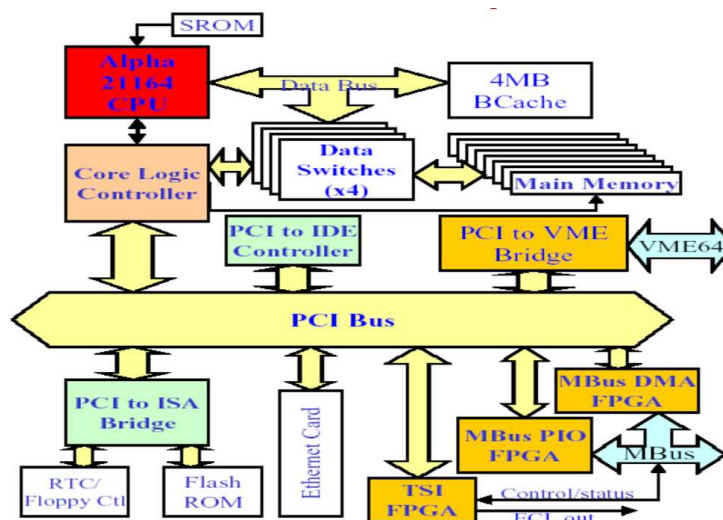


Figure 103. Block diagram of Level 2 Alpha Board.

The Alpha Board carries two kinds of firmware. A 128 kB SROM chip is directly connected to the Icache. It contains the boot code that is loaded into the CPU at power-up, including the initialization of the PCI bus, the setting of registers in the CIA, the setting up of the various caches and memory, and finally the copying of the contents of the Flash ROM to memory. The 1 MB Flash ROM chip contain OS and task specific instructions. This includes instructions to download user code via a PCI Ethernet card, a rudimentary local debugger (“Debug Monitor”), and the server for a remote debugger. The SROM chip is installed in a socket, and can therefore

be programmed by using an external device programmer. The Flash ROM chip is soldered to the board, and must be programmed in situ.

A bank of eight SIMM slots provides 128 MB of DRAM memory.

The 64-bit 33 MHz PCI bus has two expansion slots. A standard PCI Ethernet card connected to one of the PCI slots is used for remote access. Two programmable chips (PLDs) are used for PCI interrupt handling and bus arbitration.

A PCI-IDE interface chip allows to connect a 6 GB IDE hard disk drive, which has real-time Linux installed.

A PCI-ISA bridge provides support for external devices such as mouse, keyboard, and floppy drive. It also supports a parallel port, two serial ports, and a real time clock. The ISA bus is used to access the Flash ROM.

B.2.2 Magic Bus Programmed Input/Output

An interface between MBus and PCI bus is provided by the Magic Bus Programmed I/O chip (MBusPIO). It allows to read and write data between the two address spaces and thereby provides a way of communication between different cards that are connected to the MBus. For example, a board connected to the MBus can write or read into Alpha Board memory. A programmable Xilinx XC4036EX chip (MAGICFPGA) is used for this task.

B.2.3 Magic Bus Direct Memory Access Interface

In order to boost processing time, data is transferred to and from Alpha Board memory by direct memory access (DMA), i.e. data on the MBus goes directly to Alpha Board memory

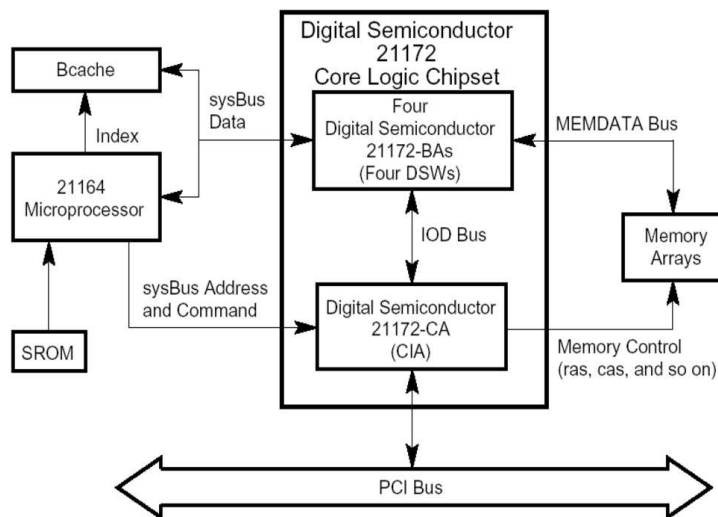


Figure 104. Block diagram of the 21172 Core Logic Chipset.

without involving the CPU. This *DMA engine* is implemented in two programmable chips: a Xilinx FPGA, and a Cypress CPLD.

B.2.4 VME Interface

A 64-bit PCI-VME interface is provided by the Tundra Universe II chip, by mapping “windows” of VME address space to Alpha Board memory space (81).

B.2.5 TSI Interface

The TSI interface is used to receive and send additional information to the trigger system. Is is also used to monitor the state of the Alpha Board processing elements.

CITED LITERATURE

1. Arnison, G. et al.: . Phys. Lett., 126B:398, 1983.
2. Bagnaia, P.: . Phys. Lett., 129B:130, 1983.
3. Veltman, M.: Facts and Mysteries in Elementary Particle Physics. World Scientific, 2003.
4. Griffiths, D.: Introduction to Elementary Particles. John Wiley & Sons, 1987.
5. Halzen, F. and Martin, A.: Quarks and Leptons. John Wiley & Sons, 1984.
6. Quigg, C.: Gauge Theories of the Strong, Weak, and Electromagnetic Interactions. Westview Press, 1983.
7. Ellis, R. et al.: QCD and Collider Physics. Cambridge University Press, 1996.
8. Prosper, H. and Danilov, M.: Techniques and Concepts of High-Energy Physics XII. NATO Science Series, 2003.
9. Nurse, E.: A Measurement of the Inclusive $Z/\gamma^* \rightarrow \mu^+\mu^-$ Cross Section and Study of W and Z Events in $p\bar{p}$ Collisions at D0. University of Manchester, 2005.
10. The Particle Adventure. 2002.
<http://particleadventure.org/particleadventure/>.
11. Thompson, J.: Introduction to Colliding Beams at Fermilab. FERMILAB-TM-1909, 1994.
12. General Reference Documents for Accelerators. 2002.
http://www-numi.fnal.gov/workgrps/protonwg/accel_reference.html.
13. Accelerator Concepts Rookie Books. 2003.
http://www-bdnew.fnal.gov/operations/rookie_books/rbooks.html.
14. Mutaf, Y.: Measurement of the Ratio of Inclusive Cross Sections $\sigma(p\bar{p} \rightarrow Z + b\text{-jet})/\sigma(p\bar{p} \rightarrow Z + \text{jet})$ at $\sqrt{s} = 1.96$ TeV. Stony Brook University, 2005.

15. Fermilab Anti-Proton Source Rookie Book. 1999.
http://www-bdnew.fnal.gov/pbar/documents/PBAR_Rookie_Book.PDF.
16. Edwards, T. et al.: Determination of the Effective Inelastic p anti-p Cross Section for the D0 Run II Luminosity Measurement. FERMILAB-TM-2278-E, 2004.
17. Ferbel, T.: A Brief Description of the D0 Detector in Run II. 2004.
<http://www-d0.fnal.gov/Run2Physics/WWW/templates/detector.tex>.
18. D0 Collaboration: The Upgraded D0 Detector. Preprint submitted to Elsevier Science, 2005.
19. D0 Collaboration: D0 Silicon Tracker Technical Design Report. 1994.
http://d0server1.fnal.gov/projects/silicon/www/tdr_final.ps.
20. D0 Collaboration: The D0 Upgrade: Central Tracker Technical Design Report. 1999.
http://d0server1.fnal.gov/users/stefan/www/CFT_TDR/CFT_TDR.ps.
21. Adams, M. et al.: Design Report of the Central Preshower Detector for the D0 Upgrade. 1996.
<http://d0server1.fnal.gov/users/qianj/CPS/doc/dn3104.pdf>.
22. Gordeev, A. et al.: Technical Design Report of the Forward Preshower Detector for the D0 Upgrade. D0 Note 3445, 1998.
23. Abachi, S. et al.: . Nucl. Instrum. Methods Phys. Res. A, 338:185, 1994.
24. Snyder, S.: Measurement of the Top Quark Mass at D0. Stony Brook University, 1995.
25. Baldin, B. et al.: Technical Design Report of the Central Muon System. D0 Note 3365, 1997.
26. Alexeev, G. et al.: Technical Design Report of the D0 Forward Muon Tracking Detector Based on Mini-Drift Tubes. D0 Note 3366, 1997.
27. Yurkewicz, A.: Search for Evidence of Supersymmetry in the Like-sign Dimuon Channel at the D0 Experiment. Michigan State University, 2004.
28. Blazey, J.: The D0 Run II Trigger.
<http://niuhep.physics.niu.edu/~blazey/rt.ps>.

29. D0 Collaboration: d0reco. 2004.
<http://www.d0.fnal.gov/Run2Physics/WWW/algorithm.htm>.
30. Borisov, G.: Ordering a Chaos... or Technical Details of AA Tracking. 2004.
http://www-d0.fnal.gov/global_tracking/talks/20030228/talk-adm-030228.ps.
31. Khanov, A.: HTF: Histogramming Method for Finding Tracks. D0 Note 3778, 2000.
32. Haas, A.: A Search for Neutral Higgs Bosons at High $\tan\beta$ in Multi-jet Events from $p\bar{p}$ Collisions at $\sqrt{s} = 1960$ GeV. University of Washington, 2004.
33. Schwartzman, A. and Narain, M.: Probabilistic Primary Vertex Selection. D0 Note 4042, 2002.
34. Melnitchouk, A.: Search for non-SM Light Higgs Boson in the $h \rightarrow \gamma\gamma$ Channel. Brown University, 2004.
35. Busato, E. and Andrieu, B.: Jet Algorithms in the D0 Run II Software: Description and User's Guide. D0 Note 4457, 2004.
36. Agram, J.-L. et al.: Jet Energy Scale at D0 Run II. D0 Note 4720, 2005.
37. D0 JES Group: Certified Jet Energy Scale.
http://www-d0.fnal.gov/phys_id/jes/d0_private/certified/certified_jes.html.
38. Mrenna, S.: Event Generators.
<http://www.phys.psu.edu/~cteq/schools/summer04/mrenna/mrenna.pdf>.
39. Baer, H. et al.: Les Houches Guidebook to Monte Carlo Generators for Hadron Collider Physics. hep-ph/0403045, 2004.
40. Sjostrand, T. et al.: PYTHIA 6.3 Physics and Manual. hep-ph/0308153, 2003.
41. Mangano, M.: Higher-order QCD processes via LO matrix-element MC's.
<http://www.wlap.org/file-archive/atlas/20040622-umwlap002-02-mangano.pdf>.
42. Mangano, M.: Merging multijet matrix elements and shower evolution in hadronic collisions.
<http://mlm.home.cern.ch/mlm/talks/lund-alpge.pdf>.

- 43. Catani, S. et al.: QCD matrix elements + parton showers. JHEP11(2001)063, 2001.
- 44. Michelangelo, L. et al.: A Generator for Hard Multiparton Processes in Hadronic Collisions. hep-ph/0206293, 2002.
- 45. Mangano, M.: ALPGEN V1.3.
<http://mlm.home.cern.ch/mlm/alpgen/>.
- 46. Maltoni, F.: MadEvent: Automatic Event Generation with MADGRAPH. hep-ph/0208156, 2002.
- 47. Mrenna, S.: Mrenna Matched Datasets.
http://cepa.fnal.gov/personal/mrenna/Matched_Dataset_Description.html.
- 48. Mrenna, S. and Richardson, P.: Matching matrix elements and parton showers with HERWIG and PYTHIA. JHEP05(2004)040, 2004.
- 49. Private Communication with Suyong Choi (suyong@fnal.gov) and <http://mcfm.fnal.gov/>.
- 50. Ellis, K.: A critical review of vector boson + jets Monte Carlos.
http://www-cdf.fnal.gov/Tevatron-Connection/QCD_Theory_Keith.pdf.
- 51. Ellis, K.: Method 2 at NLO. hep-ph/0405276, 2004.
- 52. Fisyak, Y. and Womersley, J.: D0 GEANT Simulation of the Total Apparatus Response. D0 Note 3191, 1997.
- 53. CERN: GEANT - Detector Description and Simulation Tool. 1993.
- 54. Choi, S. et al.: ATHENA Root Tuple Maker.
http://www-d0.fnal.gov/~suyong/d0_private/athenaweb/athena.htm.
- 55. Bassler, U. et al.: Technical Description of the T42 Algorithm for the Calorimeter Noise Suppression. D0 Note 4146, 2003.
- 56. Stone, A.: Bad Runs.
<http://www-clued0.fnal.gov/~alstone/D0Work/Athena/badruns/badruns.html>.
- 57. Verzocchi, M.: Inclusive Single EM Triggers for W/Z Analyses.
<http://www-d0.fnal.gov/Run2Physics/wz/d0private/triggers/EMtriggers.html>.

58. Jain, S.: Scale and Over-smearing for MC Electron. D0 Note 4402, 2004.
59. Top Physics Working Group: D0 Top Analyses and Data Sample for the Winter Conferences 2004. D0 Note 4419, 2004.
60. Chapin, D. et al.: Measurement of the $Z \rightarrow e^+e^-$ and $W \rightarrow e^\pm\nu$ Production Cross Sections with $|\eta| < 1.05$. 2005.
http://www-d0.fnal.gov/~gardnerj/wzcross_v3.2.pdf.
61. Private Communication with Paul Telford (ptelford@fnal.gov).
62. CDF Collaboration: First Measurement of Inclusive W and Z Cross Sections from Run II of the Tevatron Collider. *Phys. Rev. Lett.*, 94:091803, 2005.
<http://www-cdf.fnal.gov/physics/preprints/index.html>.
63. Heinmiller, J.: Jet Reconstruction Efficiency.
<http://dzero.phy.uic.edu/james/higgs/index.html>.
64. Chakravarti et al.: Handbook of Methods of Applied Statistics, Volume I. John Wiley & Sons, 1967.
65. Private Communication with Mathieu Agelou (agelou@fnal.gov).
66. L2 Trigger Group: L2 Web Page. 2004.
<http://www.pa.msu.edu/hep/d0/l2/>.
67. UIC L2 Trigger Group: L2 Alpha Board Information. 2003.
http://www-d0online.fnal.gov/www/groups/trigger/l2/online/uic_alpha/.
68. Adams, M. et al.: Level-2 Calorimeter Preprocessor Technical Design Report. D0 Note 3651, 1999.
69. Edmunds, D. et al.: Technical Design Report for the L2 Global Processor. D0 Note 3402, 1998.
70. Linnemann, J.: The Standard L2 Crate. 1999.
http://www.pa.msu.edu/hep/d0/ftp/l2/overview/l2_standard_crate.pdf.
71. VITA: VME64 Extensions for Physics and other Application. 1997.
<http://galileo.phys.virginia.edu/~rjh2j/l2beta/vme/vita23d13a.pdf>.

72. Baden, D. et al.: D0 Level 2 Magic Bus. 2004.
http://galileo.phys.virginia.edu/~rjh2j/l2beta/beta_docs/d0_magicbus.pdf.
73. Hirosky, R.: The L2 Beta Project.
<http://galileo.phys.virginia.edu/~rjh2j/l2beta/home.html>.
74. University of Maryland D0 Level 2 Group: A Home page for the MagicBus Transceiver card.
<http://www-d0online.fnal.gov/www/groups/trigger/l2/cards/MBT/index.html>.
75. Linnemann, J.: FIC Card - Fiber Input Converter.
<http://www.pa.msu.edu/hep/d0/l2/fic.htm>.
76. Miller, S. et al.: Level 2 Processor Board Technical Reference Manual. 1998.
http://galileo.phys.virginia.edu/~rjh2j/l2beta/alpha_docs/alphaboard_technical.pdf.
77. DEC: Digital Semiconducor AlphaPC 164 Motherboard. 1997.
http://www-d0online.fnal.gov/www/groups/trigger/l2/online/uic_alpha/l2alpha/.
78. DEC: Digital Semiconducor 21164 Alpha Microprocessor Hardware Reference Manual. 1997.
http://www-d0online.fnal.gov/www/groups/trigger/l2/online/uic_alpha/l2alpha/.
79. Compaq: Alpha Architecture Handbook. 1998.
http://www-d0online.fnal.gov/www/groups/trigger/l2/online/uic_alpha/l2alpha/.
80. DEC: Digital Semiconducor 21172 Core Logic Chipset Technical Reference Manual. 1996.
http://www-d0online.fnal.gov/www/groups/trigger/l2/online/uic_alpha/l2alpha/.
81. Tundra: Universe II User Manual. 1998.
http://www-d0online.fnal.gov/www/groups/trigger/l2/online/uic_alpha/l2alpha/.

VITA

Marc Buehler was born in Rheinfelden, Germany on March 2, 1970. He grew up in Rheinfelden where he attended public school. In 1992 he earned a B.S. in Astronomy from the University of Basel, Switzerland. In 1997 he received a M.S. in Physics from the University of Heidelberg, Germany. He was accepted into the graduate physics program at the University of Illinois at Chicago, USA in 1997. Under the direction of Dr. Nikos Varelas, he received the degree of Doctor of Philosophy in Physics in 2005.